



The Use of Laser-Induced Fluorescence to Characterize Discharge Cathode Erosion in a 30 cm Ring-Cusp Ion Thruster

George J. Williams, Jr.
Ohio Aerospace Institute, Brook Park, Ohio

The NASA STI Program Office . . . in Profile

Since its founding, NASA has been dedicated to the advancement of aeronautics and space science. The NASA Scientific and Technical Information (STI) Program Office plays a key part in helping NASA maintain this important role.

The NASA STI Program Office is operated by Langley Research Center, the Lead Center for NASA's scientific and technical information. The NASA STI Program Office provides access to the NASA STI Database, the largest collection of aeronautical and space science STI in the world. The Program Office is also NASA's institutional mechanism for disseminating the results of its research and development activities. These results are published by NASA in the NASA STI Report Series, which includes the following report types:

- **TECHNICAL PUBLICATION.** Reports of completed research or a major significant phase of research that present the results of NASA programs and include extensive data or theoretical analysis. Includes compilations of significant scientific and technical data and information deemed to be of continuing reference value. NASA's counterpart of peer-reviewed formal professional papers but has less stringent limitations on manuscript length and extent of graphic presentations.
- **TECHNICAL MEMORANDUM.** Scientific and technical findings that are preliminary or of specialized interest, e.g., quick release reports, working papers, and bibliographies that contain minimal annotation. Does not contain extensive analysis.
- **CONTRACTOR REPORT.** Scientific and technical findings by NASA-sponsored contractors and grantees.

- **CONFERENCE PUBLICATION.** Collected papers from scientific and technical conferences, symposia, seminars, or other meetings sponsored or cosponsored by NASA.
- **SPECIAL PUBLICATION.** Scientific, technical, or historical information from NASA programs, projects, and missions, often concerned with subjects having substantial public interest.
- **TECHNICAL TRANSLATION.** English-language translations of foreign scientific and technical material pertinent to NASA's mission.

Specialized services that complement the STI Program Office's diverse offerings include creating custom thesauri, building customized data bases, organizing and publishing research results . . . even providing videos.

For more information about the NASA STI Program Office, see the following:

- Access the NASA STI Program Home Page at <http://www.sti.nasa.gov>
- E-mail your question via the Internet to help@sti.nasa.gov
- Fax your question to the NASA Access Help Desk at 301-621-0134
- Telephone the NASA Access Help Desk at 301-621-0390
- Write to:
NASA Access Help Desk
NASA Center for Aerospace Information
7121 Standard Drive
Hanover, MD 21076



The Use of Laser-Induced Fluorescence to Characterize Discharge Cathode Erosion in a 30 cm Ring-Cusp Ion Thruster

George J. Williams, Jr.
Ohio Aerospace Institute, Brook Park, Ohio

Prepared under Grants NAG3-1572 and NAG3-2216

National Aeronautics and
Space Administration

Glenn Research Center

Acknowledgments

The research presented in this dissertation was supported by NASA Glenn Research Center at Lewis Field (NASA GRC) through grants NAG3-1572 and NAG3-2216. These grants were monitored by James Sovey. In addition, Michael Patterson and Luis Pinero at NASA GRC have been of special assistance. Significant amounts of equipment including an ion thruster, a thruster control system, and a soft-wall clean room were loaned to the University of Michigan by NASA GRC to enable this investigation. The lasers used in this investigation were purchased using funds received through the Defense University Research Initiative Program (DURIP). The author expresses particular gratitude to his advisor, Alec Gallimore, to the departmental technicians, and to his fellow graduate students, especially Tim Smith, Matt Domonkos, and James Haas. The involvement of several undergraduate students (including Karyl Shand, Kathryn Glick, and Yoshi Hikada) was also greatly appreciated.

Available from

NASA Center for Aerospace Information
7121 Standard Drive
Hanover, MD 21076

National Technical Information Service
5285 Port Royal Road
Springfield, VA 22100

Available electronically at <http://gltrs.grc.nasa.gov/GLTRS>

TABLE OF CONTENTS

LIST OF FIGURES	vii
LIST OF TABLES	xi
NOMENCLATURE.....	xii
LIST OF ACRONYMS	xv
CHAPTER	
1. INTRODUCTION.....	1
Ion Thrusters.....	3
Discharge Cathode Erosion.....	7
Laser-Induced Fluorescence	10
Research Objectives.....	11
Notes to Chapter 1	13
2. ASSEMBLY AND OPERATION OF A 30 CM NSTAR-TYPE ION THRUSTER.....	17
NSTAR Ion Thruster Development	17
Characteristics of the New FMT	19
<u>Windows</u>	19
<u>Discharge Cathode Assembly</u>	20

<u>Discharge Chamber</u>	22
<u>Thruster Performance</u>	27
Integration of the FMT at PEPL	29
Notes to Chapter 2	32
3. EXPERIMENTAL APPARATUS AND THEORY	33
Apparatus for Propulsion System Operation	34
<u>The Cathode Test Facility</u>	34
<u>The Large Vacuum Test Facility</u>	35
The Hollow Cathode Assembly	36
Laser-Induced Fluorescence	38
<u>Laser Selection</u>	39
<u>Multiplex LIF Technique</u>	42
<u>Calculation of Velocity and Energy Distributions</u>	49
<u>Density Measurements</u>	50
<u>Uncertainty in LIF Measurements</u>	52
Electrostatic Probe Theory	54
Notes to Chapter 3	57
 4. LASER-INDUCED FLUORESCENCE CHARACTERIZATION OF THE PLUME OF A HOLLOW CATHODE ASSEMBLY	59
Phenomenological HCA Plume Characteristics	60
Xe II Laser-Induced Fluorescence	61
<u>Velocity Measurements</u>	61

<u>Temperature Measurements</u>	65
Xe I Laser-Induced Fluorescence	66
Theories of High-Energy Ion Production	67
Probe Results	71
<u>HCA operation without the anode</u>	72
<u>HCA operation with the anode</u>	73
Implications of the Preliminary Data	75
Notes to Chapter 4	77
 5. DISCHARGE CATHODE EROSION MEASUREMENTS	79
Sputtering Theory	80
Laser-Induced Fluorescence	84
<u>Un-keepered Data</u>	86
<u>Keepered Data</u>	90
Summary	93
Notes to Chapter 5	96
 6. XENON II VELOCIMETRY DOWNSTREAM OF THE DISCHARGE CATHODE IN THE ION THRUSTER	97
Laser-Induced Fluorescence	97
Un-keepered Operation	99
Keepered Operation	107
Comparison of Velocity Profiles	112

Xe II Temperature Measurements	115
Summary.....	117
Notes to Chapter 6	119
7. CORRELATION OF ION VELOCITIES TO DISCHARGE CATHODE EROSION.....	121
Relating Xenon II Energy Measurements to Erosion.....	121
<u>Un-keepered Operation</u>	125
<u>Keepered Operation</u>	128
The Role of Xe III	130
Summary.....	133
Notes to Chapter 7	134
8. CONCLUSIONS AND FUTURE WORK.....	135
Discharge Cathode Erosion Processes	136
Predictions of DCA Erosion.....	137
Demonstration of Laser-Induced Fluorescence	138
Suggested Future Work.....	139
Notes to Chapter 8	142
BIBLIOGRAPHY	143

LIST OF FIGURES

Figure

1.1	A schematic diagram of three ion thrusters on the CNSR spacecraft.....	4
1.2	A schematic of a 30 cm ion thruster	5
1.3	A schematic of a discharge cathode assembly	6
1.4	DCA erosion patterns.....	8
1.5	Erosion rates measured in the 2000, 1000, and 8200 hr wear tests	9
2.1	Photograph and schematic of the FMT 30 cm ion thruster.....	19
2.2	A photograph of the DCA keeper assembly	22
2.3	Characteristic dimensions of the FMT discharge chamber.....	23
2.4	A comparison of the magnetic fields in the FMT-2 and EMT-1 ion thrusters.....	24
2.5	A comparison of the centerline magnetic fields near the exit of the DC.....	25
2.6	A comparison of the discharge chamber efficiencies of the FMT and other ion thrusters.....	25
2.7	A comparison of the FMT's overall thruster performance to that of other ion engines	29
2.8	A photograph of the SKIT-Pac used to operate the ion thruster.....	30
2.9	A schematic diagram of the ion thruster telemetry	31
3.1	A schematic of the HCA in the CTF.....	35
3.2	A schematic of the LVTF at PEPL	36

3.3	A photograph of the hollow cathode assembly	37
3.4	A photograph of the HCA anode	37
3.5	Energy levels and hyperfine structure for the 605—525 nm Xe II transition	38
3.6	A schematic of the laser and beam conditioning optics at PEPL	40
3.7	Beam delivery to the CTF.....	44
3.8	A schematic of multiple beam interrogation.....	45
4.1	Typical Xe II LIF scan data of the 1.4” HCA.....	62
4.2	Typical Xe II axial ion velocity distribution.....	63
4.3	Typical Xe II axial ion energy distribution.....	64
4.4	Centerline Xe II axial velocities for the HCA over various operating conditions	64
4.5	Xe II temperatures measured at different axial positions over various operating conditions of the HCA	66
4.6	Typical Xe I LIF scan data of the HCA	68
4.7	A schematic representation of the effects of a potential hill.....	69
4.8	Langmuir probe data for the HCA operating without an anode	72
4.9	Langmuir probe data for the HCA operating with an anode	74
4.10	A comparison of predicted and measured electron temperatures as a function of discharge voltage.....	75
5.1	Sputter thresholds as a function of angle of incidence	82
5.2	Sputter yields as a function of ion energy and angle of incidence.....	83
5.3	Xe II densities required to produce the erosion observed in the 2000 hr wear test	84
5.4	Typical W LIF data.....	85
5.5	Typical Mo LIF data	85

5.6	Radial distribution of Mo and W LIF signals across the cathode exit plane which have been self-normalized.....	86
5.7	LIF signal strength as a function of discharge current for 25, 27 and 32 V operation.....	88
5.8	Typical Xe I LIF data.....	89
5.9	W LIF signal as a function of discharge current for $V_d = 25$ and 27 V	89
5.10	Erosion-rates predicted for un-keepered operation.....	90
5.11	Mo LIF across the face of the keeper electrode for 13 A, 25 V	91
5.12	Mo LIF signal strength as a function of discharge current for $V_d = 25$ V and 27 V.	92
5.13	DCA keeper erosion rate estimates as a function of discharge current	93
5.14	A comparison of un-keepered and keepered erosion rates	94
6.1	Schematic of laser beam delivery	98
6.2	Typical Xe II LIF data	99
6.3	Centerline axial Xe II velocities downstream of the un-keepered DCA	100
6.4	Axial velocities off-centerline for the 12 A, 27 V condition	101
6.5	A comparison of radial velocities along the centerline for the 12 A, 27 V and 13 A, 25 V un-keepered operating conditions.....	101
6.6	Xe II velocity map for 12 A, 27 V un-keepered operation	103
6.7	Xe II velocity map for 13 A, 25 V un-keepered operation	103
6.8	Normalized axial Xe II energy distributions as a function of radial distribution along the face of the un-keepered DCA for 12 A, 27 V operation.....	105
6.9	Centerline axial Xe II velocities downstream of the keepered DCA.....	107
6.10	Axial velocities off-centerline for the 13 A, 25 V keepered operating condition	108
6.11	A comparison of radial velocities along the centerline for the 12 A, 27 V and 13 A, 25 V keepered operating conditions.....	109

6.12	Xe II velocity map for 13 A, 25 V keepered operation	111
6.13	Xe II velocity map for 12 A, 27 V keepered operation	111
6.14	Energy distributions across the keeper face.....	113
6.15	A direct comparison of the centerline axial ion velocities for the 2000 hr wear test (un-keepered, 12 A, 27 V) and the 8200 hr wear test (keepered, 13 A, 25 V)	114
6.16	Axial temperatures along the centerline of the un-keepered DCA for various operating conditions	116
6.17	Axial temperatures along the centerline of the keepered DCA for various operating conditions	117
7.1	Schematic of the proposed Xe II acceleration mechanisms for un-keepered operation.....	123
7.2	Schematic of the proposed Xe II acceleration mechanisms for keepered operation	124
7.3	Impinging ion energy for un-keepered operation	126
7.4	Required Xe II number densities to produce the W erosion in the 2000 hr wear test illustrating the impact of the fall across the plasma sheath	128
7.5	Xe II number densities required for the observed keeper erosion	129
7.6	Impinging ion energy for keepered operation.....	129
7.7	Xe III number densities required to produce the observed erosion	130

LIST OF TABLES

Table

2.1	DCA/FMT operating conditions	27
2.2	Comparison of discharge voltages with and without beam extraction	28
3.1	LIF Transitions.....	45
3.2	Parameters for Gaussian fitting of the LIF data.....	48
4.1	HCA operating conditions	62
4.2	A comparison of Xe I and Xe II temperatures 0.05 cm downstream of the HCA.....	68
5.1	A comparison of the temperatures of various species as a function of operating condition taken 0.3 cm off centerline, 0.05 cm downstream.....	92
6.1	LIF interrogation angles.....	98
7.1	A comparison of ion energies before and after passing through the sheath.....	127
7.2	Explanations for observed DCA erosion	131
7.3	Calculated Xe III to Xe II current fractions for the NSTAR throttling points.....	132

NOMENCLATURE

A_{ij}	Einstein A coefficient (s^{-1})
b	Impact parameter
c	Speed of light ($2.998 \bullet 10^8$ m/s)
E	Energy (eV)
E_{ij}	Transition energy (eV)
E_s	Sublimation energy (eV)
E_{TH}	Sputter threshold energy (eV)
e	Electron charge ($1.602 \bullet 10^{-19}$ C)
h	Plank's Constant ($6.626 \bullet 10^{-34}$ Js)
F	Force (N)
f	Oscillator strength
g_i	Degeneracy of state i
$g(v)$	Gaussian line shape (s)
G	Gaunt factor
I	Intensity (W/m^2)
I_{SAT}	Saturation Intensity (W/m^2)
i_s	Ions saturation current (A)
J	Current (A)
j	Current density (A/m^2)
K	Empirical constant (atoms/ion/eV ²)
k	Boltzmann constant ($1.381 \bullet 10^{-23}$ J/K)

k_i	Constants for cross section fitting (cm)
$l(v)$	Power broadened line shape (s)
m	Mass (kg)
\dot{m}	Mass flow rate (sccm)
n	Number density (cm^{-3})
P	Probability
R_{cd}	Collisional depopulation rate ($\text{m}^3 \text{s}^{-1}$)
r	Radius (m)
S_n	Energy conversion factor (eV)
T	Temperature (K)
T_e	Electron temperature (eV)
u_B	Bohm velocity (m/s)
V	Voltage (V)
v	Velocity (m/s)
y	Sputter yield (atoms/ion)
z	atomic number
α	Axial angle of interrogation (rad)
β	Lateral angle of interrogation (rad)
γ	Homogeneous relaxation rate (Hz)
λ	Wavelength (m)
λ_D	Debye length (cm)
λ_m	Mean free path (cm)
Ω	Parametric constant

μ	Permeability of free space ($12.52 \cdot 10^{-7}$ H/m)
ν	Frequency (Hz)
σ	Cross-section (cm^2)
θ	Angle of incidence (rad)

Subscripts

a	Ambient
B	Beam
D	Discharge
e	Electron
G	Ground
i	Ion or lower state
j	Upper state
NK	Neutralizer keeper
P	Plasma
Pr	Probe
S	Screen grid

LIST OF ACRONYMS

AIAA	American Institute of Aeronautics and Astronautics
CNSR	Comet Nucleus Sample and Return (Mission)
CTF	Cathode Test Facility
DCA	Discharge Cathode Assembly
DCKA	Keeped Discharge Cathode Assembly
EMT	Engineering Model Thruster
FMT	Functional Model Thruster
FT	Flight Thruster
GRC	NASA Glenn Research Center at Lewis Field
HCA	Hollow Cathode Assembly
HVPI	High-Voltage Propellant Isolator
IEPC	International Electric Propulsion Conference
LIF	Laser-Induced Fluorescence
LVTF	Large Vacuum Test Facility
NASA	National Aeronautics and Space Administration
NSTAR	NASA Solar Electric Propulsion Technologies Application Readiness
PEPL	Plasmadynamics and Electric Propulsion Laboratory

CHAPTER 1

INTRODUCTION

Recent progress in technologies such as solid state physics and wireless communications has led to an exponential growth in the commercial utilization of space and in remote (i.e. robotic) exploration of the solar system. Spacecraft propulsion systems which provide high propellant exit velocities imply great mass savings in terms of either payloads delivered to a given destinations or in propellant needed to achieve given missions. Both savings could significantly lower the cost of deploying a given spacecraft and/or significantly enhance the lifetime or capabilities of that spacecraft.¹

Every spacecraft maneuver has a characteristic velocity, Δv , associated with it which is proportional to the velocity of the propellant exiting the thruster, u_e , and to the natural log of the ratio of spacecraft mass before and after the maneuver. Clearly, to maximize the cost effectiveness and/or the amount of useful equipment delivered for a given mission (i.e. the ratio of final mass to initial mass of the spacecraft), u_e should be as large as possible. Ideally, propulsion systems used for orbit changing and station keeping missions would have u_e between 10,000 and 25,000 m/s.² Requirements for interplanetary missions are even greater, *e.g.*, 50,000 m/s for a mission to Mars.² High-performance chemical rockets are limited to u_e 's on the order of 5000 m/s by the energy available in chemical combustion.³ Chemical propulsion systems typically used for satellite maneuvering and station keeping use less energetic, more storable, propellants

and have u_e 's on the order of 3000 m/s.⁴ One method of meeting the high u_e requirements for both station keeping and interplanetary missions is electric propulsion.

Electric propulsion is the acceleration of gases for propulsion by electrical heating and/or by electric and magnetic body forces.⁵ Typically, devices for electric propulsion fall into one of three categories: electrothermal propulsion which electrically heats the propellant and then expands it thermodynamically through a nozzle to convert its thermal energy into a jet of directed kinetic energy, electrostatic propulsion which ionizes and then accelerates the propellant through an electric field, and electromagnetic propulsion which ionizes and then accelerates a propellant via interactions of external and internal magnetic fields with electric currents driven through the stream.⁵ Electrothermal devices such as arcjets provide maneuvering and control rockets on spacecraft with the principal advantage of more efficiently using propellants and propellant feed systems designed for chemical rockets. Electrostatic thrusters such as ion engines and Hall thrusters have the potential to achieve very high exit velocities but at the expense of low thrust.⁵ Electromagnetic thrusters such as magnetoplasmadynamic (MPD) engines have the potential to provide both high exit velocities and relatively high thrust. However, these are the least developed of the three types of electric propulsion.⁵

Since a large u_e typically implies a large, massive power source carried on board the spacecraft and/or a relatively low thrust in some cases, there are typically tradeoffs between high u_e and the fraction of the final mass which is dedicated to the power supply and/or the time required to perform the maneuver. These tradeoffs have been the object of extensive study and regimes of optimal u_e have been identified.^{2,6}

As early as 1906, Robert Goddard expressed many of the concepts of electric propulsion.^{5,7} However, due to the lack of practical, lightweight electrical power sources

for space applications, the first feasibility studies were not undertaken until the late 1940's and early 1950's.⁸ During the 1960's, many types of electric propulsion devices were developed and significant attention was paid to performance testing and mission analysis. The first successful test of an electric thruster, an electrostatic ion thruster, occurred on July 20, 1964, the Space Electric Rocket Test I (SERT I). Today, over 140 spacecraft employ electric propulsion systems (almost exclusively electrothermal and electrostatic systems) primarily for station keeping and attitude control.¹⁴

Ion Thrusters

Ion thrusters are high-efficiency, high specific impulse propulsion systems used for station keeping, orbit transfer, and planetary missions⁹. Ion thrusters are capable of producing exhaust velocities above 30,000 m/s and electrical efficiencies above 60 percent. These attributes can significantly decrease the propellant mass fraction and, for many planetary missions, substantially decrease the trip time.¹⁰ As a result of the NASA Solar Electric Propulsion Technology Application Readiness (NSTAR) program, a xenon ion propulsion system was demonstrated as primary propulsion on Deep Space 1, the first of the New Millennium missions.¹¹ Ion propulsion is considered the enabling technology for the Comet Nucleus Sample and Return (CNSR) mission slated for 2003.¹² and a number of Discovery mission proposals for small body rendezvous, Mercury orbiter, and Jupiter polar orbiter missions. Ion propulsion is now considered a critical technology for proposed missions in the 2005-2010 time frame such as Europa Lander, Neptune Orbiter, Saturn Ring Explorer, and Venus Sample Return.¹³ In addition, insertion into geosynchronous orbit (GEO) from a geo-transfer orbit (GTO) has been demonstrated by a Hughes 25 cm ion thruster, and several satellites currently use ion propulsion to maintain

geo-synchronous orbit.¹⁴ Figure 1.1 shows a schematic of three 30 cm ion thrusters on the CNSR spacecraft.

Figure 1.2 gives a schematic of an ion thruster. Neutral Xe is fed into the thruster to maintain a pressure on the order of 10^{-4} Torr. Roughly 10 percent of the gas in the discharge chamber is ionized by the electrons from the discharge cathode.³ Magnetic fields created by three rings of magnets confine the primary electrons and minimize the loss of ions to the anode. After colliding with the neutral gas, the electrons become thermalized and are then collected by the anode. The ions migrate to the inner ion optic

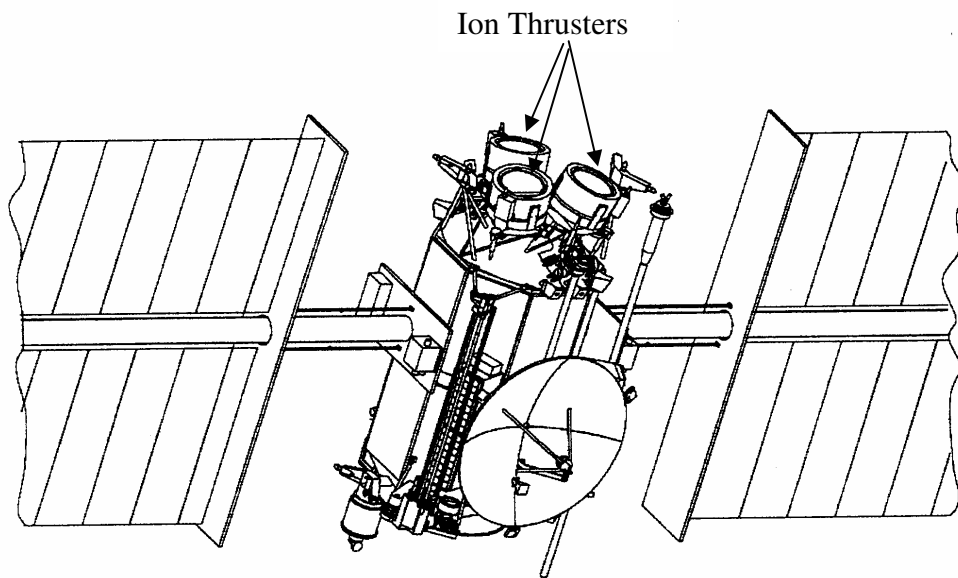


Figure 1.1 A schematic diagram of three ion thrusters on the CNSR spacecraft.¹²

grid, the screen grid, which is maintained at cathode potential. Once the ions reach the screen grid, they are accelerated between the screen and accelerator grids and leave the thruster at high velocities. The ion extraction rate is limited by space-charge considerations, the open area of the screen grid, and the uniformity of the discharge plasma density over the screen grid surface.³ Occasionally, sputtered grid material or dust from the testing facility results in a short between the grids. The material is cleared by the resulting spark. The thruster power processing system resets the high voltage and discharge currents after the initial spark to limit the high-voltage, high-current to a few milliseconds. The entire process is referred to as a recycle. To prevent thrust charge build up and to neutralize the beam space charge, a neutralizer (a hollow cathode assembly (HCA) mounted on the side of the thruster) is used to inject excess electrons into the beam.

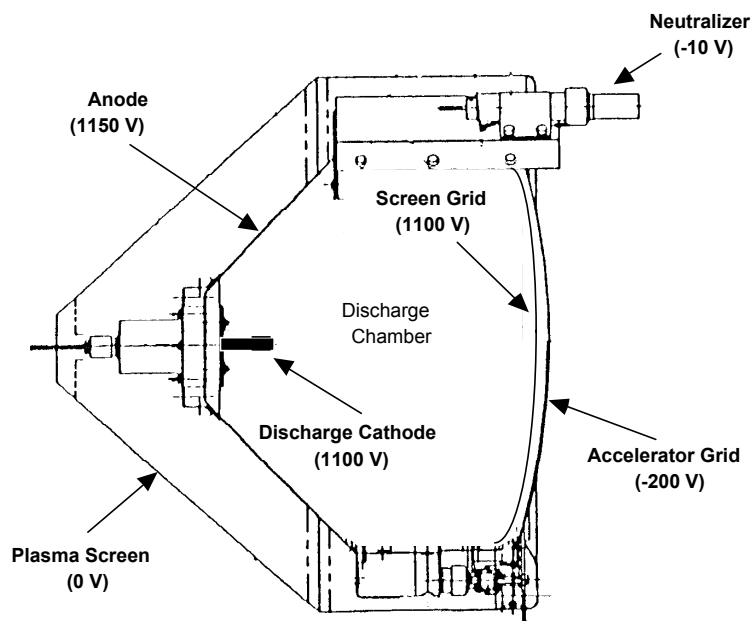


Figure 1.2 A schematic of a 30 cm ion thruster.⁹

Figure 1.3 gives a schematic of the discharge hollow cathode assembly (DCA) which injects electrons into the discharge chamber and ionizes the propellant. Inside the hollow cathode, electrons are thermionically emitted from a low work function material. Some electrons are also generated by field effect emission. Application of a voltage to an electrode immediately downstream of the cathode orifice initiates a discharge in the cathode tube. Typically this electrode continues to draw current under steady state operation to ensure that the discharge and cathode emission processes will continue even if the main current to the anode or to the ion beam is interrupted, hence it is given the name “keeper” electrode.¹⁵ The enclosed keeper geometry improves discharge stability and reduces the amplitude of electrical noise. The plasma created in the cathode tube heats the cathode insert thus sustaining electron emission and facilitating release of high-energy electrons through the cathode orifice.

Ion thrusters are being scaled to different powers and operating conditions to meet the requirements of the flight applications including those mentioned earlier. A baseline for this scaling is the NASA 30 cm ion thruster. Several wear-tests have been

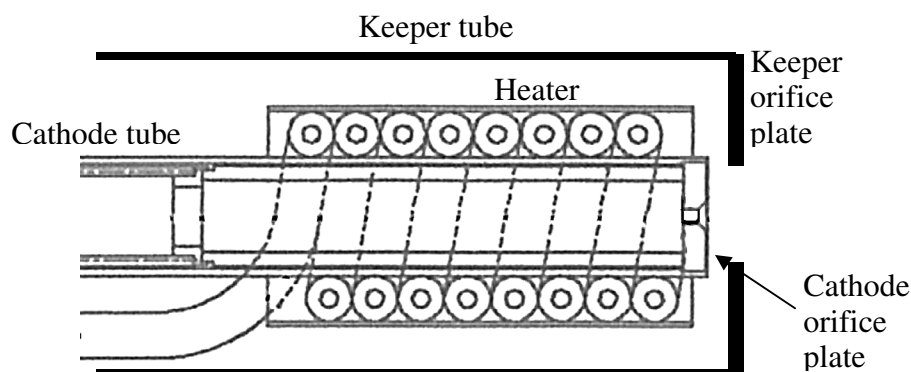
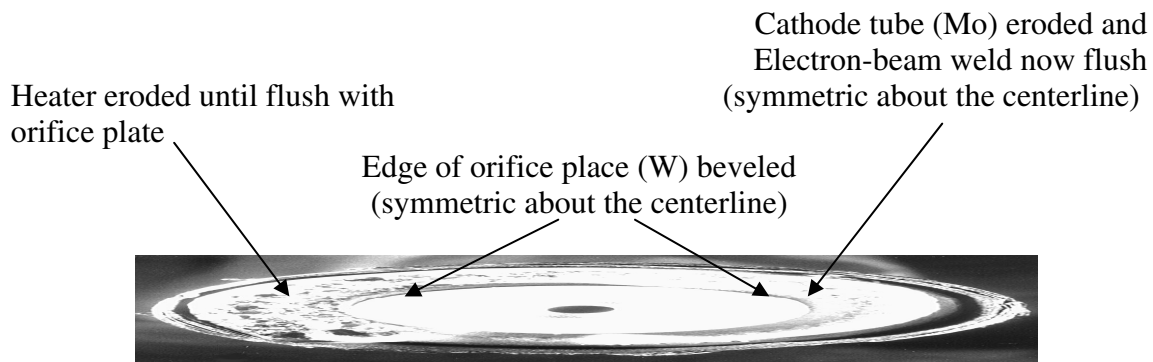


Figure 1.3 A schematic of a discharge cathode assembly.

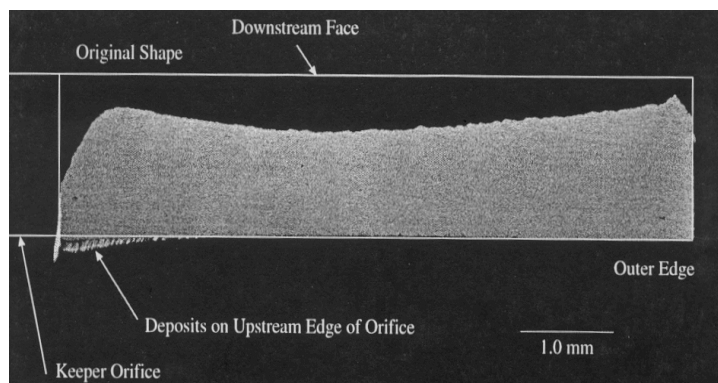
conducted to demonstrate long duration operation and to identify life-limiting phenomena. One of the potential failure mechanisms identified during these tests which could preclude the more demanding missions mentioned above was erosion of the DCA's downstream surfaces. Other potential failure mechanisms included accelerator grid erosion, screen grid erosion, and flaking of Mo deposited on the anode surfaces.¹¹

Discharge Cathode Erosion

The DCA in the first NSTAR thruster did not employ a keeper electrode. Severe erosion of the outer edge of the thoriated-tungsten orifice plate, the tip of the Mo-Re cathode tube, and the Ta heater coil outer sheath were observed in a 2000 hr development wear-test.¹⁶ The alloying of Mo and Re and the Th impregnation of the W prevent recrystallization of the Mo and W following high-temperature operation. Because measurements were performed on the Mo and W components of these materials, the components are referred to below without reference to the alloying metals. The orifice plate eroded at 145 $\mu\text{m}/\text{hr}$ and the cathode tube at 280 $\mu\text{m}/\text{hr}$.¹⁷ The discharge cathode assembly (DCA) was replaced after 870 hrs because it was believed that the erosion might have been anomalous. However erosion of the second DCA was similar to that of the first. The erosion pattern is highlighted in Fig. 1.4a. A Mo keeper electrode was introduced as an engineering solution, and, after subsequent 1000 hr and 8200 hr wear-tests the cathode orifice plate erosion was reduced to less than 3 $\mu\text{m}/\text{hr}$.^{10,13,17} This rate is significantly below the estimated acceptable threshold of 64 $\mu\text{m}/\text{hr}$.¹⁷ Shown in a photograph in Fig. 1.4b, the keeper orifice plate did erode at a



a. Photograph and sketch indicating un-keepered DCA erosion after 1000 hrs of the 2000 hr wear-test.



3 Photograph of the DCA keeper after the 8200 hr life-test.³

Figure 1.4 DCA erosion patterns.

rate of roughly $60 \mu\text{m}/\text{KHR}$ in the 8200 hr test.¹⁷ The various erosion rates are summarized in Fig. 1.5. Additional modifications to the DCA after the 2000 hr test included moving the electron beam weld from the face of the cathode orifice plate to the side of the cathode tube to further shield it from back-flowing ions and retraction of the heater coil to roughly 0.1 cm upstream of the cathode orifice plate exit plane both to shield it and to facilitate incorporation of the keeper electrode. During the 1000 hr test at the Jet Propulsion Laboratory (JPL) which incorporated these changes, the cathode

flow rate was inadvertently increased above that of the 2000 hr test. This flow rate was maintained in the subsequent 8200 hr life test because it was believed that higher flow rate might have contributed to the reduction in erosion. The discharge current was increased from 12.1 A to 13.1 A to maintain the 1.76 A beam current. The increased flow rate also reduced the discharge voltage from 26.7 V to 25.1 V even with the increased current. The NSTAR flight thruster has incorporated all of these modifications including the higher discharge cathode flow rate. It has been suggested that higher powers and longer periods of operation can be accommodated by thickening

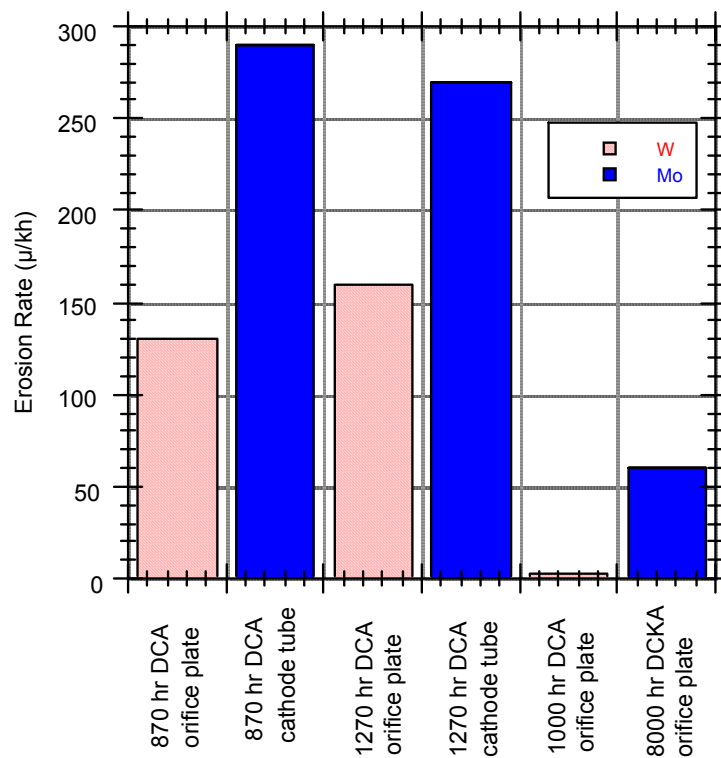


Figure 1.5 Erosion rates measured in the 2000, 1000, and 8200 hr wear tests.¹⁷ Note that the 1000 and 8000 hr tests were conducted with a keeper and that the erosion shown for the 8000 hr case is of the keeper orifice plate.

the orifice plates.¹² However, recent developments in cathode assembly design may not make this a feasible option as the orifice plates may be tapered towards their orifices.^{18,19}

During testing of high-current HCA's independent of ion thruster operation, relatively rapid erosion of an un-chamfered orifice plate occurred.²⁰ The appearance of the keeper after the erosion suggested the sputtering probably occurred from high-energy ions originating close to the cathode orifice. Some ions are focused in such a way that they strike the orifice plate at angles generating a chamfer. If these ions miss the orifice plate, they are thermalized by neutral atoms before reaching the anode.²⁰

The source of the high-energy ions causing the erosion has remained largely unknown. Ray-tracing after the 2000 hr test indicated that the source of the ions was located between 1 and 11 mm downstream of the orifice plate. The potential-hill phenomenon, which has been postulated as the source of high-energy ions eroding downstream cathode-potential surfaces, is the leading explanation.²¹ However, sheath effects and doubly charge xenon ions (Xe III) may account for the erosion pattern and plasma oscillations and charge-exchange collisions might also yield the high-energy ions required for the erosion.

Laser-Induced Fluorescence

Laser-induced fluorescence has been used successfully to interrogate both Xe plasmas and sputter eroded species associated with electric propulsion devices. Several velocimetry investigations of Hall thruster plumes have been conducted.^{22,23,24,25} These investigations have demonstrated LIF techniques and the ability of LIF to provide significant performance characterization of various thrusters. The ion number density in the plume of Hall thrusters (roughly 10^{12} cm^{-3}) is comparable to that in the near-orifice

region of hollow cathodes. Therefore, the techniques demonstrated in the Xe plume of Hall thrusters should be transferable to cathode plume investigations. One potential issue is that the high velocities present in the Hall thruster plumes (on the order of 10,000 m/s) may mask inherent errors which will be more significant at the lower velocities in the cathode plume.

Laser-induced fluorescence has also been used to study surfaces eroded by ion beams and immersed in plasmas.^{26,27,28,29} These techniques have also been applied to the measurement of the density of Mo eroded from the accelerator grid by impinging xenon ions.^{30,31,32} The grid erosion measurements yielded relative Mo LIF signal strengths as a function of operating conditions and/or grid voltages. The measured erosion rates of the grids and of the DCA indicate that the density of Mo near the DCA will be slightly less than that downstream of the grids for keepered operation and un-keepered operation primarily because of the smaller region of erosion on the DCA. However, the intensity of the laser in this investigation is significantly greater than that of the previous investigations implying that the Mo LIF signals should be relatively strong near the DCA.

Research Objectives

Given the previous investigations, there was confidence that laser-induced fluorescence (LIF) employed in this investigation would measure Xe II velocity distributions and Xe I, W and Mo relative concentrations near the exit of the DCA. LIF will permit the correlation of the erosion rates of DCA components with thruster operating conditions and the determination of physical processes that lead to high-energy ion impact on the DCA. Such understanding will facilitate confidence in thruster

operation and life as design modifications and power scaling are incorporated to enable the missions described above. Specifically, the objectives of this investigation are to

- Design, assemble, and operate at the university of Michigan an NSTAR-type ion thruster with internal optical access
- Develop a laser-induced fluorescence diagnostic capability
- Measure Mo and W relative densities near the DCA in kept and un-kept configurations as a function of thruster operating condition
- Measure Xe II velocities near the DCA
- Correlate the measurements of eroded species and ion velocities to identify potential causes of the erosion and what operating conditions will minimize the erosion.

Except for ion thruster assembly and initial testing, which were undertaken at NASA Glenn, the investigation was conducted at the Plasmadynamics and Electric Propulsion Laboratory (PEPL) at the University of Michigan.

Notes to Chapter 1

-
- ¹ Poeschel, R.L., and J.R. Beattie, “Primary Electric Propulsion Technology Study,” NASA CR-159688, 1979.
- ² Deininger, W.D., “Advanced Propulsion System Options for Geostationary Satellites,” AIAA-94-3001, 30th Joint Propulsion Conference (June, 1994).
- ³ Wilbur, P.J., “Ion Propulsion,” Advanced SEI Technologies Conference (September, 1991).
- ⁴ Sutton, G.P., *Rocket Propulsion Elements*, 6th edition, John Wiley and Sons, 1992.
- ⁵ Jahn, R.G., *Physics of Electric Propulsion*, McGraw Hill, 1968, pp 2–20.
- ⁶ Gulczinski, F.S., and R.A. Spores, “Analysis of Hall Effect Thrusters and Ion Engines for Orbit Transfer Missions,” AIAA-96-2973, 32nd Joint Propulsion Conference (July, 1996).
- ⁷ Stuhlinger, E., *Ion Propulsion for Space Flight*, McGraw Hill, 1964, pp 2–15.
- ⁸ Stuhlinger, E., “Possibilities of Electrical Space Ship Propulsion,” *Ber. 5th Intern. Astronaut. Kongr.*, Innsbruck, (August, 1954) 100.
- ⁹ Patterson, M.J., et al, “Performance of the NASA 30 cm Ion Thruster,” IEPC-93-108, 23rd International Electric Propulsion Conference, (September, 1993).
- ¹⁰ Polk, J.E., *et al.*, “A 1000-Hour Wear Test of the NASA NSTAR Ion Thruster,” AIAA-96-2717, 32nd Joint Propulsion Conference (July, 1996).
- ¹¹ Polk, J. *et al.*, “Validation of the NSTAR Ion Propulsion System on the Deep Space One Mission: Overview and Initial Results,” AIAA-99-2274, 35th Joint Propulsion Conference, (July, 1999).
- ¹² Brophy, J.R., *et al.*, “The Ion Propulsion System on NASA’s Space Technology 4/Challengion Comet Rendezvous Mission,” AIAA-99-2856, 35th Joint Propulsion Conference, (July, 1999).
- ¹³ Polk, J.E., “An Overview of the Results from an 8200 Hour Wear Test of the NSTAR Ion Thruster,” AIAA-99-2446, 35th Joint Propulsion Conference (June, 1999).
- ¹⁴ Myers, R., “Overview of Electric Propulsion Activities in Industry,” AIAA-2000-3147, 36th Joint Propulsion Conference, (July, 2000).

-
- ¹⁵ Jack, T.M., *et al.*, “The Effect of the Keeper Electrode on Hollow Cathode Characteristics,” AIAA-2000-3533, 36th Joint Propulsion Conference (July, 2000).
- ¹⁶ Patterson, M.J., *et al.*, “2.3 kW Ion Thruster Wear Test,” AIAA-95-2516, 31st Joint Propulsion Conference (July, 1995).
- ¹⁷ Patterson, M.J., Internal memo, June, 1995.
- ¹⁸ Domonkos, M.T., “Evaluation of Low-Current Orificed Hollow Cathodes,” Ph.D. Thesis, The University of Michigan, October, 1999, pp 153-157.
- ¹⁹ Katz, I., and Patterson, M.J., “Optimizing Plasma Contactors for Electrodynamic Tether Missions,” Presented at Tether Technology Interchange, September 9, 1997, Huntsville, AL.
- ²⁰ Kameyama, I., and P.J. Wilbur, “Characteristics of Ions Emitted from High-Current Hollow Cathodes,” IEPC-93-023, 23rd International Electric Propulsion Conference (August, 1993).
- ²¹ Kameyama, I., and P. J. Wilbur, “Potential-Hill Model of High-Energy Ion Production Near High-Current Hollow Cathodes,” ISTS-98-Aa2-17, 21st International Symposium on Space Technology and Science, (May, 1998).
- ²² Manzella, D. H., “Stationary Plasma Thruster Ion Velocity distribution,” AIAA-94-3141, 30th Joint Propulsion Conference (June, 1994).
- ²³ Cedolin, R. J., *et al.*, “Laser-Induced Fluorescence Diagnostics for Xenon Hall Thrusters,” AIAA-96-2986, 32nd Joint Propulsion Conference, (July, 1996).
- ²⁴ Keefer, D., “Multiplexed LIF and Langmuir Probe Diagnostic Measurements in the TAL D-55 Thruster,” AIAA-99-2425, 35th Joint Propulsion Conference (June, 1999).
- ²⁵ Williams, G. J., *et al.*, “Laser Induced Fluorescence Measurement of the Ion Energy Distribution in the Plume of a Hall Thruster,” AIAA-99-2424, 35th Joint Propulsion Conference, (June, 1999).
- ²⁶ Calaway, W. F., *et al.*, “Laser-Induced Fluorescence as a Tool for the Study of Ion Beam Sputtering,” *Handbook of Ion Beam Processing Technology*, Noyes Publications, park Ridge, NJ, 1989, pp. 112-127.
- ²⁷ Bay, H. L., “Laser-Induced Fluorescence as a technique for Investigations of Sputtering Phenomena,” *Nuclear Instruments and Methods in Physics Research B*, **18**, 1987, 430-445.

-
- ²⁸ Husinsky, W., “The Application of Doppler Shift Laser Fluorescence Spectroscopy for the Detection and Energy and Energy Analysis of Particles Evolving from Surfaces,” *Journal of Vacuum Science and Technology*, **B3** (5) 1985, 1546–1559.
- ²⁹ Gaeta, C.J., *et al.*, “Plasma Erosion Rate Diagnostics Using Laser-Induced Fluorescence,” *Review of Scientific Instruments*, **63** (5) 1992, 3090–3095.
- ³⁰ Gaeta, C.J., *et al.*, “Erosion Rate Diagnostics in Ion Thrusters Using Laser-Induced Fluorescence,” *Journal of Propulsion and Power*, **9** (3) 1993, 369–376.
- ³¹ Crofton, M.W., “Laser Spectroscopic Study of the T5 Ion Thruster,” AIAA–96–5151, 32nd Joint Propulsion Conference (July, 1996).
- ³² Beattie, J.R., and J.N. Matossian, “High-Power Ion Thruster Technology,” NASA Technical Report CR–195477, 1992.

CHAPTER 2

ASSEMBLY AND OPERATION OF A 30 CM NSTAR-TYPE ION THRUSTER

Operation of an ion thruster at PEPL presupposes a thruster suitable for optical diagnostics and evaluation of erosion in NSTAR-like ion thrusters. A discussion of the thruster specifically designed and assembled for operation at PEPL follows a brief history of recent ion thruster development.

NSTAR Ion Thruster Development

Development of a lightweight, 30 cm ion thruster began in 1992 and led to the NSTAR ion thruster program. This first attempt to integrate ten years of technological developments and significant weight reduction beyond a purely laboratory model thruster resulted in a pre-engineering model thruster dubbed the functional model ion thruster (FMT). It had a configuration similar to that which might be used in flight applications and was intended to verify the physical and functional design and the manufacturing processes.¹ Major developments incorporated into the FMT were the use of a conical discharge chamber, the use of non-ferromagnetic material (Al 1100) as the principal structural material, an un-keepered DCA, reverse propellant injection, and a simplified power processing scheme.² Discharge cathode, magnetic field, neutralizer, and ion optics were similar to previous engines. Vibration testing of the FMT indicated

areas for design improvement, but no damage was incurred in these tests.¹ Parts for three FMT's were fabricated, but only one was assembled.

Four engineering model thrusters (EMT's) were developed from the basic design of the FMT.³ EMT-1 through EMT-3 incorporated Al 1600 while EMT-4 used Ti as its primary structural material. EMT-1 was endurance tested at NASA Glenn for 2000 hrs and at JPL for 1000 hrs.^{4,5} EMT-2 was incorporated in a 8200 hr life-test at JPL.⁶ Two flight thrusters (FT's) were fabricated at Hughes Electron Dynamics Division,⁷ and FT-1 was installed on the Deep Space 1 spacecraft.

In order to perform significant internal optical diagnostics such as LIF, optical access via windows in the discharge chamber was required. Modification and assembly of the second FMT, FMT-2, was more expedient and more practical than modification of an assembled EMT or of fabrication and assembly of an additional EMT. In addition to permitting optical access, design modifications insuring identical DCA operation and plasma environment near the DCA to that of both EMT-1 and EMT-2 in their respective wear-tests were incorporated. The principal modifications included

- Incorporation of windows in the discharge chamber
- Incorporation of windows in the plasma screen
- Relocation of gimbal mounting to permit optical diagnostics
- Reconciliation of FMT and EMT discharge cathode mounting
- Simplification of discharge cathode keeper mounting
- Modification of high-voltage propellant isolator (HVPI) design
- Modification of neutralizer mounting
- Reconciliation of mounting EMT ion optics on an FMT frame
- Modification of EMT DCA design

To the extent possible, EMT components were incorporated into the assembly.

Characteristics of the New FMT

The modifications were incorporated into the FMT at NASA Glenn. The modified FMT is shown in Fig. 2.1. Each of the notable characteristics or modifications is discussed in detail below.

Windows

Three 10.2 cm by 3.2 cm by 0.3 cm windows were placed on the discharge chamber as shown in Fig. 2.1, replacing roughly 3.5 percent of the Al anode. The laser beams entered and exited through the top and bottom windows, and the fluorescence was collected through the side window. Quartz and plane glass windows were used. Each window rested in a frame, and small screw clamps created a pressure seal between the windows and the anode.

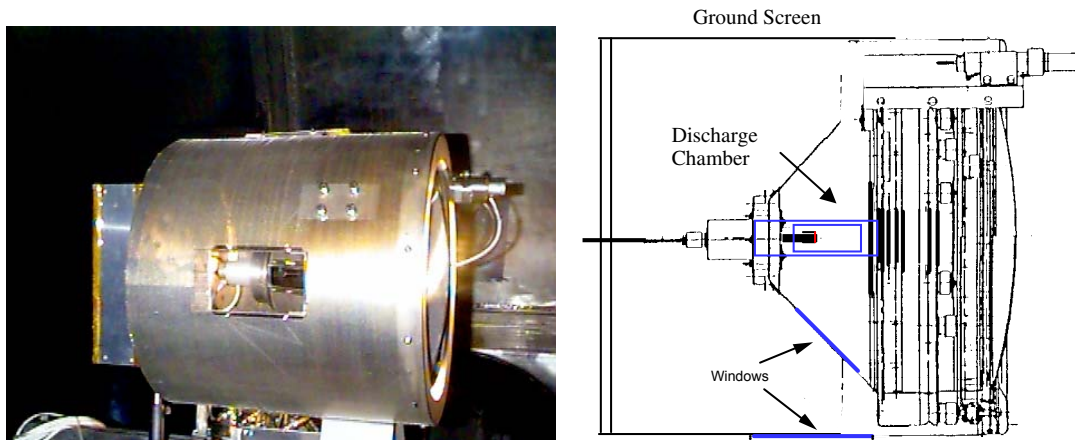


Figure 2.1 Photograph and schematic of the FMT 30 cm ion thruster. Note the location of the windows on the discharge chamber wall and the ground screen.

Three quartz windows were also placed on the ground (plasma) screen. The top and bottom windows were 12.7 cm by 4.5 cm by 0.15 cm which permitted angled laser beams to pass in and out of the thruster. The length of the windows was limited by the structural support ring around the discharge chamber which precluded both optical access to the discharge chamber and blocked beams entering at large downstream angles. A 12.7 cm by 7.6 cm by 0.15 cm window on the side of the plasma screen maximized the fluorescence which could be collected through the smaller window on the anode. The plasma screen was made cylindrical instead of conformal as in the EMT's and FT's in order to accommodate these windows. Small screw clamps held the windows in frames on the plasma screen in a manner analogous to that of the windows on the discharge chamber. All six windows can be removed without additional disassembly of the thruster.

Discharge Cathode Assembly

As noted in Chapter 1, the electron beam weld was moved to the side of the Mo-Re cathode tube following the 2000 hr wear-test. In order to duplicate the erosion in that test, the cathodes used in this investigation were fabricated with the electron beam weld on the downstream face of the W orifice plate. This also permitted interrogation of Mo species since the Mo tube would otherwise have been shielded from erosion by the orifice plate.

The heater coil was located slightly upstream of the cathode exit plane as per the 1000 hr wear-test and all subsequent EMT and FT thrusters but unlike EMT-1 in the 2000 hr test. This permitted incorporation of a keeper electrode without installation of an alternative cathode (which might have complicated comparisons between keepered

and un-keepered results). However, it prohibited accurate reproduction of the Ta erosion observed in the 2000 hr test, but preliminary analysis indicated that Ta LIF would have been prohibitively difficult due to LIF interrogation lines being relatively far in the UV (330 nm).

Two new discharge cathode assemblies were fabricated. One broke upon initial installation and was replaced by the DCA used in the second half of the 2000 hr wear test with a new heater and a new insert. The second new DCA was held in reserve. The DCA was mounted through the rear of the discharge chamber as per the EMT configuration.

Shown in Fig. 2.2, the Mo keeper electrode and its mounting structure were similar to those employed on the EMT's. The principal modification was the addition of a second, upstream flange to the keeper assembly which permits installation and removal of the keeper electrode with only minimal disassembly of the thruster, i.e. removal of only the ion optics instead of removal of the ion optics, plasma screen, and the entire DCA. Initial, un-keepered operation was performed without any keeper mounting components in the thruster as per the 2000 hr wear-test. Un-keepered operation following keepered operation was conducted with the keeper flange at anode potential.



Figure 2.2 A photograph of the DCA keeper assembly.

Discharge Chamber

To insure the reproduction of the plasma conditions which resulted in the DCA erosion, high priority was given to insuring the similarity of the physical dimensions and of the magnetic field in the discharge chamber of the FMT-2 to that of the EMT-1. The characteristic dimensions of the discharge chambers which are illustrated and compared on a schematic diagram in Fig. 2.3. The differences are negligible.

Figure 2.4 compares the magnetic field in the FMT-2 and EMT-1 discharge chambers with the same discharge cathode assembly. Radial and axial magnetic field measurements were taken on each thruster with a Gaussmeter. The spatial resolution was roughly 0.5 cm in the region near the cathode and roughly 1.0 cm in the bulk of the discharge chamber. The measurements were calibrated with Helmholtz coils and showed a very good repeatability. The error was roughly 5 percent. The two fields are nearly identical. Figure 2.5 compares the axial magnetic fields for several thrusters. These data were taken in a similar manner as those presented in Fig. 2.4.

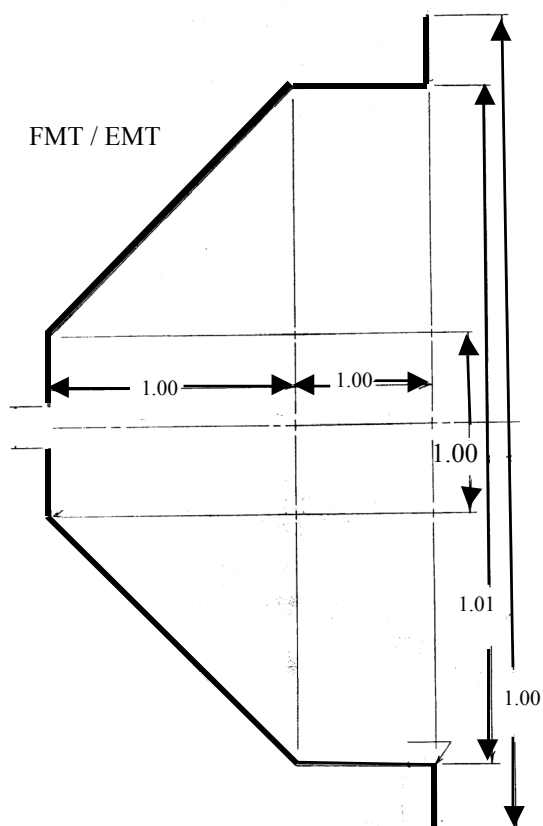


Figure 2.3 Characteristic dimensions of the FMT discharge chamber.
Numbers indicate the ratio of dimensions of the FMT to the EMT-1.

but only axial magnetic field components were measured. Note that the field strength at the exit of the cathode is nearly identical in all cases (~ 107 G). The similarity in the fields and other parameters indicates that the plasma should be similar in these thrusters and that the erosion observed in the FMT should be representative of erosion in other NSTAR-type thrusters.

Figure 2.6 compares the keptered discharge chamber performance of the FMT operated at PEPL with other thrusters taken at NASA Glenn. Note that the addition of windows appeared to have little impact. The agreement of these curves also adds confidence to the representative nature of FMT-2 measurements. The inner surfaces of the windows were found to be coated with sputtered metal after extended operation. The amount of coating was proportional to the number of recycles

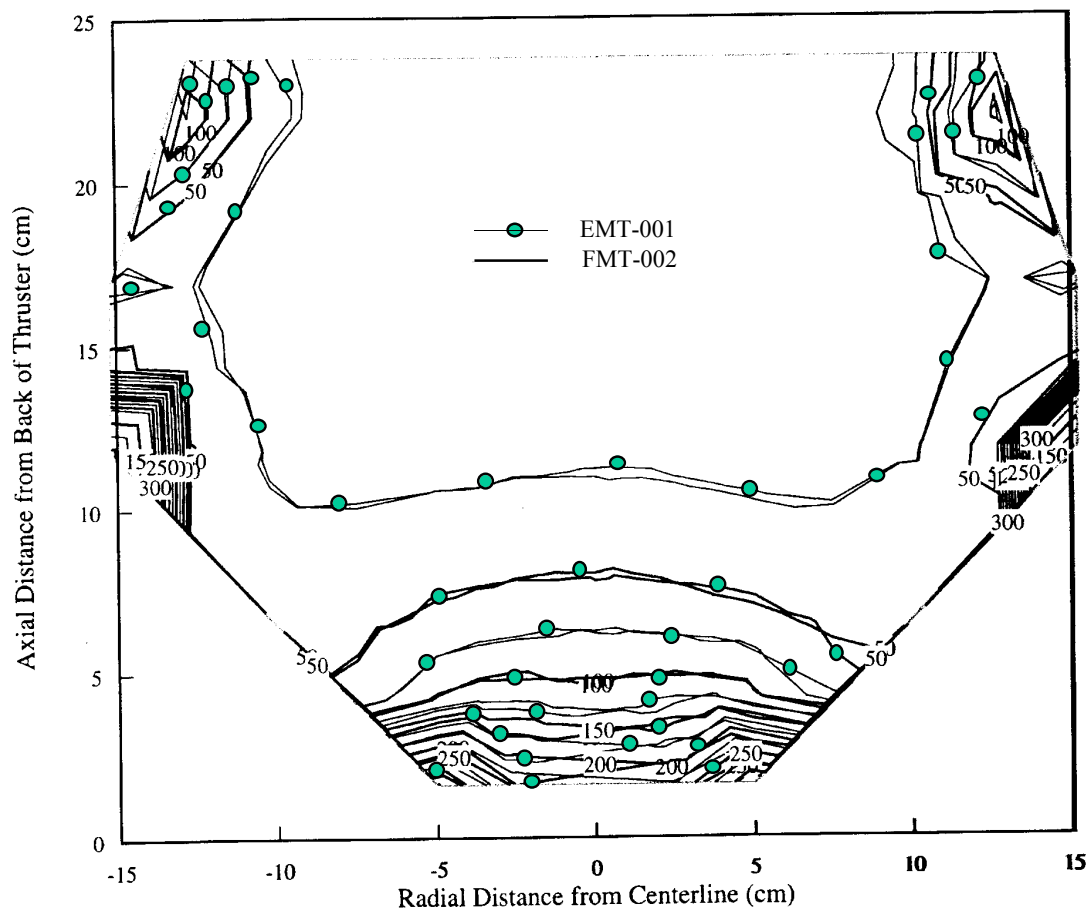


Figure 2.4 A comparison of the magnetic fields in the FMT-2 and EMT-1 ion thrusters. Data are in Gauss. Note that the fields are nearly identical.

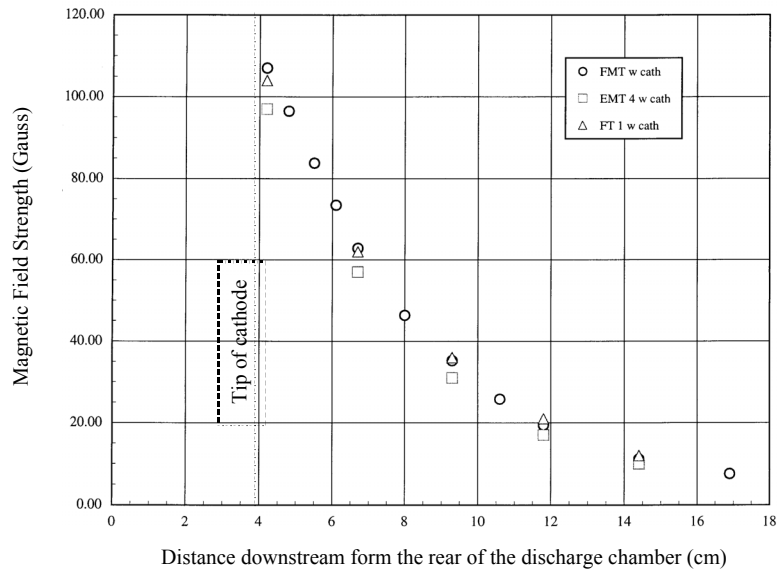


Figure 2.5 A comparison the centerline magnetic fields near the exit of the DCA.

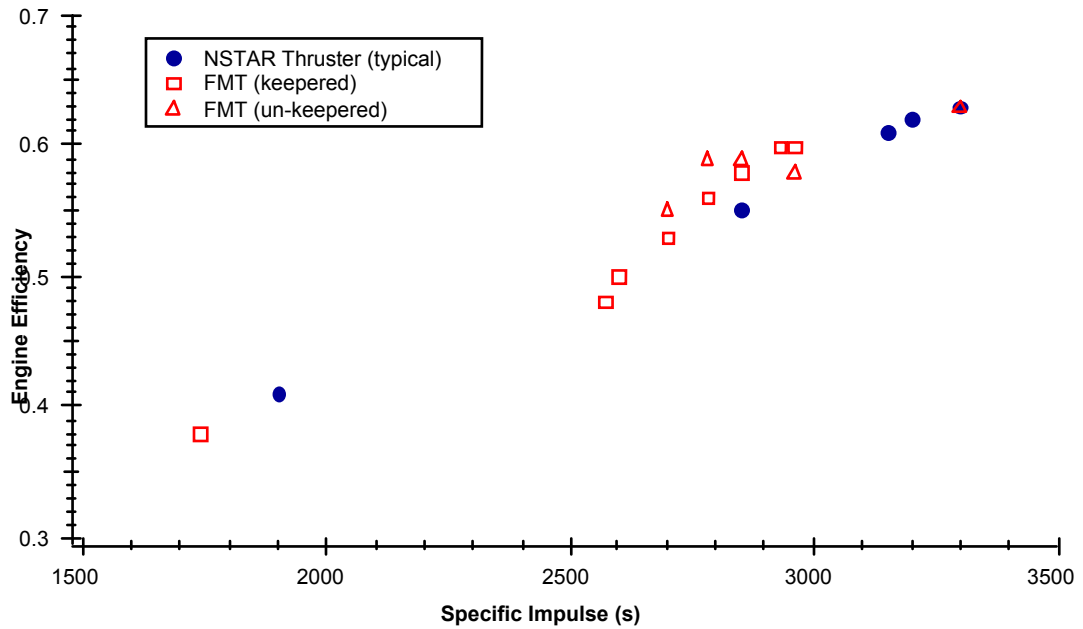


Figure 2.6 A comparison of the discharge chamber efficiencies of the FMT and other ion thrusters.

(grid clearing events) and to the thruster power at which the recycles occurred. Under nominal operating conditions with recycles occurring less than one per hour, the coating was minimal resulting in a 20 percent loss in transparency over tens of hours. The windows did not coat uniformly under these conditions with the downstream ends coating more than the upstream ends. However, during one period of testing when a screen grid to anode thermal short resulted in tens of recycles per hour, the windows were uniformly coated and became nearly opaque. In all cases, the three windows did not appear to coat at different rates, and the coating of glass or quartz windows was indistinguishable. No material analysis was performed on the windows, but the material collected on them is predicted to be Mo from the screen grid. Such analysis is recommended as part of the follow on studies.

Various other design modifications were incorporated. A single gimbal mount was placed at the base of the FMT to facilitate optical access. Addition of a post on the box containing the high-voltage propellant isolators (HVPI's) provided stability. One HVPI consisted of a viton tube on the discharge cathode line as per EMT-1. Five 0.32 cm diameter cryobreaks were used as the other HVPI on the main propellant supply line instead of the 12 used on EMT-1. The reduction in the number of cryobreaks resulted from tests conducted at GRC as part of this investigation. A laboratory model plasma contactor was used as the FMT-2's neutralizer. The neutralizer was mounted at 45 degrees opposite the collection windows on the plasma screen to facilitate optical access instead of at the nominal twelve o'clock position. New, NSTAR ion optics were aligned and installed. An electrode gap spacing of 0.06 cm was maintained over the breadth of the optics. Extended high-voltage stand-offs were added to accept EMT ion optics. In addition, 0.15 cm spacers were incorporated between the standoffs and

the anode to increase the anode to screen grid spacing since previous experience had shown that the soft Al 1100 structure tended to warp after operation resulting in a screen to anode short at high discharge powers (i.e. at high anode wall temperatures).

Thruster Performance

The FMT was operated over the entire NSTAR throttling range at GRC and at PEPL. The experimental facilities used for these tests will be described in the next chapter. Table 2.1 lists the complete range of throttling settings as a function of operating power.³ The thruster setting point in the first column will be used henceforth to refer to the discharge cathode and thruster operating conditions. The 12 A, 27 V case corresponds to the 2.3 kW operating condition of the 2000 hr wear test.

Table 2.1: DCA/FMT Operating Conditions.

Designation	J_D (A)	V_D (V)	P (kW)	\dot{m}_C (sccm)	\dot{m}_M (sccm)	TH
6 A	6.05	25.4	1.0	2.50	8.3	4
8 A	8.24	25.4	1.5	2.50	14.4	8
10 A	10.2	25.4	2.0	2.60	19.0	11
12 A, 25 V	12.1	25.1	2.3	2.90	24.0	-
12 A, 25 V, II	12.1	25.1	2.3	3.00	27.5	-
12 A, 27 V	12.1	26.8	2.3	3.00	23.0	2000 hr wear-test
12 A, 32 V	12.1	32.2	2.3	2.65	21.0	-
12.5 A	12.6	25.4	2.2	3.10	24.0	-
13 A, 25 V	13.1	25.1	2.3	3.70	24.0	15
13 A, 27 V	13.1	26.8	2.4	2.90	24.0	-
13 A, 27 V, II	13.1	26.8	2.4	3.70	22.5	-
13.5 A	13.6	25.1	2.3	3.20	24.0	-

Where: J_D = discharge current
 V_D = discharge voltage
P = thruster power

\dot{m}_C = discharge cathode flow rate
 \dot{m}_M = main flow rate
TH = NSTAR/DS1 throttling point

The 13 A, 25 V (TH 15) case corresponds to the 2.3 kW operating condition of the 8200 hr life test. Because it was unclear if the change in cathode flow rate had, in itself, significantly affected the erosion process, both \dot{m}_M and \dot{m}_C were varied in this investigation to achieve the same J_D and V_D . The cases which emphasized variations in \dot{m}_M are denoted with “II” after the current and voltage.

Figure 2.7 compares the overall thruster performance of the FMT to an EMT for the NSTAR throttling conditions. Again, the close agreement indicates that the erosion and plasma measurements made on the FMT are characteristic of NSTAR-type thrusters in general.

The FMT was also operated without beam extraction. Table 2.2 compares the discharge voltages as a function of discharge current for the same flow rates with and without beam extraction. The significantly lower V_D 's without beam extraction indicate that the plasma in the region of the DCA is significantly different in the two

Table 2.2: Comparison of discharge voltages with and without beam extraction.

\dot{m}_M (sccm)	\dot{m}_C (sccm)	J_D (A)	$V_D (J_B \neq 0)$ (V)	$V_D (J_B = 0)$ (V)
5.9	2.50	4.3	25.4	18.0
8.3	2.50	6.1	25.4	19.0
14.4	2.50	8.3	25.4	21.0
23.4	3.7	13.1	25.4	18.0
22.9	3.0	12.1	26.8	20.0

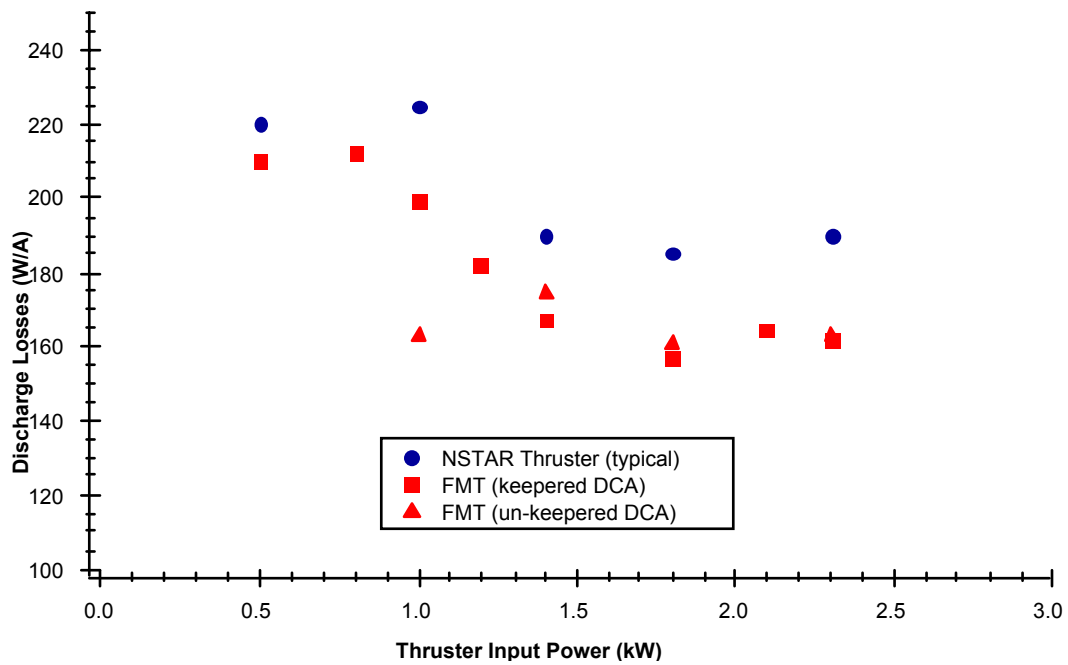


Figure 2.7 A comparison of the FMT's overall thruster performance to that of other ion engines.

cases. Ion data taken without beam extraction would not represent ion characteristics leading to DCA erosion under normal operating conditions.

Integration of the FMT at PEPL

In addition to the ion thruster, NASA Glenn provided a propellant feed system, a station-keeping ion thruster package (SKIT-Pac) power processing and control rack, and a soft-walled down-flow clean-room to enable ion thruster operation and maintenance at PEPL. The SKIT-Pac is shown in Fig. 2.8. The SKIT-Pac was



Figure 2.8 A photograph of the SKIT-Pac used to operate the ion thruster.

located in the PEPL control room which permitted simultaneous thruster control and visual monitoring of both the thruster and discharge chamber via video cameras. Telemetry consisted of 12 Fluke multi-meters which measured currents and voltages supplied to the FMT at the vacuum chamber flange. Figure 2.9 provides a schematic of the telemetry. The manually controlled propellant feed system was dedicated to ion thruster operation. NASA specifications for HCA and ion thruster operation were observed with this system.² The flow rates were periodically calibrated with a bubble flow meter.

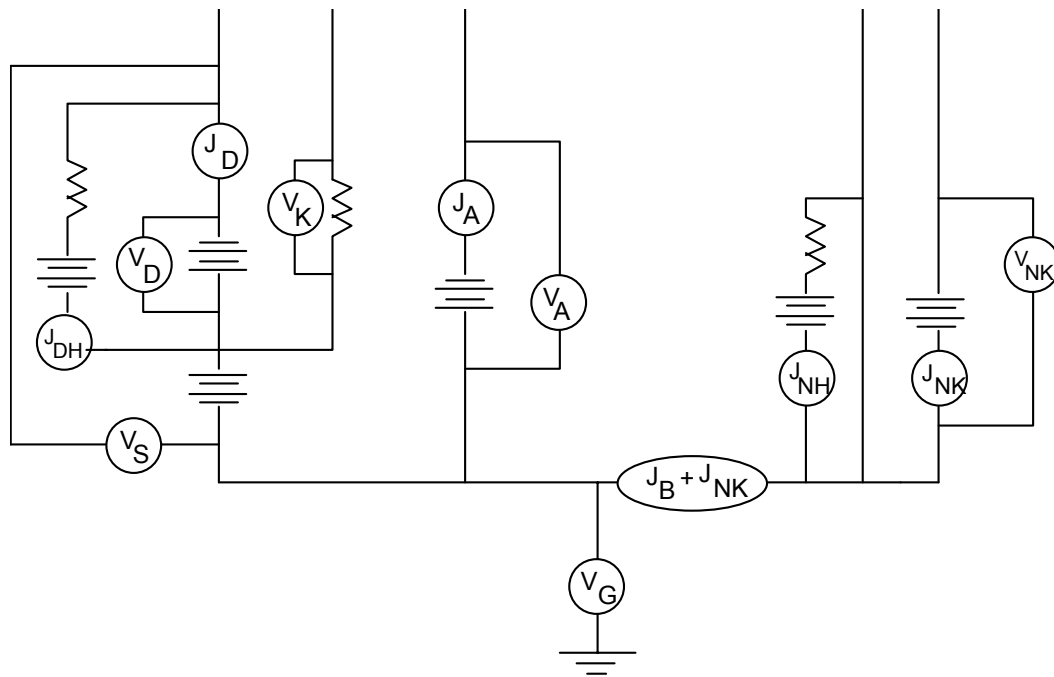


Figure 2.9 A schematic diagram of the ion thruster telemetry, where

J_B = Beam current,
 J_{DH} = Discharge heater current,
 J_D = Discharge current,
 J_A = Accelerator grid current,
 J_{NK} = Neutralizer keeper current,
 V_A = Accelerator grid voltage,
 V_D = Discharge voltage,
 V_K = Discharge keeper voltage,
 V_S = Screen grid voltage,
 V_G = Coupling voltage, and
 V_{NK} = Neutralizer keeper current.

Notes to Chapter 2

-
- ¹ Patterson, M.J., T.W. Haag, and G.J. Williams, “Derated Ion Thruster Development Status,” 29th Joint Propulsion Conference, AIAA-93-2225, (July, 1993).
- ² Patterson, M.J., et al, “Performance of the NASA 30 cm Ion Thruster,” IEPC-93-108, 23rd International Electric Propulsion Conference, (September, 1993).
- ³ Rawlin, V.K., et al., “NSTAR Flight Thruster Qualification Testing,” AIAA-98-3936, 34th Joint Propulsion Conference (July, 1998).
- ⁴ Patterson, M.J., et al., “2.3 kW Ion Thruster Wear Test,” AIAA-95-2516, 31st Joint Propulsion Conference (July, 1995).
- ⁵ Polk, J.E., et al., “A 1000-Hour Wear Test of the NASA NSTAR Ion Thruster,” AIAA-96-2717, 32nd Joint Propulsion Conference (July, 1996).
- ⁶ Polk, J.E., “An Overview of the Results from an 8200 Hour Wear Test of the NSTAR Ion Thruster,” AIAA-99-2446, 35th Joint Propulsion Conference (June, 1999).
- ⁷ Christensen, J., et al., “Design and Fabrication of a Flight Model 2.3 kW Ion Thruster for the Deep Space 1 Mission,” AIAA-98-3327, 34th Joint Propulsion Conference (July, 1998).

CHAPTER 3

EXPERIMENTAL APPARATUS AND THEORY

The apparatus and theory necessary to measure DCA erosion and plasma properties were first used to overcome several challenges that presented themselves prior to the investigation of the FMT DCA:

- Operation of a 30 cm NASA ion thruster at PEPL. (A flight-level ion thruster had never been operated at a university.)
- Development of a laser-induced fluorescence (LIF) diagnostic capability at PEPL
- Development of a multiplex Xe II LIF diagnostic capability (Ideal for ion velocity characterization, it had been successfully implemented only at the University of Tennessee Space Institute despite several attempts at other sites.¹⁾)
- Demonstration of Xe I and Xe II LIF in the plume of a hollow cathode assembly (HCA).

This chapter describes and presents the theory associated with the laser diagnostic techniques and apparatus (in addition to the FMT) used to meet these preliminary objectives and the principal objectives of measuring the DCA erosion rates

and the plasma properties near the DCA. A brief discussion of the uncertainty associated with the LIF and probe data is also provided.

Apparatus for propulsion system operation

Both an HCA and the FMT were operated during this investigation. A down-flow clean room was installed in a room adjacent to PEPL's main room containing the vacuum chambers. The FMT and HCA were stored in the clean area with N₂ purges on the cathodes. Periodic disassembly and assembly and maintenance were performed in this room. Personal clean attire (gloves, smock, hats, etc.) worn during assembly and handling followed requirements established by NASA Glenn.² The facilities and the HCA are described below.

The Cathode Test Facility

The cathode test facility (CTF) at PEPL was used to perform HCA tests. The CTF has an inside diameter of 60 cm and a length of 245 cm. A 41 cm diameter cryogenic vacuum pump maintained a high vacuum in the chamber during testing, with a base pressure of approximately $7 \cdot 10^{-6}$ Pa; a cold cathode gage measured the pressure. The pump speed on Xe was approximately 1500 L/s. The CTF propellant feed system was designed and maintained as closely as possible to the specifications established in the space station plasma contactor program.²

In all measurements, the HCA was moved with respect to the probes and to the point of LIF interrogation to permit interrogation of various points in the HCA plume. Two 30 cm translation stages (for axial and radial motion) and a lab jack provided three

degrees of freedom with stepper motor (for vertical motion). The jack was mounted to a plate bolted to rails on the wall of the CTF; the axial stage was mounted on the jack, and the radial stage was mounted on the axial stage. Figure 3.1 gives a schematic of the HCA in the CTF.

The Large Vacuum Test Facility

FMT interrogation was performed in the 6 m by 9 m large vacuum test facility (LVTF) at PEPL. Four CVI Model TM-1200 Re-Entrant Cryopumps provided a combined pumping speed of 140,000 l/s on xenon with a base pressure of less than $2 \cdot 10^{-7}$ Torr. The tank pressure during 2.3 kW operation was roughly $3 \cdot 10^{-6}$ Torr, corrected for xenon. The facility has since been upgraded to seven cryopumps for a xenon pumping speed of 240,000 l/s.

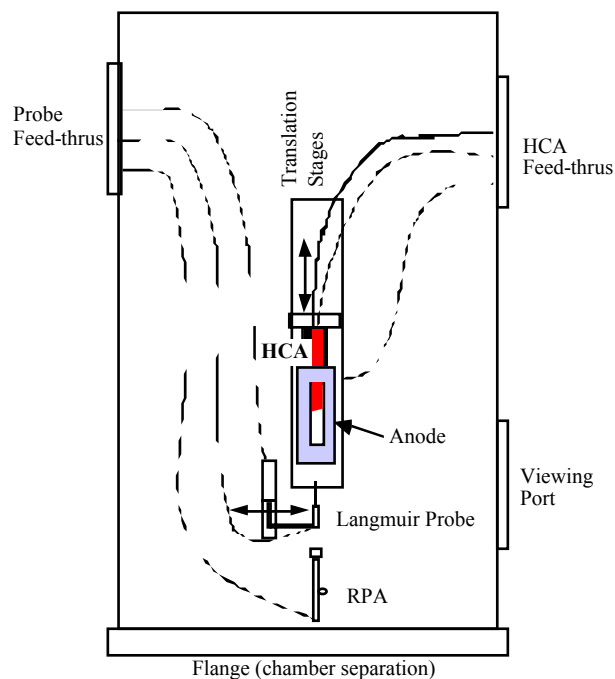


Figure 3.1 A schematic of the HCA in the CTF.

The FMT was mounted on a two-axis positioning system whose resolution was on the order of 0.025 cm. A 1.8 m by 2.5 m louvered graphite panel beam-dump protected windows downstream of the thruster and suppressed back sputtering. The panels were located roughly 4 m downstream of the thruster. Figure 3.2 gives a schematic for all measurements in the LVTF. The FMT was on thruster station 2.

The Hollow Cathode Assembly

A prototype space station contactor HCA (shown in Fig. 3.3) with a 0.635 cm diameter cathode of identical material to the cathode in the FMT DCA was used in the preliminary investigation. The HCA had a 25 percent smaller cathode orifice and had a permanent Mo keeper geometrically similar to that of the keeper used on the DCA.³

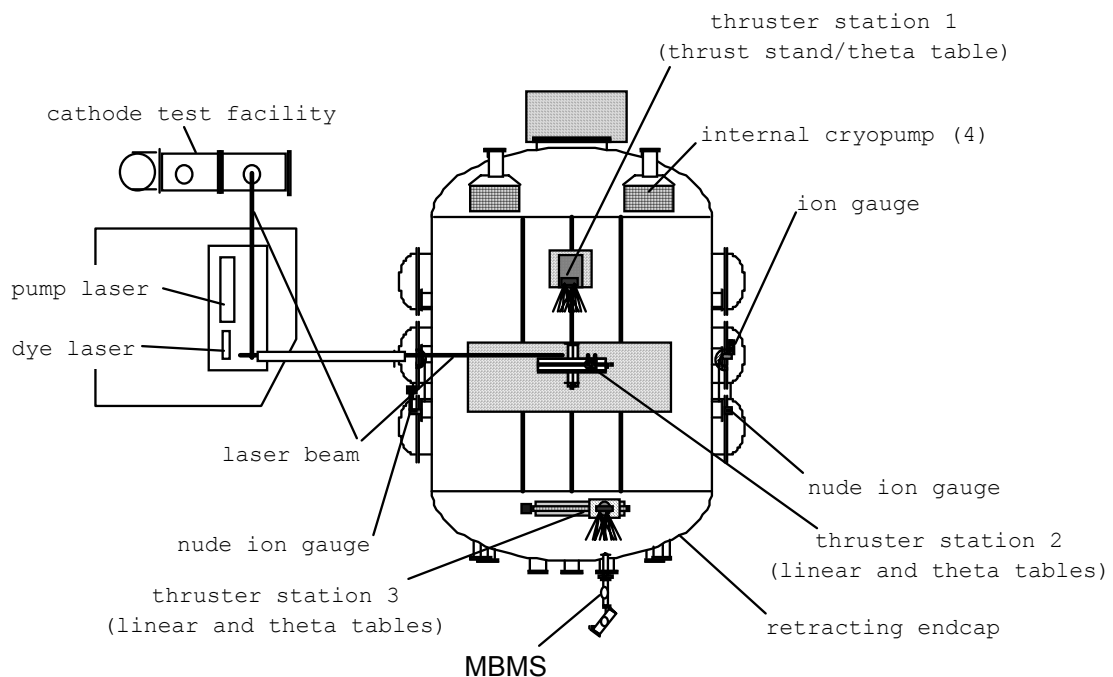


Figure 3.2 A schematic of the LVTF at PEPL.

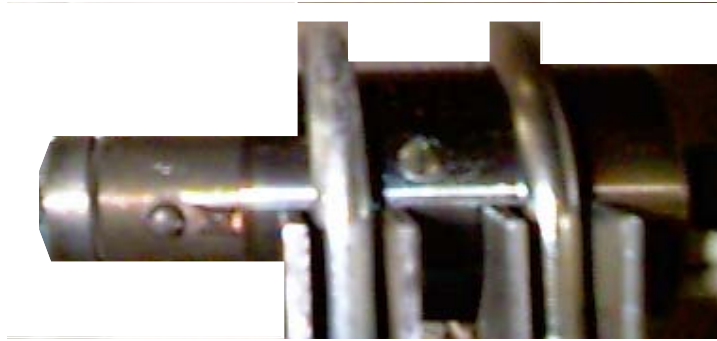


Figure 3.3 A photograph of the hollow cathode assembly.

The keeper-to-cathode gap was 0.2 cm. A cylindrical anode (shown in Fig. 3.4) was incorporated as a first approximation (note the absence of a magnetic field) to the discharge cathode environment of an ion engine. The 6.35 cm diameter of the anode was chosen to facilitate comparison of data with previous investigations of ion velocities.^{4,5} Four 7 cm axial slits cut into the anode facilitated observation of cathode operation, alignment of probes, and LIF measurements. Tests were performed with and without voltage applied to the anode electrode.



Figure 3.4 A photograph of the HCA anode.

HCA handling and conditioning followed procedures derived from experience with the Space Station Plasma Contactor program.⁶ These procedures ensured the best possible means to achieve similar cathode lifetimes, providing continuity to the research effort.

Laser-Induced Fluorescence

Laser-induced fluorescence (LIF) is the incoherent spontaneous emission of photons from an excited energy level (electronic in the case of xenon or other monatomics) populated by the absorption of photons from the laser. In general, the energies (wavelengths) of the absorbed and emitted photons are different. Indeed, emission may occur at many different wavelengths. As an example, the laser and fluorescing transitions for the 605 nm driven Xe II transition are given in Fig. 3.5.

The absorbing atom or ion will “see” the wavelength of the incoming photons shifted by the relative motion of the ion in the direction of the photon. This Doppler

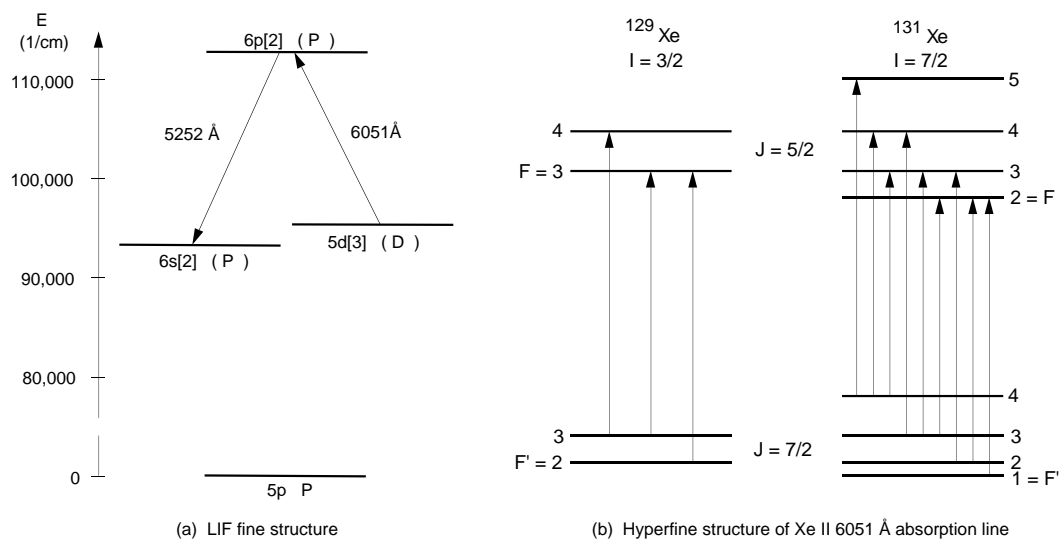


Figure 3.5 Energy levels and hyperfine structure for the 605—525 nm Xe II transition.

effect results in spectral line broadening due to the random thermal (Maxwellian) or artificial (accelerated) variations in absorber motion. It also results in a potentially large Doppler shift due to the bulk velocity of the interrogated species. In either case, the change in photon frequency $\Delta\nu$ is a function of the nominal transition frequency, ν_0 , and the velocity of the ion, v_i

$$\Delta\nu = \nu_0 \cdot \left(\frac{v_i}{c} \right). \quad (3.1)$$

Laser Selection

An argon-ion pumped Coherent dye laser (899-29 model) was selected to drive the LIF. The ion laser was an Innova R series laser with nominally 25 W broadband visible and 5 W broadband UV output. It enables relatively high-power UV dye (500 mW), visible dye (2 W), and infra-red/titanium-sapphire (2 W) operation. The principal advantages of the 899-29 system are the flexibility in wavelength associated with dye operation, the linewidth of the laser output which is nominally 0.5 MHz and is significantly smaller than most pulsed laser systems, the Autoscan computer control which permits tuning repeatability of 50 MHz and a scanning range of over 100 GHz, the demonstrated use of similar dye systems in similar plasma interrogations,¹ and the relatively high power of this system compared to diode systems.

The laser and optics shown schematically in Fig. 3.6 were located in a controlled atmosphere/low-dust enclosure. The beam from the dye laser was directed through the conditioning optics by high-reflecting, 2.5 cm diameter mirrors specially coated for either 380 to 450 nm or 450 to 700 nm operation. The beam was sampled

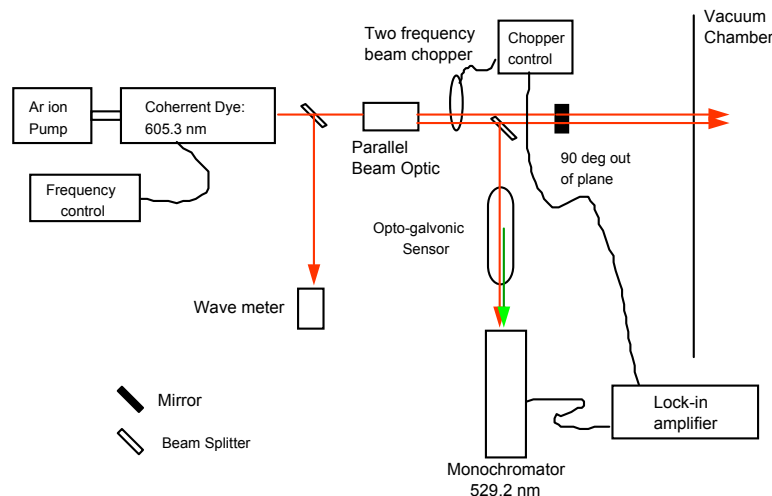


Figure 3.6 A schematic of the laser and beam conditioning optics at PEPL.

for wavelength and power measurement (not shown) by 2.5 cm square by 0.16 cm thick quartz slides. The Burleigh WA10000 wave meter had a resolution of 0.0001 nm and an accuracy of 0.001 nm between 400 nm and 10000 nm. The sampling beam was aligned to the wave meter using two 2.5 cm mirrors in periscope configuration. The parallel beam optics (as many as three but only one is shown in the figure to illustrate the path) consisted of a 2.5 cm diameter 50-50 beam splitter coated for 450 to 700 nm operation and a 2.5 cm diameter high-reflecting mirror. Fine adjustment, high-precision mounts were used to hold the beam splitter and the mirror to permit parallel alignment over a total path length of 10 m.

Calculations and previous investigations¹ have indicated that the natural fluorescence will be several orders of magnitude stronger than laser-induced fluorescence. One method of addressing this is to introduce an AC component to the induced fluorescence by chopping the laser beams. The strong DC natural fluorescence

could then be rejected through the use of phase-matched detection. Lock-in amplifiers have been used successfully to extract the weak LIF signal in Xe plasmas.¹

An Oriel two-frequency optical chopper chopped the beams downstream of the parallel beam optics. The frequency was fed directly from the chopper to the lock-in amplifiers, and the phase of the chopping was matched by maximizing the lock-ins' signals using laser scatter. Three Thor Labs LIA-100, two Stanford Research 8200, a Princeton Scientific 100 and a Stanford Research 8500 lock-in amplifiers were employed in various combinations. The three Stanford lock-ins were used for FMT erosion measurements because of their higher gain and better phase matching, and a Thor LIA-100 was used for all reference measurements. One of the chopped beams was sampled by another 2.5 cm quartz plate and the sampled beam was directed to the reference cell (see below) by 2.5 cm high-reflecting optics. The two primary beams were directed to the vacuum chamber by two 10 cm diameter, protected-silver mirrors. The large mirrors permitted variable beam spacing and out-of-plane beam spacing as will be discussed below.

A Hamamatsu opto-galvanic cell (model L2783-42XNe-Mo) was used as a reference cell.¹ The cell consisted of a 0.625 cm diameter, Mo tube cathode-anode pair centered in a 2.5 cm diameter by 10 cm long glass cylinder filled with xenon and neon in a 40:60 mixture. (The neon added stability to the cathode discharge.) The ends of the cylinder were angled approximately at Brewster's angles to minimize reflective losses. The cell was designed to permit a laser beam to pass through the cylinder and the electrodes. For neutral transitions of Ne, Xe, or of the electrode material (Mo) the voltage required to maintain a discharge at a given current will be reduced since the laser will excite the atoms and make them easier to ionize, thus indicating the

wavelength of the transition. However, in this investigation, the fluorescence induced by the laser passing through the plasma between the electrodes was collected through a monochromator onto a Hamamatsu 928 photo-multiplier tube (PMT) in exactly the same fashion as LIF would be collected from the devices interrogated in the vacuum chambers. A 2.5 cm diameter lens (not shown in Fig. 3.4) was used to collect the fluorescence. Occasionally, line filters were used to minimize the collection of laser scatter. Typically, the cell was operated at 440 V, 9 mA which yielded strong, stable Mo, Ne, Xe, and Xe II LIF signals. The temperature of the atoms and ions in the reference cell were estimated to be 800 K.¹³ Increasing the operating voltage of the reference cell increased the Xe II and Mo LIF signals but decreased the Xe I signal.

Multiplex LIF Technique

Laser-induced fluorescence measures the velocity parallel to the laser beam via a Doppler shift. Typically, a single beam is used for interrogation.^{7,8} To measure a velocity component, the laser is introduced along the axis of that component. This method requires significant rotational flexibility both in terms of the plasma source and in terms of optics survivability. If the thruster or HCA were moved between interrogation of velocity components, there is necessarily an uncertainty introduced in whether the beam is interrogating the same point as before. Equally, it is unclear that the same operating conditions are present in subsequent interrogations of the same point. For most cases this is less of an issue than the time required to measure each velocity component independently. The expense of operating the facility, the extended use of propellant, and potential optical coatings all increase by at least a factor of three. Single component internal LIF measurements would have required significantly greater

modifications to the thruster (*e.g.*, larger windows, more windows, a more versatile gimbal mounting, etc.).

The multiplex technique incorporates several beams that simultaneously measure several components of velocity.⁹ Proper alignment of the beams ensures that they interrogate the same point. The beams enter a lens parallel to each other and are crossed and focused at the focal point of the lens. Simultaneous measurement of all velocity components at the same location removes many of the problems associated with single beam interrogation. However, there are several issues associated with the multiplex technique. Instead of measuring the velocity components directly, the angled beams measure projections of the velocity components. Optics greater than 10 cm in diameter become prohibitively expensive which limits the angle of interrogation. In the case of a 30 cm ion thruster, the maximum angle of interrogation is roughly 13 degrees. As discussed below, the smaller the angle, the greater the sensitivity of the velocity measurement to the measurement of the angle. However, the advantages of limited thruster modifications to accommodate optical access and of significantly reduced test time outweigh the uncertainty introduced in the measurement.

The multiplex LIF technique was first demonstrated at PEPL on Xe II in an HCA plume in the CTF. The beams were delivered to the cathode test facility (CTF)

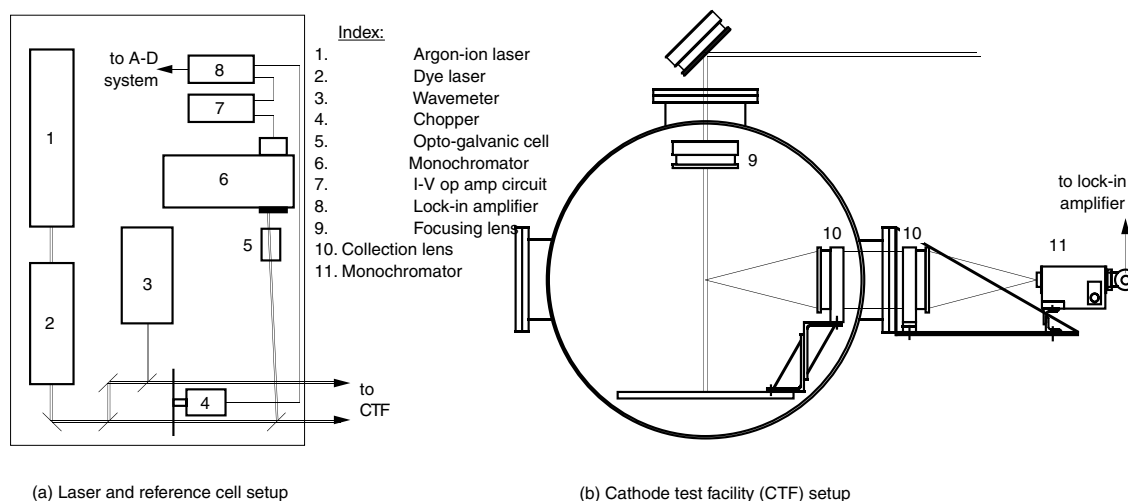


Figure 3.7 Beam delivery to the CTF.

and then to the cathode as shown in Fig. 3.7. The fluorescence from the cathode plume was collected by a monochromator with a Hamamatsu 928 PMT. Operational amplifier circuits converted the PMT current signals to voltage signals that could be input into an analog to digital data acquisition system. The Coherent 899-29 Autoscan software collected and matched the laser frequency to these signals. A Burleigh wave meter on loan from NASA Glenn was used to verify the frequency of the laser. The principal transitions used in this investigation are given in Table 3.1. Note that all of the species are interrogated in excited states.

Since the natural fluorescence is several orders of magnitude greater than the induced fluorescence, phase sensitive detection of the fluorescence was implemented by chopping the laser beams. Each beam used in the multiplex technique was chopped at a

Table 3.1: LIF Transitions.^{10,11}

Species	λ Laser (nm)	Term Symbols {Energy levels (eV)}	λ Fluorescence (nm)	Term Symbols [Energy levels (eV)]	I_{SAT} (mW/cm ²)
Xe I	582.389	$6s'[1/2]^{\circ}—5f[1\ 1/2]$ {9.45—11.57}	617.967	$6s'[1/2]^{\circ}—5f[1\ 1/2]$ {9.57—11.57}	100
Xe II	605.115	$5d^4D—6p^4P^{\circ}$ {11.83—13.89}	529.222	$6s^4P—6p^4P^{\circ}$ {11.54—13.89}	30
Mo	603.066	{1.06—2.49}	550.649	{0.93—2.49}	10
W	429.461	{0.25—2.26}	426.939	{0.25—2.27}	50

different frequency. Care was taken to avoid natural harmonics that cause aliasing. Lock-in amplifiers set to each of the chopping frequencies then isolated the components of these signals, separating the “axial” and radial components of the ion’s velocity.

The beams were split just downstream of the dye laser by a parallel beam optic as shown in Fig. 3.6. For the purposes of discussion, consider a two-beam multiplex configuration intended to measure azimuthal (radial on centerline) and axial velocity components as illustrated in Fig. 3.8. This was the configuration used in the CTF measurements and is readily extended to three or four beams as used in the LVTF.

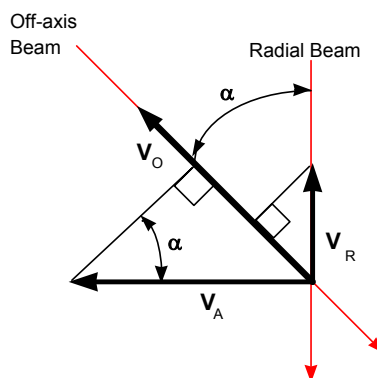


Figure 3.8 A schematic of multiple beam interrogation.

The parallel beams were crossed by a 10 cm diameter lens with a focal length of 25 cm as shown in Fig. 3.7. The beam passing perpendicular to the axis of the cathode directly measured the azimuthal component of velocity and is referred to below as the “vertical” beam. The other beam measured the velocity in the direction of the beam which has both azimuthal and axial components and is referred to below as the “off-axis” beam. The axial velocity component, v_A , can be deduced from the vertical velocity, v_v , and the off-axis velocity, v_o ,

$$v_A = \frac{v_o - v_v \cos(\alpha)}{\sin(\alpha)}. \quad (3.2)$$

A beam splitter and mirror were used together to form a parallel beam optic instead of a dedicated, single crystal block with coated surfaces as in previous investigations.¹ This provided significantly greater flexibility in beam spacing (from 1.0 to 3.5 cm) but introduced uncertainty into the beam spacing at the lens above the interrogation volume. Retro-reflection from the lens used to cross the beams insured that the beams were parallel from the beam splitters to the lens. A 10 cm square mirror was placed on the lens mount to yield the retro-reflection. Several measurements were made of the beam spacing at the lens and the standard deviation was used to estimate the uncertainty in the angles of interrogation.

Each of the laser beams yielded a fluorescence spectrum composed of Maxwellian distributions which have temperatures associated with them. However, as with the bulk velocity components, the spectrum produced by the “axial” beam has contributions of both axial and radial velocity distributions. Assuming statistical independence of the Maxwellian distributions associated with each velocity component,

the true axial temperature, T_A , can be calculated using the temperatures of the distributions in the radial, T_R , and off-axis, T_O , directions. This assumption yields an elliptical relationship between the temperatures:

$$\left(\frac{T_V}{T_A}\right)^2 \sin^2(\alpha) + \cos^2(\alpha) = \left(\frac{T_V}{T_O}\right)^2.$$

Solving for the axial temperature yields (for $\alpha \neq 0$ and $T_V \approx T_O$)

$$T_A = T_V \left[\frac{\left(\frac{T_V}{T_O}\right)^2 - 1}{\sin^2(\alpha)} + 1 \right]^{-1/2}. \quad (3.3)$$

Estimation of the ion or neutral temperature required a model of the fluorescence spectral lineshape. A first-order model was used.³ Some broadening mechanisms such as natural lifetime, collisions, and transit time were neglected because of the low density and the small resonance time of the excited states. The Xe I and Xe II models considered only Doppler broadening which assumes a Maxwell-Boltzmann velocity distribution. Averaging over the Doppler shift of each velocity component in the distribution yielded a Gaussian lineshape,¹²

$$g(v) = \frac{c}{v_0} \left(\frac{m}{2\pi kT} \right)^{1/2} \exp \left[-4 \ln(2) \frac{(v - v_0)^2}{\Delta v_D^2} \right]$$

where Δv_D is the full width at half maximum height (FWHM):

$$\Delta v_D = \frac{2v_0}{c} \left(\frac{2 \ln(2) kT}{m} \right)^{1/2}, \quad (3.4)$$

m is the mass of the ion or atom, and T is the kinetic temperature of the species.

Xe II LIF data from the low-temperature reference cell were fit with the sum of six Gaussian distributions. The magnitude and the wavelength at the center of each

Gaussian were chosen to optimize the fit and only coincidentally corresponded to the wavelengths and line strengths of Xe II fine structure. The line centers and relative line strengths of the Gaussians were maintained in all subsequent reduction of Xe II LIF data. This provided a fair approximation of the temperature. Centerlines and relative magnitudes for the Gaussian profiles used to fit Xe II, Xe I, Mo and W data are given in Table 3.2. A sophisticated model which incorporated isotopic and hyperfine structure was developed by Timothy Smith for the 605 nm—529 nm Xe II transition.¹³ There was excellent agreement between the two Xe II models.

Neutral density filters were periodically placed in the laser beam path to check for Mo LIF saturation; occasionally saturation effects were significant. To account for this, the Mo line shape model was modified to include a convolution of Gaussian and power broadened (partially saturated) line shapes. Saturation intensity can be approximated by¹⁴

$$I_{\text{SAT}} [\text{W} / \text{cm}^2] = \frac{hc}{2\sigma\lambda} A_{ji}, \quad (3.5)$$

Table 3.2: Parameters for Gaussian fitting of LIF data.

	Xe I	Xe II	Mo	W
Centerline				
Gaussian 1	582.54697 nm	605.28987 nm	603.23290 nm	429.79474 nm
Gaussian 2	582.54601 nm	605.29109 nm	603.23369 nm	429.79647 nm
Gaussian 3	582.54814 nm	605.28759 nm	603.23103 nm	429.79314 nm
Gaussian 4	582.54949 nm	605.28871 nm	603.23190 nm	-
Gaussian 5	582.54470 nm	605.29175 nm	603.23454 nm	-
Gaussian 6	582.54388 nm	605.29359 nm	603.22978 nm	-
Magnitude				
Gaussian 1	0.940	0.840	0.979	2.7
Gaussian 2	0.550	0.336	0.473	1.4
Gaussian 3	0.355	0.221	0.484	1.7
Gaussian 4	0.050	0.179	0.462	-
Gaussian 5	0.050	0.084	0.220	-
Gaussian 6	0.035	0.525	0.055	-

where the cross-section, σ , was approximated from tabulated spectral data.¹⁵

$$\sigma = A_{21} \frac{\lambda^2}{8\pi} g(v_o).$$

The Einstein A, A_{ij} , coefficient was taken from the literature.¹⁰ The power-broadened fluorescence lineshape, $\ell(v)$, takes the form¹⁴

$$\ell(v)[s] = \frac{\frac{\gamma}{2}}{(v - v_o)^2 + (\frac{\gamma}{2})^2 \left(1 + \frac{I}{I_{SAT}}\right)}. \quad (3.6)$$

The homogeneous relaxation rate, γ , is a combination of natural and collisional relaxation rates. As discussed below, the natural rate will dominate in the low-density environment near the DCA: $A_{ji} \approx \gamma$. The convolved spectrum yielded a more accurate estimate of the Mo temperature.

Calculation of Velocity and Energy Distributions

Since the data were fit assuming Maxwellian distributions, the bulk velocity corresponds to the mean velocity of the velocity distribution function. Bulk velocities were calculated using Eqns. 3.1 and 3.2 for each of the six Gaussians in the simple fits. About each of the bulk velocities, the velocity distribution was calculated via Eqn. 1, where Δv was now the difference between the frequency and the frequency of the center of the respective data fit, v_o . The energy distribution was calculated directly from the velocity distribution using the relation

$$E[eV] = \frac{mv_i^2}{2e}. \quad (3.7)$$

Density Measurements

The natural population of the lower state of the pump transition may vary with cathode operating condition. In order to correlate the LIF signal with the density of sputtered species, this variation must be taken into account. Note that the lower states of the Mo and W pump transition (given in Table 3.1) have direct transitions to the ground state.

The most straightforward approximation is to assume local thermodynamic equilibrium (LTE). The relative population of an excited state, n_i , is given by a Boltzmann relation.¹⁶

$$\frac{n_i}{n} = g_i \frac{\exp \left\{ \frac{E_i}{kT} \right\}}{Q(T)},$$

where the partition function, $Q(T)$, is

$$Q(T) = \sum_i g_i \exp \left\{ \frac{E_i}{kT} \right\}$$

The ratio of the populations of an excited state for different temperatures is then

$$\frac{n_i(T_2)}{n_i(T_1)} = \frac{Q(T_1)}{Q(T_2)} \exp \left\{ \frac{E_i}{kT_2} - \frac{E_i}{kT_1} \right\} \quad (3.8)$$

Electrons, because of their greater velocity, cause most of the collisional transitions which lead to equilibrium. In some plasmas, the electron density is small enough that radiative transition rates, especially de-excitation rates, become comparable to collisional transition rates. For the radiative decay rates to cause less than a ten percent deviation from LTE,

$$n_e n_j R_{CDij} \geq 10 n_j A_{ij} \quad (3.9)$$

where

$$R_{CDij} = 1.58 \cdot 10^{-5} \left(\frac{g_i}{g_j} \right) \frac{f_{ij} \langle G \rangle}{E_{ij} T_e^{1/2}} [\text{cm}^3 \text{s}^{-1}] .$$

The inequality can be simplified, and the assumption of LTE is valid if¹⁷

$$n_e \geq 1.6 \cdot 10^{12} T_e^{1/2} E_{ij}^3 \quad (3.10)$$

For an electron temperature of 2.5 eV, n_e on the order of 10^{15} cm^{-3} is required for the 603 nm Mo transition. An electron number density of 10^{12} cm^{-3} has been measured downstream of an HCA operating at 6 A with a flow rate of 3 sccm.¹⁸ As the discharge current of an ion thruster at 2.3 kW is typically 12 to 13 A,, the number density should be of the same order of magnitude. Therefore, LTE does not appear justified.

One alternative to the LTE model is the steady-state corona equilibrium (CE) model.¹⁹ Appropriate for low-density plasmas, this model assumes that radiative processes dominate the excited state relaxation, while the excitation is dominated by collisions. Because the number densities predicted just downstream of the DCA are on the order of 10^{12} cm^{-3} , this model can be used to relate the density of the excited state to that of the ground state.¹⁹ For coronal equilibrium, the rate of collisional excitation and radiative relaxation balance:

$$n_o n_e R_{oj} = n_j A_{oj} .$$

Solving for the ratio of the excited state to the ground state yields

$$\frac{n_o}{n_j} = \left[1.58 \cdot 10^{-5} n_e \left(\frac{g_o}{g_j} \right) \frac{f_{oj} \langle G \rangle}{E_{oj} T_e^{1/2}} \exp \left\{ \frac{E_{oj}}{T_e} \right\} \right]^{-1} A_{oj} . \quad (3.11)$$

The ratio of the populations of an excited state for two different temperatures is strictly a function of T_e :

$$\frac{n_i(T_{e2})}{n_i(T_{e1})} = \left(\frac{T_{e2}}{T_{e1}} \right)^{1/6} \exp \left\{ \frac{-E_{ij}}{kT_{e2}} + \frac{E_{ij}}{kT_{e1}} \right\} \quad (3.12)$$

Unfortunately, each of these models, LTE and CRE, is a function of T_e which cannot be measured via LIF. In situ measurement of T_e near the DCA by electrostatic probes such as Langmuir probes was beyond the scope of this investigation. However, T_e can be approximated using an empirical fit to 30 cm ion thruster data^{20,21} as a function of discharge voltage, V_d ,¹⁷

$$T_e[\text{eV}] = \frac{1}{0.09} \ln \left(\frac{V_d}{20.0} \right). \quad (3.13)$$

Equation 3.12 predicts T_e to vary between 2.0 and 5.3 eV for discharge voltages between 24 and 32 V. No variation in T_e across the plume of the DCA is possible without probe data. Equations 3.12 and 3.13 were used to correct the LIF signal obtained at different discharge voltages for variations in the population of the excited state which might otherwise be interpreted as variations in the overall population of sputtered material.

Uncertainty in LIF Measurements

There are many sources of uncertainty in the data and its analysis. The principal source of uncertainty enters during fitting of the LIF data. A best fit is determined by visually or mathematically minimizing the deviation of the fit from the data especially within the FWHM portion of the distribution. In part, this uncertainty resulted from noise in the LIF spectra itself. Effects of saturation, empirical fits, and non-ideal distributions also added inaccuracies in the fits. Several steps were undertaken to minimize this error including averaging up to 14 sets of raw data at each point of

interrogation, introducing an offset in the magnitude of the LIF data to permit averaging of fluctuations, averaging data with different time constants to check for artificial broadening and shifting of the signal, reducing the same data with different routines (numerical optimization, visual optimization, or a combination of the two), and repeating the collection of data at the same condition and location. While these efforts did not remove the uncertainty, they did reduce it and did permit estimation of the error introduced through the fitting of the data:

- 5% error in the Doppler shift of all data
- 10% error in identification of peak values in the Mo data
- 20% error in identification of peak values in the W data
- 500 K error in temperatures in all species.

Some data were more noisy than others, but these values represent the error associated with the vast majority of the data. In general, the noise of the reference cell signal was very small and the fit could be made with a high degree of confidence. However, the experimental uncertainty of the frequency associated with zero velocity was amplified by the angle of interrogation (Eqn 3.2). The uncertainty in the Doppler shift considering both plasma and reference cell data was on the order of 500 to 1000 m/s. For large velocities, this may be negligible or superceded by uncertainty introduced by the angle of interrogation.

Another uncertainty also introduced uncertainty into the calculation of Xe II velocities and temperatures. The angles of interrogation are known within roughly 10 percent. From Eqn. 3.2, for small angles, the uncertainty in the angle is directly transferable to the uncertainty of the axial velocity. From Eqn. 3.4, the temperature will reflect roughly twice the uncertainty of the angle for small angles, or roughly 20 percent.

Lastly, the uncertainty in spectral constants and in T_e introduced a substantial uncertainty in the correction of LIF signal for variation in the population of excited states due to fluctuations in the discharge voltage. An uncertainty of 20 percent was given to all erosion data requiring the correction (i.e. for all data for which V_D varied).

Electrostatic Probe Theory

Langmuir probes were used to interrogate the HCA plasma to corroborate and augment LIF data. These probes were subject to four “sheath” effects: deviation from quasineutrality, plasma density perturbation, ion density depletion, and electron energy perturbation.²² Density disturbances depend on the solid angle at which the ion can impact the probe. In general, if the probe radius and sheath thickness are significantly less than the mean free path, this effect is negligible. Similarly, if the sheath thickness is much smaller than λ_m , which implies there are no collisions in the sheath, the deviation from quasineutrality can be neglected.²² To accurately measure the energy distributions, the probe radius must also be much smaller than the mean free path.²² This arises from the fact that ion depleting collisions with the probe must be replaced in the local plasma by collisional ionization or ion flux.

Two Langmuir probes with 0.025 cm diameter tungsten wire collectors were used in a planar probe configuration to eliminate probe radius effects, *i.e.* the wire did not extend beyond the end of the insulator. A guard ring electrode (roughly 0.25 cm in diameter, 0.04 cm thick and 2 cm exposed length) was used initially. This shield was ramped to the same voltage as the probe. The driving and signal collection circuits are given in Fig. 4. During testing, it was noted that the shield had no noticeable effect on

the data. (It was verified that a signal could be collected through it. Indeed, it provided excellent current vs. voltage traces at several centimeters from the cathode.)

The second probe was constructed subsequent to initial testing in order to provide interrogation within 0.5 cm of the HCA. The guard ring was eliminated to minimize perturbation of the plasma. In other respects, it was identical to the first probe. Also, erosion of the probe in this high-density, high-temperature region could affect both probe and cathode operation. Erosion was observed on the shield of the large probe and use of this probe was subsequently restricted to regions greater than 0.5 cm downstream of the keeper orifice.

The ion-ion mean free path can be expressed as a function of mean velocity and collision frequency²³

$$\lambda_m = \frac{\bar{v}}{v_i}. \quad (3.13)$$

The mean velocity can be inferred from the ion saturation current, J_{iSAT} :

$$\bar{v} = \frac{4J_{iSat}}{eAm_i}. \quad (3.14)$$

The collision frequency is a function of electron temperature and number density,

$$v_i = 1.8 \cdot 10^{-9} \sqrt{\frac{m_e}{m_i}} \frac{n_e}{T_e^{3/2}}, \quad (3.15)$$

and the sheath thickness²² can be approximated as

$$h[\text{cm}] \sim 6.9 \left(\frac{T_e}{n_e} \right)^{1/2}. \quad (3.16)$$

Similarly, the Debye length can be expressed²⁴

$$\lambda_D = \left(\frac{kT_e}{4\pi n_e e^2} \right)^{1/2}. \quad (3.17)$$

For Xe, $n_e = 10^{12} \text{ cm}^{-3}$, $T_e = 2.5 \text{ eV}$ and $A = 0.13 \text{ cm}^2$ the values of these parameters are $\lambda_m = 4 \text{ cm}$, $h = 5 \bullet 10^{-3} \text{ cm}$, and $\lambda_D = 1.2 \bullet 10^{-3} \text{ cm}$.

Parameters were obtained under the following assumptions: infinite, quasineutral and homogeneous plasma, Maxwellian electron and ion populations with $T_e \gg T_i$, electron and ion mean free paths much greater than probe or sheath dimensions, charged particles collected at the probe surface without reflection or reaction, and sheath size small compared to probe dimensions. These assumptions yielded the following relations:

$$T_e [\text{eV}] = \left[\frac{d(\ln I_e)}{d(V_{Pr})} \right]^{-1}$$

$$V_p = V_{Pr} \left(\frac{d(I_{Pr})}{d(V_{Pr})} = \text{maximum} \right) \quad (3.18)$$

$$n_e [\text{cm}^{-3}] = \frac{I_{Pr}(V_p)}{eA_{Pr}} \left(\frac{2\pi m_e}{kT_e} \right)^{1/2}.$$

Data generated by these relations provided insight into the HCA plume. Unfortunately, no probe data were collected in the FMT.

In general, the error introduced by the method of data reduction (a few percent) was significantly less than the errors introduced phenomenologically and by the noise of the data. Errors of roughly ten percent are assumed with respect to determination of electron temperature which corresponds to the well established error for T_e measurement.²⁵ The error associated with electron number density is significantly larger and the data may well be off by 50 percent.^{25,26}

Notes to Chapter 3

-
- ¹ Keefer, D., et al., “Multiplexed Laser-Induced Fluorescence and Non-Equilibrium Processes in Arcjets,” AIAA-94-2656, 25th Plasmadynamics and Lasers Conference (July, 1992).
- ² Sarver-Verhey, T.R., “Extended Test of a Xenon Hollow Cathode for a Space Plasma Contactor,” NASA Contractor Report 195402, November, 1994.
- ³ Williams, G.J., et al, “Laser-Induced Fluorescence Characterization of Ions Emitted from Hollow Cathodes,” AIAA-99-2862, 35th Joint Propulsion Conference (June, 1999).
- ⁴ Friedly, V.J., and P. J. Wilbur, “High-Current Hollow Cathode Phenomena,” *Journal of Propulsion and Power*, **8** (3) 1992, 635–643.
- ⁵ Siegfried, D.E., and P.J. Wilbur, “An Investigation of Mercury Hollow Cathode Phenomena,” AIAA-78-705, 13th International Electric Propulsion Conference, (April, 1978).
- ⁶ Sarver-Verhey, T.R., “Extended Test of a Xenon Hollow Cathode for a Space Plasma Contactor,” NASA Contractor Report 195402, November, 1994.
- ⁷ Cedolin, R.J., et al., “Laser-Induced Fluorescence Diagnostics for Xenon Hall Thrusters,” AIAA-96-2986, 32nd Joint Propulsion Conference, (July, 1996).
- ⁸ Hargus, W.A., and M.A. Cappelli, “Interior and Exterior Laser-Induced Fluorescence and Plasma Potential Measurements on a Laboratory Hall Thruster,” AIAA-99-2721 (June, 1999).
- ⁹ Ruyten, W.M., and D. Keefer, “Two-Beam Multiplexed Laser-Induced Fluorescence Measurements of an Argon Arcjet Plume,” *AIAA Journal*, **31** November, 1993, 2083–2089.
- ¹⁰ Striganov, A.R., and N.S. Sventitskii, *Tables of Spectral Lines of Neutral and Ionized Atoms*, Plenum, New York, 1968, pp. 571–607.
- ¹¹ Corliss, C.H., and W.R. Bozman, *Experimental Transition Probabilities for Spectral Lines of Seventy Elements*, National Bureau of Standards Monograph 53, 1962, pp. 195–219 and 499–519.
- ¹² Eckbreth, A.C., *Laser Diagnostics for Combustion Temperature and Species*, Abacus Press, Cambridge, 1988, pp. 72–73.

-
- ¹³ Williams, G.J., et al., “Laser Induced Fluorescence Measurement of the Ion Energy Distribution in the Plume of a Hall Thruster,” AIAA-99-2424, 35th Joint Propulsion Conference, (June, 1999).
- ¹⁴ Miles, R., “Lasers and Optics,” Course notes, Princeton University, 1995.
- ¹⁵ Verdeyn, J.T., Laser Electronics, 3rd ed., Prentice-Hall, 1995, p. 216.
- ¹⁶ Griem, H.R., *Plasma Spectroscopy*, McGraw Hill, New York, 1964, pp. 129–160.
- ¹⁷ Rock, B.A., “Development of an Optical Emission Model for the Determination of Sputtering Rates in Ion Thruster Propulsion Systems,” Ph.D. Dissertation, Arizona State University, 1984, pp. 43–59.
- ¹⁸ Williams, G.J., et. al., Near-Field Investigation of Ions Emitted from a Hollow Cathode Assembly Operating at Low-Power,” AIAA-98-3658, 34th Joint Propulsion Conference (July, 1998).
- ¹⁹ Huddleston, R.H., and S.L. Leonard, *Plasma Diagnostic Techniques*, Academic Press, New York, 1965, pp. 208–214.
- ²⁰ Poeschel, R.L., and J.R. Beattie, “Primary Electric Propulsion Technology Study,” NASA CR-159688, 1979.
- ²¹ Poeschel, R.L., “2.5 kW Advanced Technology Ion thrusters,” NASA CR-135076, 1976.
- ²² Schott, L., “Electrical Probes,” *Plasma diagnostics*, W. Lochte-Holtgreven ed., American Institute of Physics, New York, pp. 668–725.
- ²³ Jahn, R.G., *Physics of Electric Propulsion*, McGraw-Hill, New York, pp. 45–65.
- ²⁴ Hubin, J.D., *NRL Plasma Formulary*, Office of Naval Research, 1998.
- ²⁵ Hutchinson, I.H., *Principles of Plasma Diagnostics*, Cambridge University Press, 1987, pp. 62–66.
- ²⁶ Domonkos, M.T., et al., “Low Current Hollow Cathode Evaluation,” AIAA-99-2575, 35th Joint Propulsion Conference (June, 1999).

CHAPTER 4

LASER-INDUCED FLUORESCENCE CHARACTERIZATION OF THE PLUME OF A HOLLOW CATHODE ASSEMBLY

Hollow cathode operation in the cathode test facility provided a less complicated environment to validate PEPL's LIF diagnostic capability than ion thruster operation in the large vacuum test facility. The CTF was less expensive to operate and also provided greater flexibility in laser delivery and signal collection and greater control over the interrogation volume. The objectives of this preliminary investigation included

- Demonstrating an LIF diagnostic capability
- Demonstrating LIF velocimetry in an HCA plume
- Comparing LIF measurements with probe measurements including probe measurements of high-energy ions in other HCA experiments
- Establishing a data base of HCA characteristics for comparison to ion thruster discharge cathode characteristics to determine in part whether operation of a ion thruster with beam extraction is necessary to evaluate discharge cathode erosion phenomena.

Phenomenological HCA Plume Characteristics

The operating conditions of the HCA with an anode were chosen to present a mix of spot- and plume-modes. Spot-mode emission is characterized by a bright spot at the downstream end of the orifice and negligible current and voltage oscillations. The efficiency of ionization within the cathode in spot-mode is hypothesized to be sufficient to emit ions to neutralize the plasma in the cathode-to-keeper gap. Hence, there is no evidence of electron-impact ionization in the gap. In contrast, plume-mode emission exhibits both a luminous plume downstream of the cathode and large current and voltage oscillations at several megahertz typically. Plume-mode operation is postulated to result from insufficient plasma production in the cathode, and consequently, the discharge is maintained through electron-impact ionization in the cathode-to-keeper gap.¹ Experimental observation of the luminous plume and an increase in discharge voltage support this theory of plume-mode operation.² Both modes are also present in un-keepered operation with the anode serving as the electron collector.

The cathode-to-keeper gap has a major impact on the amplitude of the discharge noise, the anode potential required to extract a given current in a diode geometry, and on external plasma parameters.³ There is considerable evidence that this HCA behavior is more benign when used in a gridded ion thruster, possibly due to the influence of the higher gas pressure within the discharge chamber and to the presence of the magnetic field. The mean energy of ions emerging from the cathodes appears to increase as the discharge current is increased, ambient pressure is reduced, or cathode flow rate is reduced. Higher discharge currents, lower ambient pressures, and higher cathode flow rates increases the ion population in the high-energy tails of the distributions.⁶

Previous investigations have shown that the ion energy distributions are similar in shape for keepered and un-keepered operation, but the number density on centerline is less for un-keepered operation for the same discharge current up to 10 A. Above 10 A, the mean-energy data suggest that the character of the discharge changes significantly going from plume to beam-mode (typically a transition mode from spot to plume-mode).⁶ The results suggested that the keeper may serve to focus and to guide ions created near the cathode orifice along the centerline. Cases were selected to span the different operating modes to provide preliminary data for future ion thruster measurements.

Xe II Laser-Induced Fluorescence

The initial Xe II LIF was intended to demonstrate LIF capability, to validate data reduction methods, to provide a first insight into ion velocities near an HCA, and to provide some correlation between previous electrostatic analyzer (ESA) data and Langmuir probe data.^{2,4,5} Spatial resolution of the LIF measurements was roughly 1 cm.³ As discussed above, the uncertainty in the velocimetry was roughly 20 percent. Table 4.1 summarizes HCA operating conditions used in this investigation.

Velocity Measurements

Because the LIF signal strength was optimized at most points of interrogation, the data are presented in a self-normalized format. Periodically, a polarizer was

Table 4.1: HCA operating conditions.

Designation	Keeper Current (A)	Keeper Voltage (V)	Anode Current (A)	Anode Voltage (V)	Mass Flow Rate (sccm)	Facility Pressure (Pa)
4 A, plume-mode	4.03	13.07	-	-	2.3	$2.0 \cdot 10^{-3}$
4 A, spot-mode	4.03	11.61	-	-	4.0	$4.1 \cdot 10^{-3}$
6 A, spot-mode	2.15	10.24	4.00	16.90	4.0	$3.9 \cdot 10^{-3}$
6A, plume-mode	0.00	0.00	6.05	28.1	4.0	$4.0 \cdot 10^{-3}$

used to vary the power of the laser beam upstream of the first beam splitter as a check for saturation and power broadening. Neither saturation or power broadening was observed in the Xe I or the Xe II data.

Figure 4.1 shows fluorescence data collected during an LIF interrogation 5 mm downstream of the keeper of the HCA operating in a 6 A spot-mode. The trends in Fig. 4.1 were typical of data taken at all locations and operating conditions of the

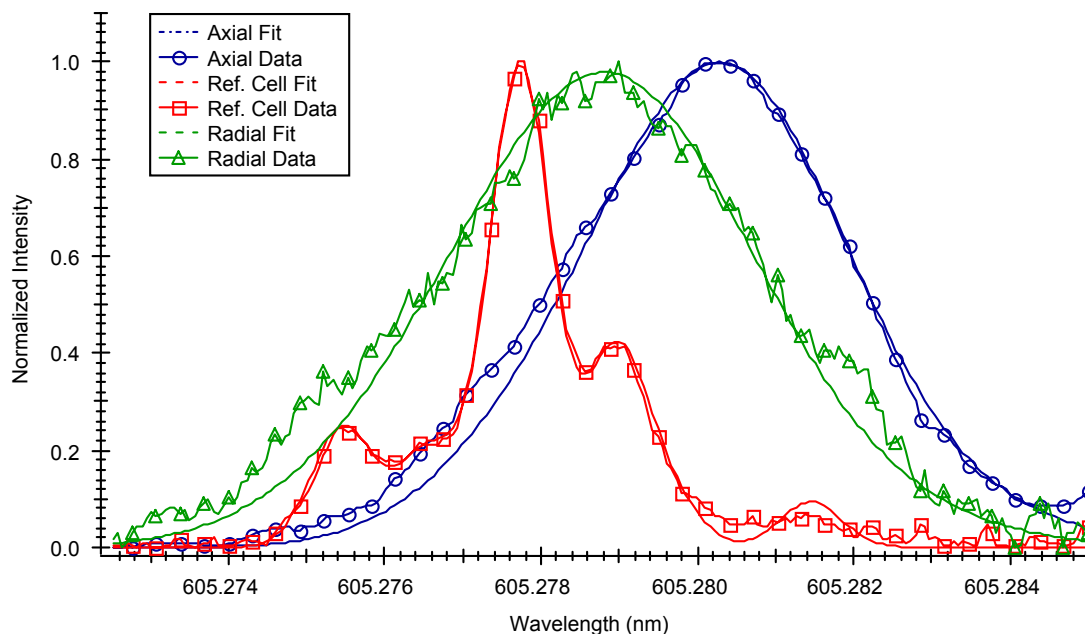


Figure 4.1 Typical Xe II LIF scan data of the 1/4" HCA. Data shown were taken 5 mm downstream of the keeper in 6 A spot-mode operation.

HCA. The slight offset of the radial signal relative to the reference signal indicates that the point of interrogation was slightly above the centerline of the cathode orifice. The effects of this were taken into account in reducing the axial component of the velocity via Eqn. 3.2. The relatively well-defined peaks facilitated the calculation of bulk speeds. The axial velocity and energy distributions for the data of Fig. 4.1 are given in Figs. 4.2 and 4.3 respectively. Maxwellian distributions were assumed as a first approximation and the distributions were calculated given the bulk-mean velocity and temperature from the LIF measurements. As stated in the previous chapter, LTE is not strictly justified, but the resolution of the deviation from Maxwellian is beyond the capability of the simple curve fitting model. A more sophisticated model will be used in the reduction of FMT data. The calculated values are presented here to illustrate nominal spreads in velocities and energies. Note that the FWHM of the

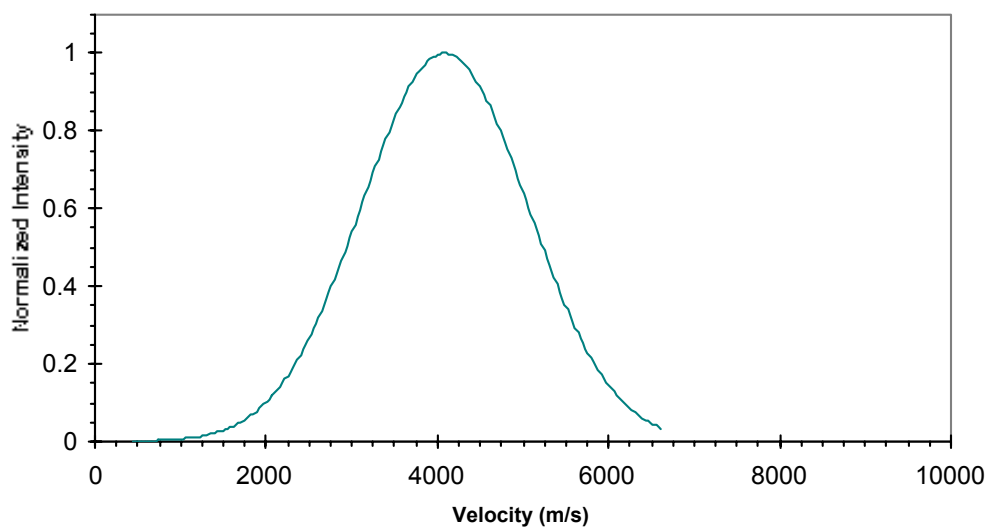


Figure 4.2 Typical Xe II axial ion velocity distribution. Data shown were taken 5 mm downstream of the keeper of the 1/4" Contactor HCA in 6 A spot-mode operation.

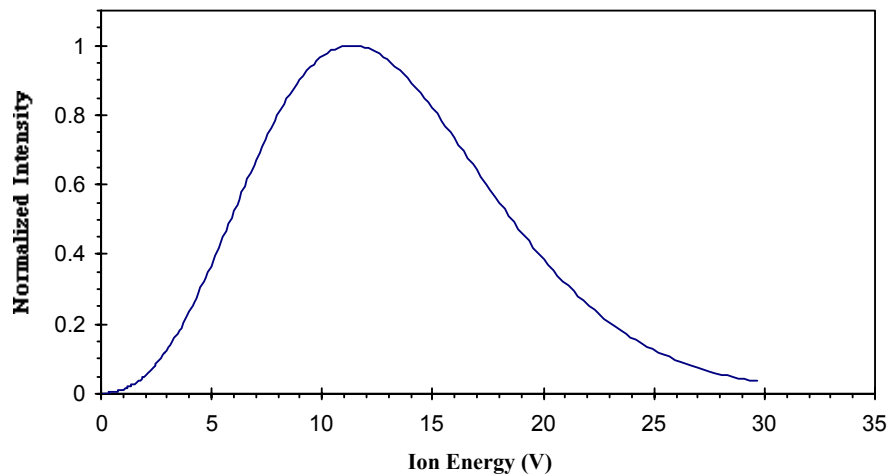


Figure 4.3 Typical Xe II axial ion energy distribution. Data shown were taken 5 mm downstream of the keeper of the 1/4" Contactor HCA in 6 A spot-mode operation.

energy distribution is nearly 8 V and that axial ion energies up to 30 V were detected even though the cathode-to-anode gap voltage was 16.9 V.

Figure 4.4 gives the centerline axial velocity components for the four HCA operating conditions. Note that there was a significant rise in the velocity of the ions a

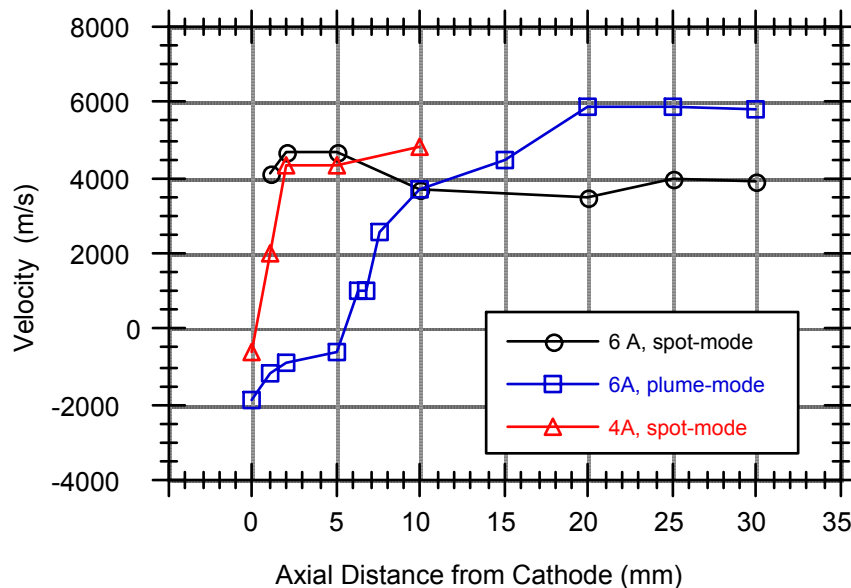


Figure 4.4 Centerline Xe II axial velocities for the HCA over various operating conditions.

few centimeters downstream of the keeper face in all cases. No variation in axial speed ± 0.5 and 1.0 mm off centerline was observed. This symmetry existed in both plume and spot modes. The smaller velocities near the HCA probably indicate the region of primary ionization. Note that there are back-flowing ions in the 6 A plume-mode and 4 A spot-mode cases, though they are much more pronounced in the plume-mode case.

The observation of higher-energy ions in both spot-mode and plume-mode is consistent with several previous investigations.^{6,7} As expected, the peak energy was higher for the ions generated in plume-mode (higher electron temperature and lower flow rate for the same current). The relative axial peak locations were also consistent with previous Langmuir probe measurements.⁸ The low velocities near the keeper may indicate a pre-acceleration region very near the keeper orifice. This phenomenon may result from the very high density of ions near the orifice in the spot-mode. This will be discussed at length in Chapter 6.

Temperature Measurements

While the magnitudes of each distribution are normalized in Fig. 4.1, the line widths reflect the actual thermal spreads in the data. Note that much of the structure observed in the reference cell signal is not present in the HCA data. Significantly reducing laser power in each beam did not reduce the line widths and did not reveal more structure. Reducing the lock-in time constants and increasing the time of the laser scan also had no effect which implied no artificial broadening was present and increased confidence in the temperature measurements is warranted.

The temperatures associated with each of the three signals were calculated by the model described in Chapter 3. The fits are shown in Fig. 4.1 as dashed lines.

Failure of the model to fit more closely in the wings may result from the non-physical nature of the model, a non-Maxwellian distribution of ion velocities, noise amplified in the normalization, or some combination of these. Figure 4.5 gives the Xe II temperatures associated with the axial and radial measurements. The error bars reflect a ten percent uncertainty in fitting the data. The temperatures for spot-mode operation are roughly constant, varying between 0.5 and 1.5 eV. In plume-mode, the axial temperatures are larger and decrease significantly with axial position. The narrowing of the profiles (decreasing temperatures) most likely resulted from the migration of lower-energy ions from the centerline, leaving a narrower distribution of higher-energy ions. Note that the axial velocity magnitudes were significantly higher than the radial.

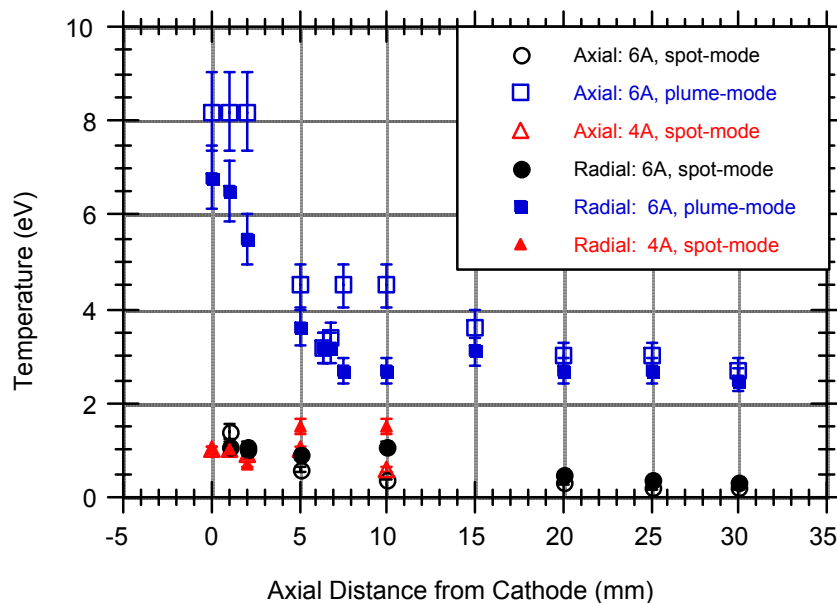


Figure 4.5 Xe II temperatures measured at different axial positions over various operating conditions of the HCA.

Xe I Laser-Induced Fluorescence

The temperature of neutral xenon, Xe I, was measured using LIF. Figure 4.6 shows a typical Xe I LIF scan. Note the virtual overlap of the radial, axial, and

reference profiles, implying that the bulk velocity of the neutrals was very small. The neutral signal was very strong in plume mode and very weak in spot mode. Xe I and Xe II temperatures are compared in Table 4.2. Note that the Xe I temperatures are significantly lower than the Xe II temperatures, but the Xe I temperatures (between 2000 and 5000 K) are much higher than measured cathode tube temperatures of roughly 1000 K for 4 A operation.²

A separate analysis of the internal HCA phenomena may provide a theoretical explanation for the high heavy particle temperatures observed in this investigation.⁹ Internal pressures greater than 10 kPa were measured which are an order of magnitude greater than would be expected if the heavy particle temperatures were in equilibrium with the cathode surfaces.² The pressures were however, consistent with the values reported by Salhi¹⁰ scaled to the ratio of orifice areas. A pinch effect in the orifice of the hollow cathode was hypothesized to generate both the high internal pressures and high neutral temperatures downstream of the orifice since the pressure and the temperature would be related by an equation of state.⁹

Theories of high-energy ion production

High-energy ions have been observed downstream of HCA's.^{11,12,13} One model describing the production of these ions proposes a “potential-hill” downstream of the cathode.¹³ This model suggests a region of substantial ion production resulting from

Table 4.2 A comparison of Xe I and Xe II temperatures 0.05 cm downstream of the HCA.

Cathode Condition	Xe I	Xe II
4 A spot-mode	-	12,500 K
6.0 A spot-mode	2250K	11,600 K
6.0 A plume-mode	5000 K	40,600 K

electron impact ionization creates a region of high-potential. The ionization results in regions of high ion density. In order to maintain quasineutrality, a potential hill develops to prevent the more mobile electrons from leaving the region.¹⁴ Ions leave the region with slow velocity but are accelerated through the gradient in potential so that at the base of the hill, they may have high velocities. Figure 4.7 illustrates the projected plasma and ion parameters indicative of a potential-hill.

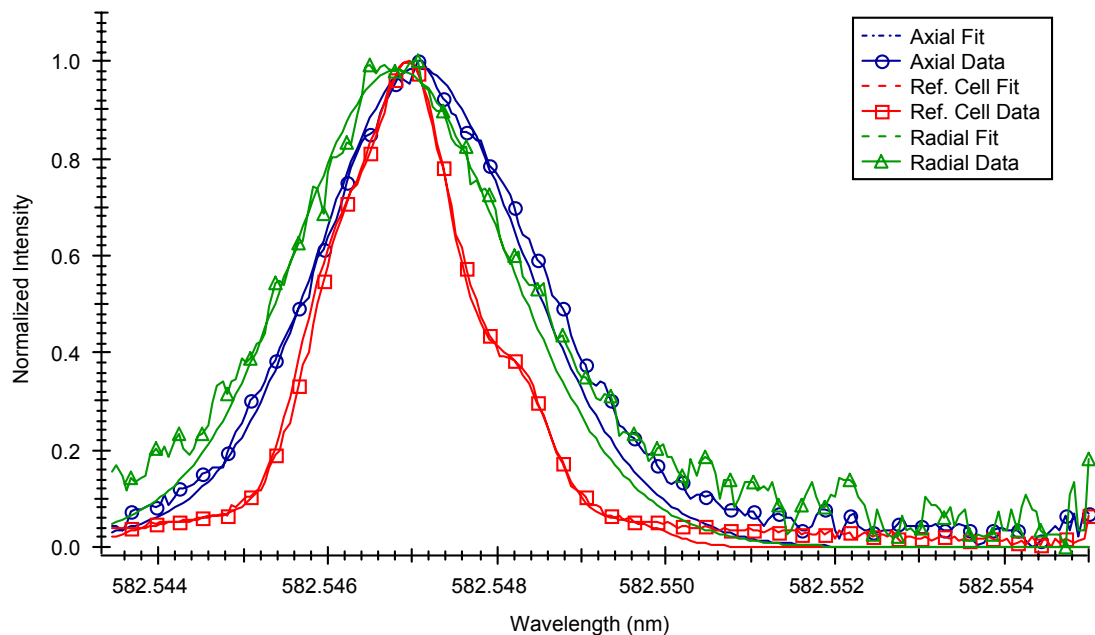


Figure 4.6 Typical Xe I LIF scan data of the HCA. Data shown were taken on centerline, 0.0 mm downstream in plume-mode operation.

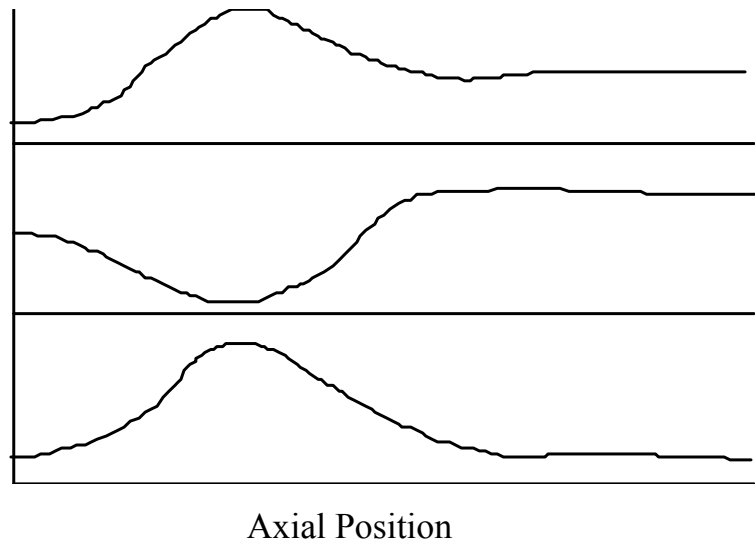


Figure 4.7 A schematic representation of the effects of a potential-hill.

A second model suggests the high-energy ions result from a magnetoplasdynamic (MPD) effect associated with high-current densities near the orifice.¹⁵ In this model, the high-energy ions are accelerated by the Lorentz force resulting from the self-induced magnetic field and the arc/discharge current in much the same way ions are accelerated in an MPD thruster. Considering the electrode diameters to be those of the cathode and keeper orifices, the electric field would have a significant radial component. A self-induced azimuthal magnetic field would result from the axial current emanating from the cathode orifice. This effect would be characterized by an almost instantaneous acceleration (jump) to a high velocity. The acceleration is provided both by the cross product of the radial arc current with the azimuthal magnetic field and by the cross product of axial components of the arc

current with the azimuthal magnetic field.¹⁶ These two effects can be integrated over the cathode face, yielding¹⁶

$$F = \frac{\mu J^2}{4\pi} \left[\ln \left(\frac{r_a}{r_c} \right) + \frac{3}{4} \right]. \quad (4.1)$$

For a flow rate on the order of 1 sccm and a current of 6 A, the exit velocity would be on the order of 0.075 m/s. Indeed, an upper bound to the exhaust speed derived from the magnetic field is

$$u \leq \frac{\mu e J}{2\pi m_i}. \quad (4.2)$$

For 6 A, this yields a limit of roughly 5 m/s. Thus, even though the data may qualitatively suggest this mechanism in spot-mode, it seems to have negligible impact.

Charge exchange collisions (involving Xe III or higher ionization states) have also been suggested as a creator of high-energy ions.¹⁷ Charge exchange collisions (Xe II—Xe I) are also the primary source of ions impinging on and eroding the accelerator grid.¹⁶ Xe I and Xe II charge exchange may also significantly influence the distributions of Xe II velocities downstream of the DCA. Cross sections for the charge exchange between an ion and an atom of the same species, *e.g.*, Xe II and Xe I, is a function of the probability of charge transfer, *P*, in a collision:¹⁸

$$\sigma(v) = 2\pi \int_0^\infty P(b, v) b db \quad (4.3)$$

where

$$P(b, v) = 2\pi \sin^2 \left[\int_{-\infty}^{+\infty} \frac{(E_a - E_s)}{2\hbar v} \right].$$

However, assuming that the internuclear separation during impact is much greater than the Bohr radius, that $P \approx 0.5$ for smaller values of b which introduce oscillations in P , and that b is constant over small ranges of v , Eqn. 4.4 simplifies to¹⁸

$$\sigma^{1/2} = -k_1 \ln(v) + k_2 \text{ [m]}. \quad (4.4)$$

For Xe I—Xe II charge exchange, $k_1 = 8.66 \cdot 10^{-9}$ and $k_2 = 1.900 \cdot 10^{-7}$. Note that the cross section increases as the ion velocity decreases. For $v = 1000 \text{ m/s}$, $\sigma = 8.100 \cdot 10^{-15} \text{ cm}^2$. The rate of charge exchange collisions will depend on the ion density measured with the Langmuir probes. Xe II—Xe III charge exchange cross sections have been shown to be roughly an order of magnitude less than the Xe I—Xe II cross sections.¹⁹

Probe Results

From Eqns. 3.13-3.14, the ion-ion mean free path of the plasma varied from 4.0 cm to roughly 40.0 cm. The sheath thickness from Eqn 3.16 was on the order of $5 \cdot 10^{-3} \text{ cm}$ and the Debye length was roughly $7 \cdot 10^{-4} \text{ cm}$. Therefore, probe data were within the thin sheath limit. The cathode was maintained at ground potential; plasma potential and the ion potentials measured were measured with respect to ground.

Floating potential, plasma potential, electron temperature, electron saturation current, and electron number density were determined using the Langmuir probe. Due to the large uncertainty in the error itself, no error bars are provided in the plots of plasma potential. The following discussion is divided into sections on the HCA without an anode and the HCA with an anode.

HCA operation without the anode

Two operating conditions were selected to represent the testing without an anode. Both were taken from an application requiring an HCA to provide an ambient plasma for space environment simulation.²⁰ As noted in Table 4.1, the same current was maintained for each and the flow rate was varied from 2.3 to 4 sccm. Both conditions are in spot mode, but the one with the lower flow rate is close to transitioning.

Langmuir probe data for HCA operation without the anode is seen in Fig. 4.8. Note that the small Langmuir probe was used for all measurements closer than 0.5 cm to the keeper. For the 2.3 sccm case, there was a significant change in electron temperature as measured by the smaller probe. As the reason for this is unclear, the error associated with that measurement is correspondingly increased. Note, however, that number density and plasma potential data for both probes were in agreement with each other. The increase in electron temperature for the 2.3 sccm case was due to the

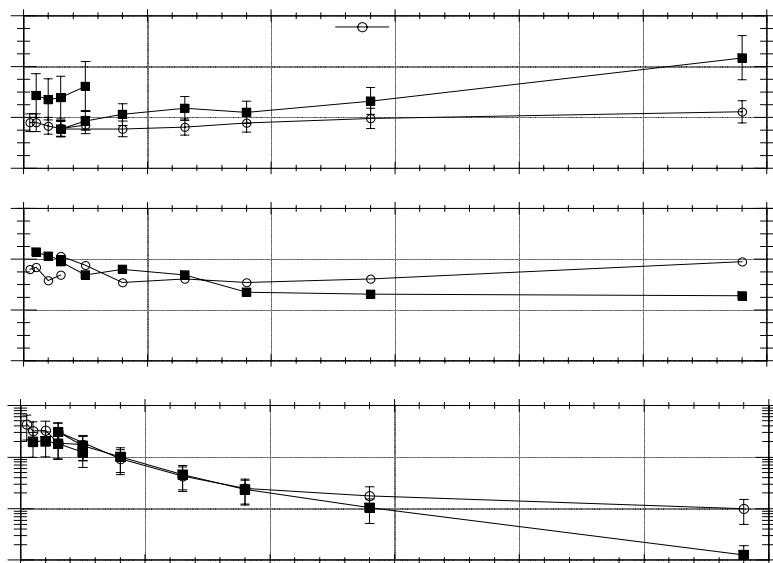


Figure 4.8 Langmuir probe data for the HCA operating without an anode. Note that all data inside of 5 mm was taken with the small probe.

close proximity of this operating condition to plume mode. Electron temperature data for the 4 sccm case appear to transition smoothly between use of the two probes.

HCA operation with the anode

Operation of the HCA with an anode was limited in power by the propellant feed system and the wiring. These limitations prevented simulation of ion thruster discharge cathode operating conditions. However, the moderate 6 A operation was instructive in predicting trends which might be observed in later studies. Because the keeper electrode is integral to the HCA, operation without a keeper (as in the 2000 hr wear test configuration) was not possible. Operation with the keeper floating resulted in clear plume mode operation.

Figure 4.9 shows that the electron temperature in plume-mode increased significantly with distance from the keeper. The slight increase in electron temperature may result from the presence of two electron populations. Primary electrons emitted from the HCA have high energies (> 15 eV) and are most likely not Maxwellian.⁹ Secondary electrons resulting from collisions are most likely Maxwellian and will be preferentially collected by the surrounding anode. The downstream electron distribution should reflect this with an increase in the mean electron temperature. The greater increase in T_e for the plume-mode case indicates that there was greater loss of moderately energetic ions from the centerline to the anode for that case.

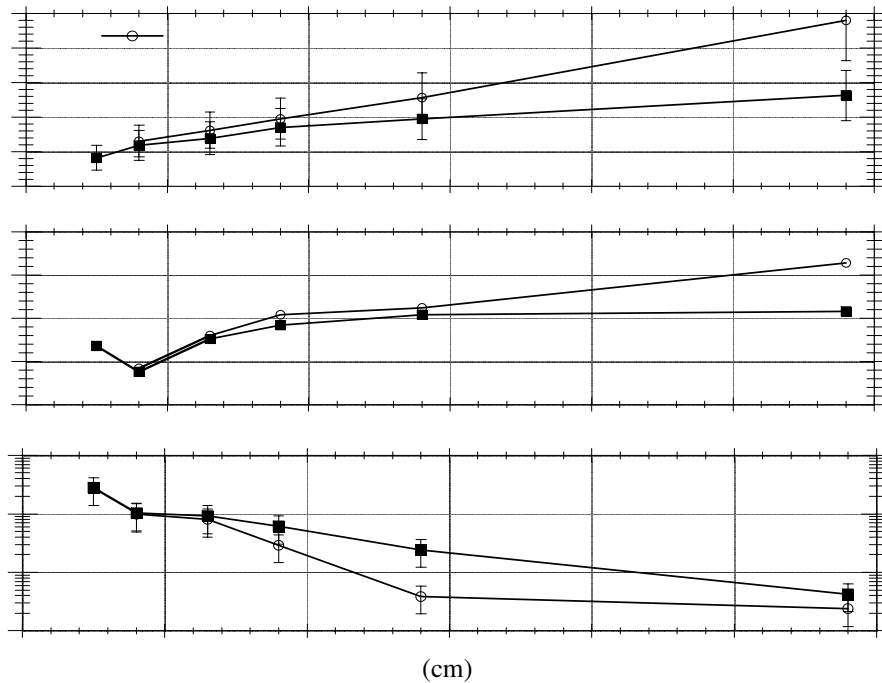


Figure 4.9 Langmuir probe data for the HCA with the anode.

The plasma potential was again roughly constant and was slightly above the discharge voltage. The increase in plasma potential several centimeters downstream of the HCA may be within the error of the measurement. However, there is a dip at about 1 cm from the keeper for both cases. It is unclear how this would exist in steady state. Because of the harsh plasma environment, it was not possible to use the small probe to obtain data closer than 0.5 cm. It was expected that the potential of the plume-mode would increase significantly. The absence of such a rise may be due to the uncertainty associated with the plasma potential measurement.

Figure 4.10 compares T_e predicted by Eqn. 3.12 to the anode-only data of HCA operation. The anode voltage of 26 V yielded a T_e of 2.5 eV which is comparable to that predicted by Eqn. 3.12 (2.9 eV). However, as discussed above, the discharge voltage is typically higher in the ion thruster discharge chamber due to ion extraction.

The rough agreement, however, does place some confidence in the use of Eqn. 3.12 to predict T_e in the discharge chamber.

Implications of the Preliminary Data

Laser-induced fluorescence was demonstrated to be a viable technique for interrogating the ion plumes of hollow cathode assemblies. The multiplex technique permitted repeatable, reliable measurement of ion speeds up to several centimeters downstream of the HCA.

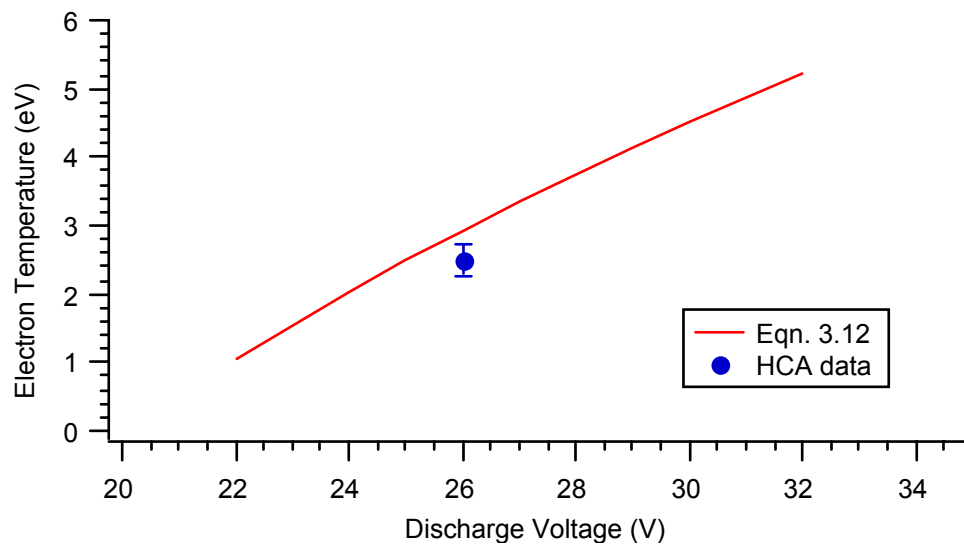


Figure 4.10 A comparison of predicted and measured electron temperature as a function of discharge voltage. The HCA anode voltage was used as V_D .

Neutral number densities estimated to be on the order of 10^{13} cm^{-3} indicate a charge-exchange mean free path of roughly 7 cm for ions moving at 500 m/s. Since there is a region of even lower velocities, especially in plume-mode, a significant

number of charge exchange collisions may be occurring within a few centimeters of the HCA exit plane. Unfortunately, Xe I velocities were not measured to verify the presence of high-speed Xe I atoms which would indicate charge exchange collisions.

The difference in Xe I and Xe II temperatures may indicate that the ion velocity distribution was not an accurate indication of the ion temperature and/or that Xe I and Xe II were not in thermodynamic equilibrium. The observed Xe I temperatures, when used in an equation of state, were consistent with the internal cathode pressures observed during operation.²

The LIF data indicated an extended region of increasing velocity downstream of the HCA and some back-flowing ions. This is especially true for plume-mode operation. No peaks in V_p were detected with the Langmuir probe. The broader and multi-peaked distributions observed in other investigations and not observed here may have resulted from doubly-charged ions, collisional broadening, or integration of off-axis ions. The observation of ions being accelerated back towards the cathode orifice indicated that this LIF technique will be of value in mapping the ion velocity profiles near the exit of the discharge cathode of an ion engine.

Notes to Chapter 4

-
- ¹ Williams, G.J., et al., “Laser-Induced Fluorescence Characterization of Ions Emitted from Hollow Cathodes,” AIAA-99-2862 (June, 1999).
- ² Domonkos, M.T., Gallimore, A.D., Williams, G.J., and Patterson, M.J., “Low-Current Hollow Cathode Evaluation,” 35th AIAA/ASME/SAE/ASEE Joint Propulsion Conference, Los Angeles, CA, June 1999.
- ³ Jack, T.M., et al., “The Effect of the Keeper Electrode on Hollow Cathode Characteristics,” AIAA-2000-3533, 36th Joint Propulsion Conference (July, 2000).
- ⁴ Friedly, V.J. and P.J. Wilbur, “High-Current Hollow Cathode Phenomena,” *Journal of Propulsion and Power*, **8** (3) 1992, 635–643.
- ⁵ Siegfried, D.E. and P.J. Wilbur, “An Investigation of Mercury Hollow Cathode Phenomena,” AIAA-78-705, 13th International Electric Propulsion Conference (April, 1978).
- ⁶ Kamayama, I., and P.J. Wilbur, “Characteristics of Ions Emitted from High-Current Hollow Cathodes,” IEPC-93-023, 23rd International Electric Propulsion Conference (August, 1993).
- ⁷ Kamayama, I., and P.J. Wilbur, “Effects of External Flow near High-Current Hollow Cathodes on Ion-energy Distributions,” IEPC-97-173, 25th International Electric Propulsion Conference (August, 1997).
- ⁸ Williams, G.J., et al., “Near-field Investigation of Ions Emitted from a Hollow Cathode Assembly Operating at Low Power,” AIAA-98-3658, 34th Joint Propulsion Conference (July, 1998).
- ⁹ Domonkos, M.T., et al., “Low Current Hollow Cathode Evaluation,” AIAA-99-2575, 35th Joint Propulsion Conference (June, 1999).
- ¹⁰ Salhi, A., *Theoretical and Experimental Studies of Orificed Hollow Cathodes*, Ph.D. Dissertation, Colorado State University, 1993.
- ¹¹ Kameyama, I., and P.J. Wilbur, “Characteristics of Ions Emitted from High-Current Hollow Cathodes,” IEPC-93-023, 23rd International Electric Propulsion Conference, (August, 1993).
- ¹² Kameyama, I., and P.J. Wilbur, “Effects of External Flow Near High-Current Hollow Cathodes on Ion-Energy Distributions,” IEPC-97-173, 25th International Electric Propulsion Conference, (August, 1997).

-
- ¹³ Friedly, V.J., and P.J. Wilbur, "High Current Hollow Cathode Phenomena," *Journal of Propulsion and Power*, Vol. 8, No. 3, 1992, 635–643.
- ¹⁴ Kameyama, I., and P.J. Wilbur, "Potential-Hill Model of High-Energy Ion Production Near High-Current Hollow Cathodes," ISTS-98-Aa-2-17, 21st International Symposium on Space Technology and Science, (May, 1998).
- ¹⁵ Brophy, J.R., and C.E. Garner, "Tests of High Current Hollow Cathodes for ion Engines," AIAA-88-2913, 24th Joint propulsion Conference, (July, 1988).
- ¹⁶ Jahn, R G., *Physics of Electric Propulsion*, McGraw Hill, New York, 1968, pp. 240–248.
- ¹⁷ Crofton, M.W., "The Feasibility of Hollow Cathode Ion Thrusters: A Preliminary Characterization," AIAA-2000-5354, 36th Joint Propulsion Conference (July, 2000).
- ¹⁸ Rapp, D., and W.E. Francis, "Charge Exchange Between Gaseous Ions and Atoms," *The Journal of Chemical Physics*, **37** (11) December, 1962, 2631–2645.
- ¹⁹ Kusakabe, T., et al., "Charge Transfer of Multiply Charged Slow Argon, Krypton, and Xenon Ions on Atomic and Molecular Targets. Single-Charge Transfer Cross Sections," *journal of Physics, B*, **19** 1986, 2165–2174.
- ²⁰ Bilen, S.G., et al., "The Far-Field Plasma Environment of a Hollow Cathode Assembly," AIAA-99-2861, 35th Joint Propulsion Conference (June, 1999).

CHAPTER 5

DISCHARGE CATHODE EROSION MEASUREMENTS

Previous investigations have demonstrated LIF as a tool for measuring erosion of ion thruster components.^{1,2} It presents an attractive alternative to profilometry or destructive analysis because it can, in principle, provide a real-time measurement of a species' concentration—which could be correlated to operating condition, provide an in situ measurement, and provide detailed spatial resolution. The concentration can be related to erosion rates of specific surfaces, especially given LIF's high spatial resolution.

Given the capability to perform LIF and a thruster with optical access, a real-time, absolute erosion-rate measurement capability would require a real-time measurement of an eroded species, a model which converts the signal to a measure of the density of eroded species, a conversion from density to erosion-rate, and an in-situ calibration of this rate. The former two are discussed in depth below following a brief overview of sputtering theory. As a first approximation, the relative erosion rates are calculated given the erosion rates measured in the 2000 hr and 8200 hr wear tests. The latter two requirements of a true absolute erosion-rate measurement capability are left to future investigations.

Sputtering Theory

Sputtering of discharge chamber materials by low-energy ions (<100 eV) has been the subject of much theoretical but little experimental investigation.³ Two investigations identified sputtering thresholds at low energies.^{4,5} The sputtering yield and threshold energy are proportional to what has been referred to as the binding energy. Typically, the binding energy has been assumed to equal the sublimation energy.⁶ An empirical correlation between these values and the sublimation energy of the target material was developed to predict the threshold energy for low energy sputtering by heavy ions.⁷ For ions striking the target at normal incidence (0 deg.), this correlation yielded the following curve fit for the threshold energy as a function of sublimation energy, E_s , and the ration of target atom to incident ion masses (m_2/m_1):

$$E_{TH}(\theta = 0) = E_s \left(4.4 - 1.3 \cdot \log \left(\frac{m_2}{m_1} \right) \right). \quad (5.1)$$

The angular dependence of the sputtering yield and threshold energy has been the subject of several investigations.^{6,8,9,10,11} However, because this investigation is primarily concerned with erosion below the nominal Mo and W threshold values of 30 to 35 eV, incorporation of the angular dependence into the expression for the threshold energy was important. Angular dependence of the yield without modification of the threshold value would produce a variation in the sputtering yield but not a reduction in the threshold at which this erosion occurs and that would, most likely, preclude consideration of the ion energies present in the discharge chamber.

The angular dependence of the threshold energy is driven by the threshold for the sputtering processes such as “billiard ball” mechanisms and by the threshold corresponding to surface channeling.³ For small to moderate angles ($\theta < 60$ deg from

normal incidence) the sputtering process dominates and experimental evidence suggests the following angular dependence:⁸

$$E_{TH}(\theta) = E_s \left(4.4 - 1.3 \cdot \log \left(\frac{m_2}{m_1} \right) \right) \cos^2(\theta) \quad (5.2)$$

For large angles, the surface channeling becomes important and for very large angles, it dominates.⁸ The threshold energy for large angles reflects this:

$$E_{TH}(\theta) = \left[0.3 \frac{\frac{m_1}{m_2}}{\frac{m_1}{m_2} + 1} \frac{m_1 + m_2}{m_2} Z_1 Z_2 e^2 \frac{a^2}{n_2} \right] \cos^{-2}(\theta) \quad (5.3)$$

where the Thomas-Fermi screening radius is given by,

$$a = 0.4685 \left(Z_1^{2/3} + Z_2^{2/3} \right)^{-1/2},$$

and Z_1 and Z_2 refer to the incident and target atomic numbers, respectively.⁸

Given the sputtering threshold energies, Bodansky's formulation for the sputtering yield (atoms per incident ion) was selected because it is valid for both light and heavy ions and because it has shown good agreement with experimental data where available.³ Using this relation, the sputter yield, $y(E, \theta)$, can be expressed as a function of ion energy, E , and angle from normal incidence, θ :¹²

$$y(E, \theta) = \frac{0.042 \zeta S_n(E)}{E_s} \left(\frac{R_p}{R} \right) \left[1 - \left(\frac{E_{TH}(\theta)}{E} \right)^{2/3} \right] \left[1 - \left(\frac{E_{TH}(\theta)}{E} \right) \right]^2 \quad (5.4)$$

where ζ is a normalizing constant to correlate the measured yields and threshold energies for normal incidence.

Figure 5.1 shows Mo and W sputtering thresholds as a function of ion angle of incidence. Note that both thresholds dip and then increase with angle. The minimum thresholds are roughly 20 eV for both species. The minimum threshold for Mo occurs

for ions impacting at 45 degrees and for W for ions at roughly 50 degrees. Sputter yields as a function of ion angle and energy are given in Figs. 5.2a and 5.2b for Mo and W, respectively. Note that the yields for ions impacting at 50 to 55 degrees are roughly twice that for ions impacting at normal incidence (0 degrees).

The flux of atoms sputtered from the surface of the DCA can be calculated from the erosion rates given in Chapter 1 for the 2000 hr wear-test. These are $2.55 \cdot 10^{18} \text{ m}^{-2} \text{ s}^{-1}$ and $4.98 \cdot 10^{18} \text{ m}^{-2} \text{ s}^{-1}$ for W and Mo, respectively. The flux of mono-energetic incident ions required to generate these fluxes can be calculated as a function of energy and

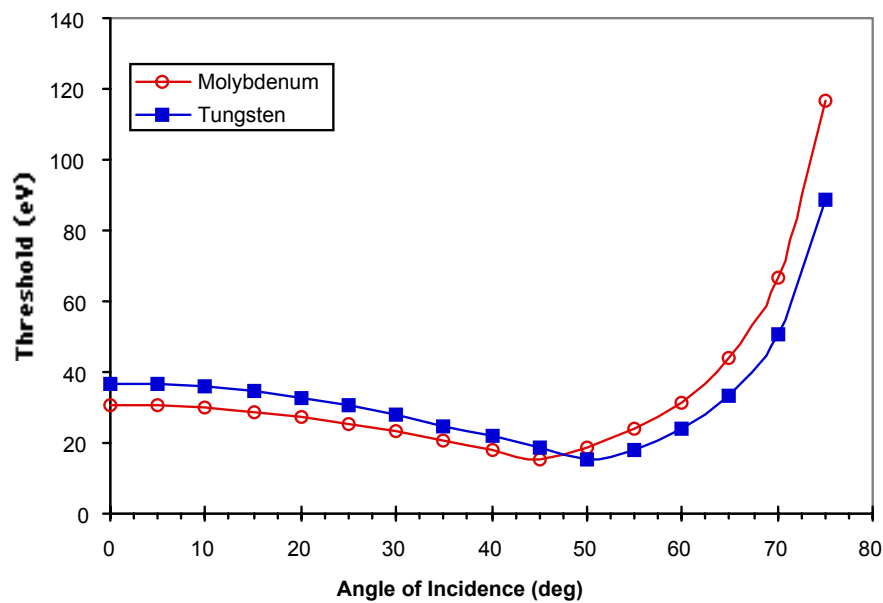


Figure 5.1 Sputter thresholds as a function of angle of incidence.

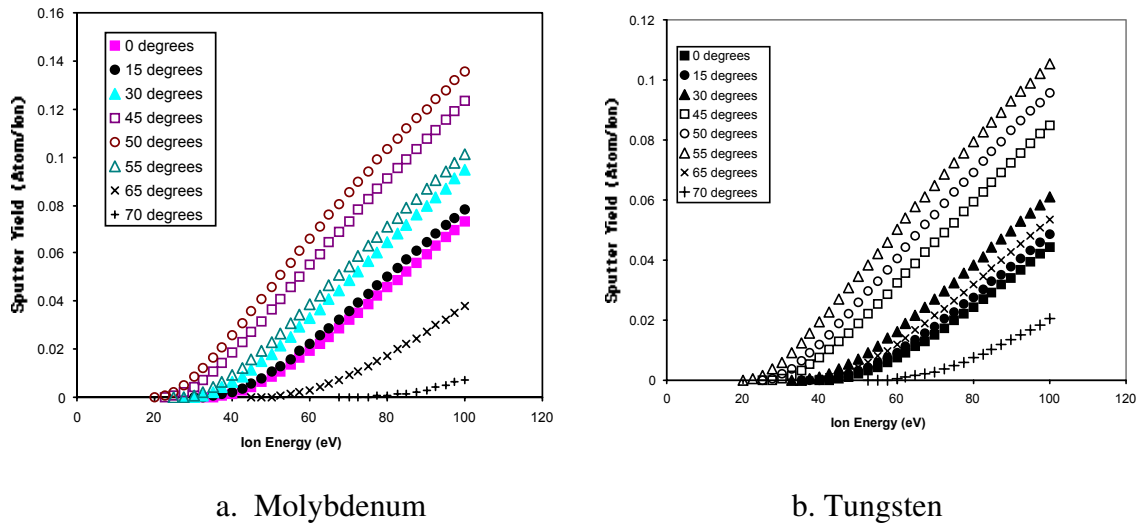


Figure 5.2 Sputter yields as a function of ion energy and angle of incidence.

angle of incidence using Eqn. 5.4. The densities associated with the ion fluxes is then calculated by dividing the ion flux by the velocities corresponding to the energies of the ions (pre-sheath). The sheath energy (approximated as 20 V as discussed below) is added to the ion energy to calculate the sputter yield. These number densities of incident Xe II ions required to generate the measured fluxes of eroded species are given in Fig. 5.3a and 5.3b as a function of incident energy and angle. Note, the effects of Th impregnation of the W have been neglected due to the uncertainty in the value of the resulting sublimation energy, E_s . The curves' upper limits correspond to the threshold energies. Note the significant decrease in density required at lower energies for angles of incidence near 50 degrees. Note that a 50 degrees angle of incidence would indicate a source of high-energy ions roughly 0.25 cm downstream of the orifice.

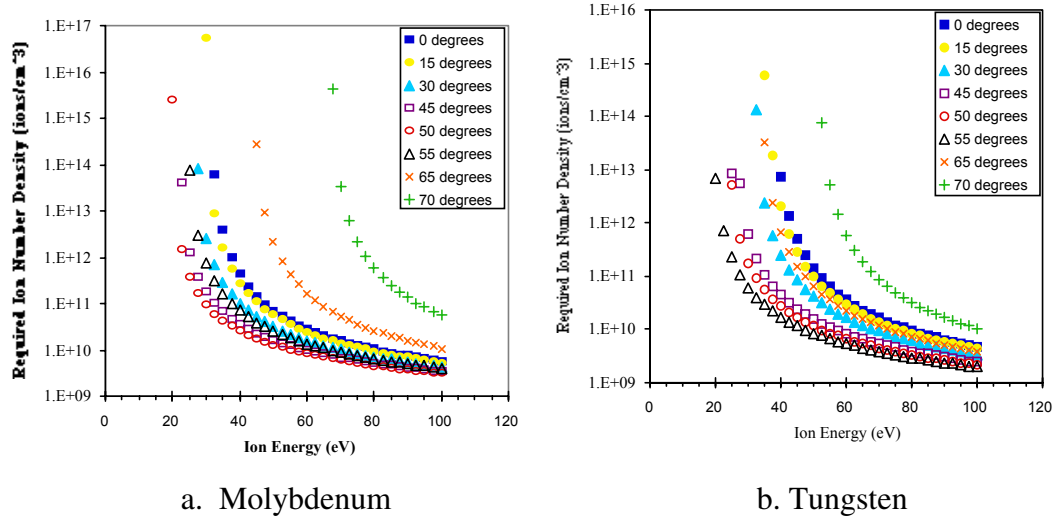


Figure 5.3 Xe II densities required to produce the erosion observed in the 2000 hr wear test.

Laser-Induced Fluorescence

A typical W LIF signal is shown in Fig. 5.4. The data were taken 0.3 cm off centerline, 0.05 cm downstream of the un-keepered DCA operating at 12 A, 27 V. To facilitate optimization of the W LIF signal, a W target was bombarded with ions from the HCA. The target provided a clean W LIF spectrum and was located on centerline behind the FMT in the LVTF. The W reference data were taken with the W target biased 100 V below cathode potential. The first order fit is shown with open markers. The fit indicated that the reference data had a temperature of 1000 K. Table 3.2 gives the parameters for the W fit. The spatial resolution of the LIF data is roughly 1 mm³.

A typical Mo LIF signal is shown in Fig. 5.5. The Mo reference data were taken in the same Hamamatsu cell used to generate the Xe I and Xe II reference

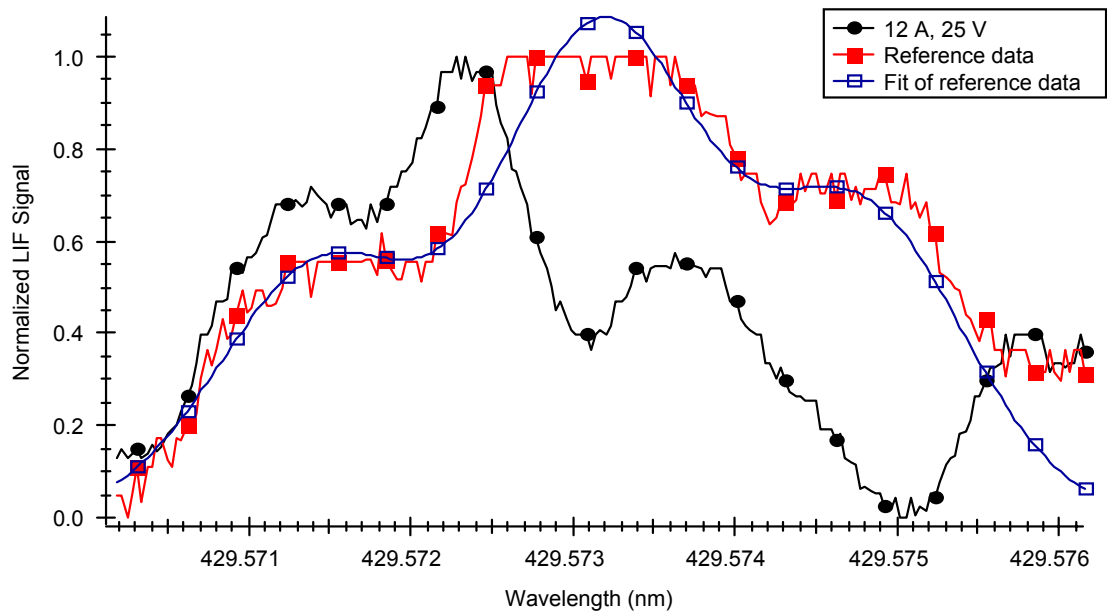


Figure 5.4 Typical W LIF data. Note that the slight offset of the data taken downstream of the DCA indicates an axial velocity on the order of 1000 m/s.

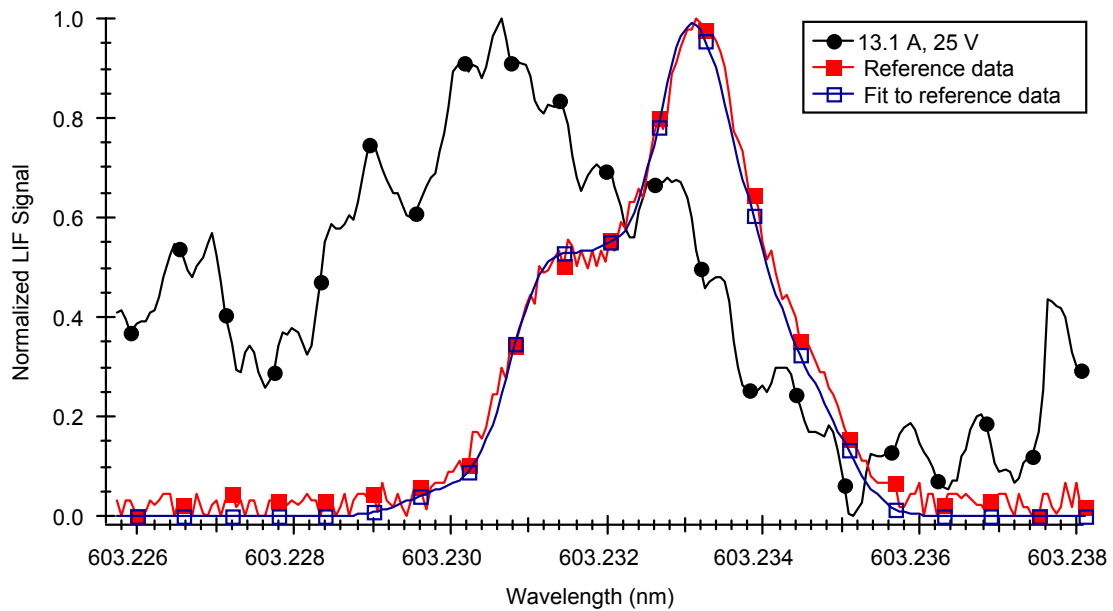


Figure 5.5 Typical Mo LIF data.

signals. The Mo in the reference cell discharge was generated both by sputtering from impinging ions and by thermal release from the surface to maintain its vapor pressure. The temperature indicated by the fit of the reference cell data, 800 K, is within 50 K of the Xe I and Xe II data taken at the same cell voltage and current. The data near the DCA were collected with a single “vertical” beam. The fluorescence signal was processed by several lock-in amplifiers set to slightly different gains and time constants. The signals from the lock-ins were later averaged to minimize the noise in the signal.

Un-keepered Data

Figure 5.6 shows Mo and W LIF signals as a function of radial position as indicated by a picture of the exit plane of the un-keepered DCA. Note that the signals peak at roughly the same radial position (0.3 to 0.4 cm) and indicate erosion peaks

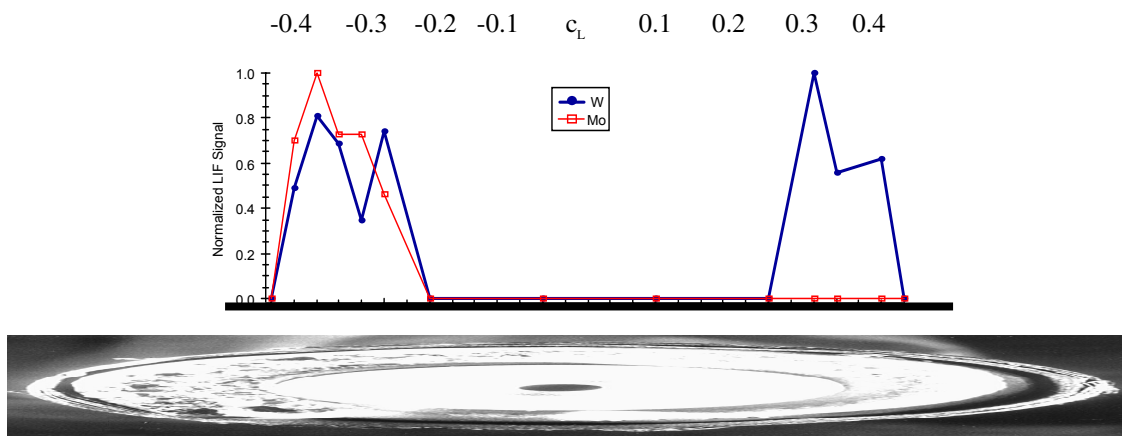


Figure 5.6 Radial distribution of Mo and W LIF signals across the cathode exit plane which have been self-normalized. Note that no Mo data were taken right of centerline. Data shown are for 12 A, 27 V.

near the transition from the cathode orifice plate (W) to the cathode tube (Mo). The resolution of the LIF technique (roughly 0.05 cm) did not allow a more detailed mapping. Mo data were only taken over half of the diameter.

These data are in excellent agreement with the erosion observed during the 2000 hr wear test. Recall from Chapter 1 that the orifice plate experienced very little erosion except near its outer edge. Thus, little W should have been detected over the inner half of the orifice plate. That W LIF signals were detected over a broader length than is suggested by erosion measurements is probably because of diffuse sputtering of the W atoms. That is, while the W atoms may emanate from a somewhat narrow band along the orifice plate, their trajectories are such that they are detected over a larger radial zone downstream of the surface. Since the Mo LIF signal has roughly the same breadth as the W signal, even though the Mo surface is confined to the downstream edge of the cathode tube (roughly 0.025 cm thick), the W erosion may be coming from a region of roughly the same thickness which would be in agreement with the observed erosion. Even greater spatial resolution may not yield discrimination between erosion from various portions of the cathode tube (*e.g.*, from its downstream or exposed outer surfaces) because of the diffuse nature of sputtering. Spatial resolution on the order of 0.2 cm should be possible, however.

Subsequent Mo data were taken at the 0.3 cm radial location (0.05 cm downstream) because the Mo surface subject to impinging ions (the downstream edge of the Mo tube at the outer edge of the orifice plate) was limited to this region. W data were taken at roughly the same point for comparison, and because this was the location of the greatest W erosion observed in the 2000 hr test.

Figure 5.7 shows the Mo LIF signal strength as a function of discharge current. Note that there is a noticeable increase in signal with current and a non-negligible signal at $J_d=6.0$ A. Data taken at $V_d = 27$ V show that the Mo LIF signal also increases with discharge voltage. Also shown in the figure is the 27 V data corrected for discharge voltage variations using the coronal model. This tended to collapse the data to a monotonically increasing function of J_d .

The Mo temperature was roughly constant at 2000 K after correction for saturation effects. Xenon neutral temperatures varied between 2000 and 2500 K when corrected for saturation effects. Typical Xe I data ($J_d = 13.1$ A) are given in Fig. 5.8. The correlation of these two temperatures was surprising since it might suggest collisions between Mo and Xe I neutral atoms. However, neutral-neutral mean free paths on the order of 50 cm indicate that these collisions are not taking place.

Figure 5.9 shows W LIF data as a function of discharge current and discharge voltage. The signal is roughly constant with discharge current below 12 A, above

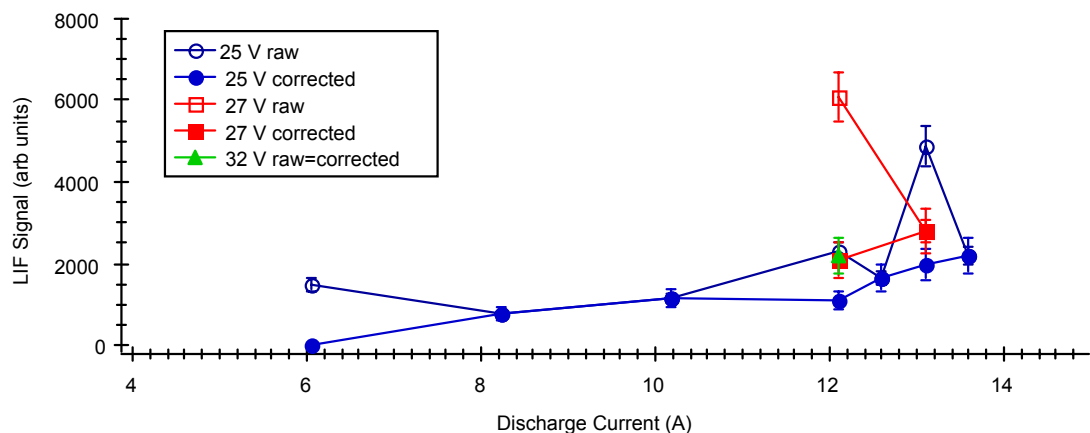


Figure 5.7 LIF signal strength as a function of discharge current for 25, 27 and 32 V operation. Solid data markers indicate signal correction for variations in V_d .

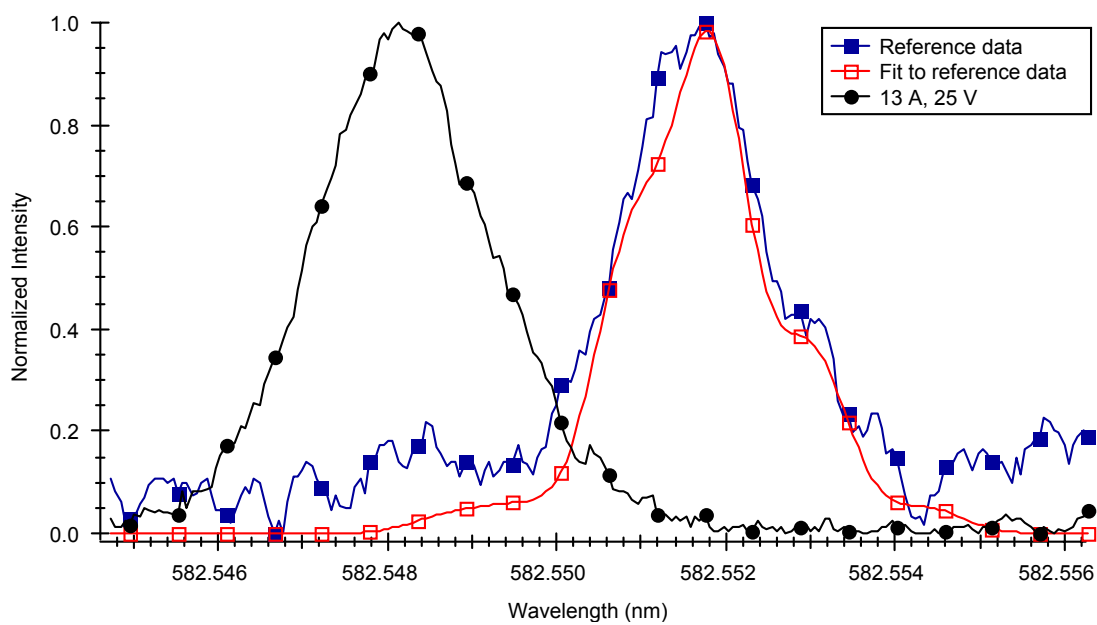


Figure 5.8 Typical Xe I LIF data. The offset is within the uncertainty of the velocity measurement.

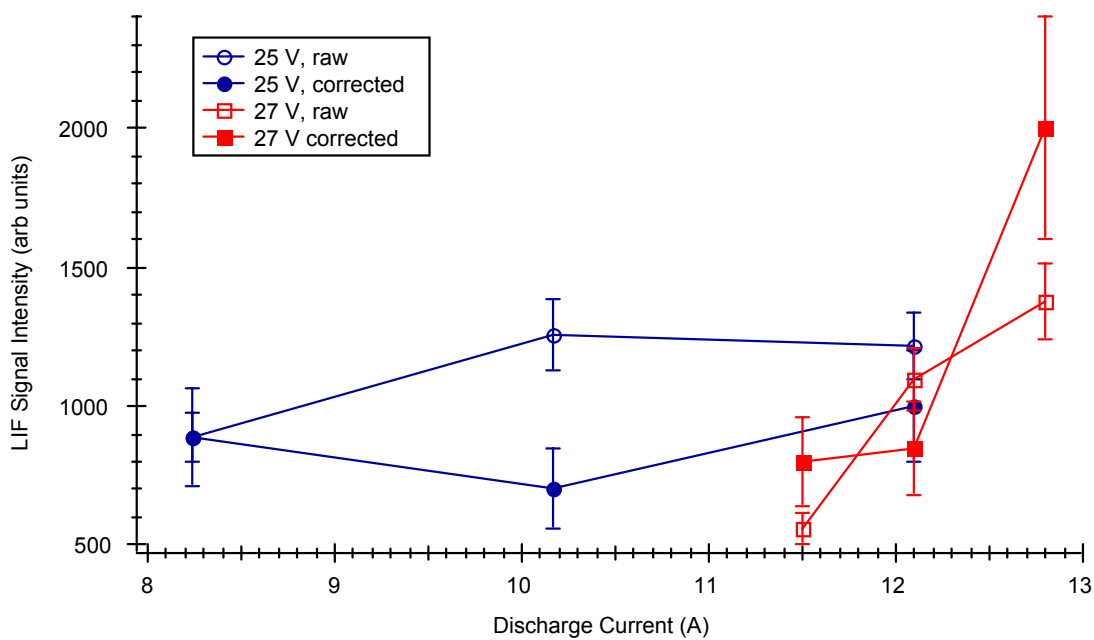


Figure 5.9 W LIF signal as a function of discharge current for $V_d = 25$ and 27 V.

which it increases significantly. The W temperatures varied between 2000 and 3000. However, the data were very noisy and introduced an uncertainty of roughly 30 percent.

Figure 5.10 shows Mo and W orifice plate erosion rates as a function of operating condition. The 12 A, 27 V erosion rate was set to the value measured in the 2000 hr wear-test and the other data were scaled accordingly in order to show the dependence of the erosion rate on the operating condition. Note that the Mo data show a greater dependence on operating condition. The 12 A, 27 V condition had a significantly higher signal and temperature than other conditions. The signal corrected for saturation and variations in state populations was consistent with those at other operating conditions.

Keeped Data

Figure 5.11 shows the variation in Mo LIF signal across the face of the DCA keeper. The picture of the keeper provides a reference for radial position. The data

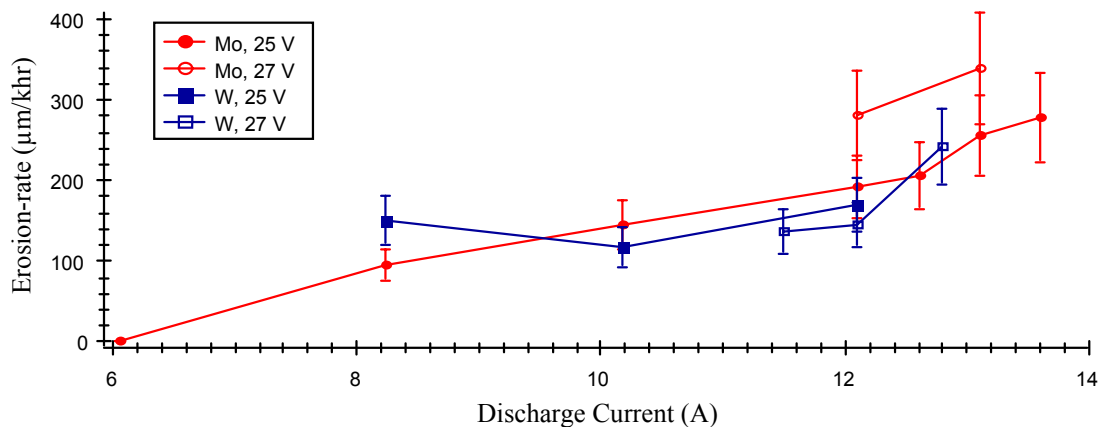


Figure 5.10 Erosion-rates predicted for un-keeped operation.

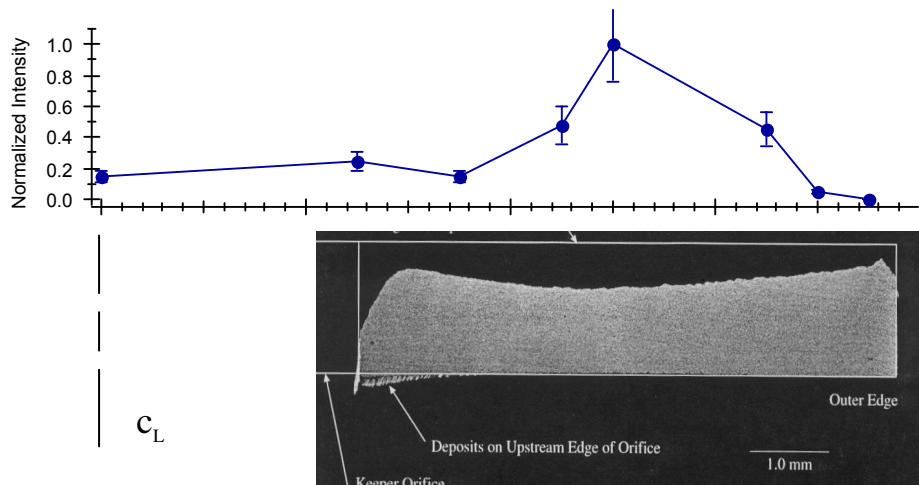


Figure 5.11 Mo LIF across the face of the keeper electrode for 13 A, 25 V. Note that the LIF signal corresponds to the erosion pattern.

were taken 0.05 cm downstream of the keeper orifice plate and the maximum signal occurred at roughly 0.5 cm off centerline. Limits in optical access prevented measurement beyond 1 cm. Subsequent Mo data were taken at the 0.5 cm radial location. No W data were collected for keptered operation.

Figure 5.12 shows Mo LIF signal and T_e -corrected data as a function of discharge current for $V_d = 25$ V and 27 V. A strong dependence on current is evident, and the signal is non-negligible at $J_d = 8.2$ A. Unlike in the un-keptered data, T_e corrections appear to remove the dependence on discharge voltage over this small range. Pure Gaussian fitting of the keptered Mo signals yielded temperatures between 8000 and 11000 K. Corrected for saturation, the temperatures were between 2000 and 3000 K, a reduction of roughly 75 percent. Neutral xenon data collected for $J_d = 8.2$ and 13.1 A (25 V) yielded temperatures varying between 2500 and 3500 K. For reference, the temperatures determined from fitting the spectra of various species are

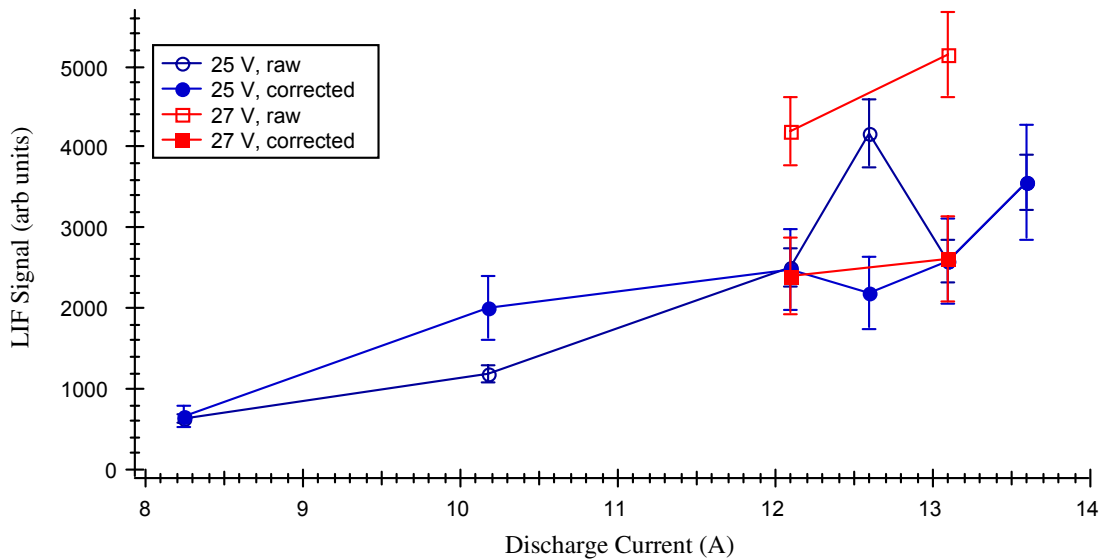


Figure 5.12 Mo LIF signal strength as a function of discharge current for $V_d = 25$ V and 27 V.

given in Table 5.1 for various operating conditions. Note the relative consistency of the eroded species temperatures and the large fluctuations in the Xe II temperatures. However, as noted in Chapter 4, the absence of LTE places into question the meaningful relation of these temperatures.

Table 5.1: A comparison of the temperatures of various species as a function of operating condition taken 0.3 cm off centerline, 0.05 cm downstream.

	Xe I	Xe II	Mo	W
Un-kept				
8 A, 27 V	3500 K	-	2000 K	2800 K
12 A, 27 V	-	4600 K	2000 K	3300 K
13 A, 25 V	2750 K	20,900 K	3000 K	2000 K
Kept				
8 A, 25 V	5000 K	11,600 K	-	N/A
12 A, 27 V	-	9900 K	3000 K	N/A
13 A, 25 V	3500 K	7200 K	3000 K	N/A

Figure 5.13 shows the keeper erosion-rate as a function of operating condition assuming the 13 A, 25 V case produces a rate similar to that measured in the 8000 hr life-test. Note that, as in the un-kept Mo data, there is a noticeable dependence on J_D and that the curve is fairly smooth.

Summary

Erosion was observed at all operating conditions in both kept and un-kept configurations. The erosion rate appeared to be linear with discharge current—there was no operating point which abruptly increased or decreased the erosion. As observed in the 8200 hr wear test, the erosion rate of the keeper was roughly a factor of four less than the orifice plate erosion as illustrated in Fig. 5.14.

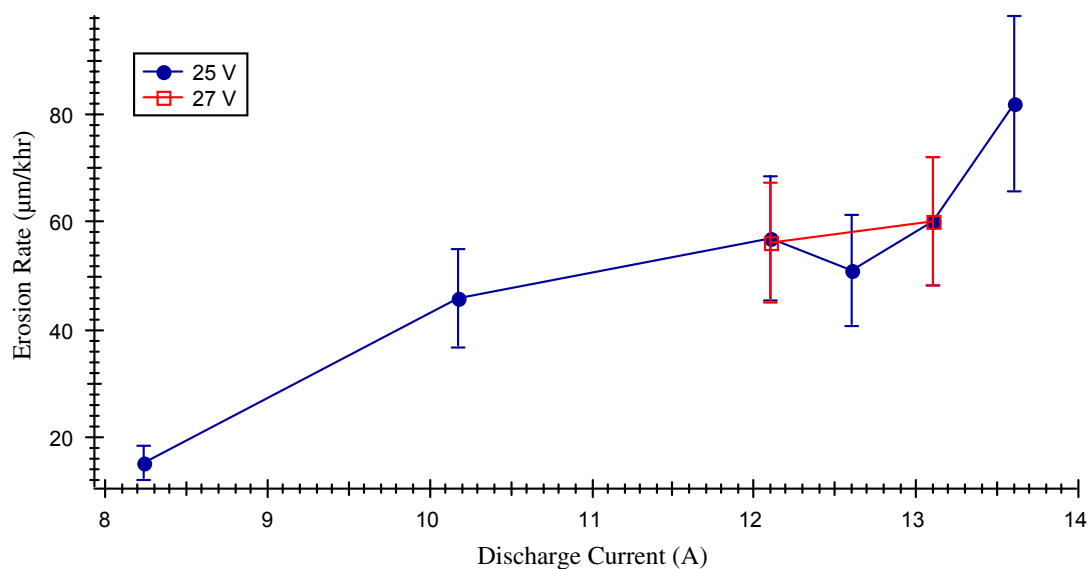


Figure 5.13 DCA keeper erosion rate estimates as a function of discharge current.

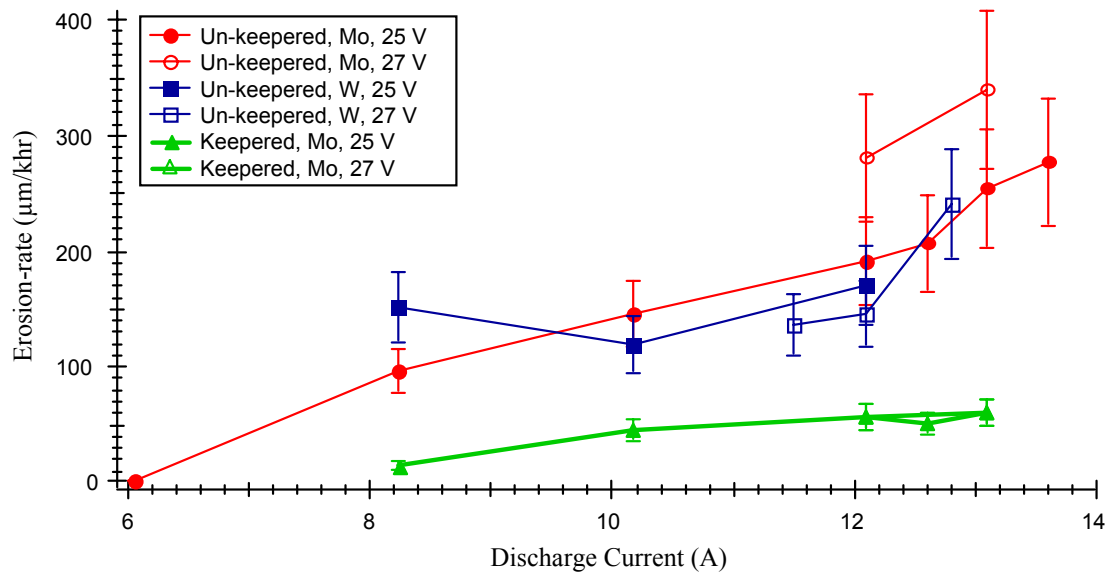


Figure 5.14 A comparison of un-kept and kept erosion rates.

The throttling of NSTAR and post-NSTAR 30 cm ion thrusters is nominally done at constant discharge voltage. Therefore, the trends evident in the 25 V data are of particular value despite the uncertainty in absolute values. Note that both kept and un-kept data show a gradual rise in predicted erosion rate with discharge current (Fig. 5.14). Modest changes in J_d below 12 A will moderately reduce the erosion. However, increasing J_d above 12 A may significantly increase it unless the discharge voltage is decreased.

The erosion rates were smaller for kept operation independent of cathode flow rate, current or voltage as compared to un-kept operation. This is consistent with the decreased erosion observed in the 1000 hr wear-test and 8200 life-test and suggests that the keeper, itself, modified the erosion process. The data suggest that the

counter-acting contributions of a decrease in discharge voltage and an increase in discharge current probably resulted in little modification of the erosion process and would not, by themselves, result in a significantly different erosion rate.

Notes to Chapter 5

-
- ¹ Gaeta, C.J., et al., “Erosion Rate Diagnostics in Ion Thrusters Using Laser Induced Fluorescence,” *Journal of Propulsion and Power*, **9** (3) 1993, 369–376.
- ² Beattie, J.R., and J.N. Matossian, “High-Power Ion Thruster technology,” NASA Technical Report CR–195477, 1992.
- ³ Duchemin, O.B., et al., “A Review of Low-Energy Sputtering Theory and Experiments,” IEPC–97–068, 25th International Electric Propulsion Conference, (October, 1999).
- ⁴ Stuart, R.V., and G.K. Wehner, “Sputtering at Very Low Energy Light ion Sputtering,” *Journal of Applied Physics*, **33** (7) 1962, 2345–2352.
- ⁵ Askerov, S.G., and L.A. Sena, “Cathode Sputtering of Metals by Slow Mercury Ions,” *Soviet Physics—Solid State*, **11** (6) 1969, 1288–1293.
- ⁶ Sigmund, P., “Theory of Sputtering Yields of Amorphous and Polycrystalline Targets,” *Physical Review*, **184** (2) 1969, 383–416.
- ⁷ Manteniks, M.A., “Sputtering Threshold Energies of Heavy Ions,” IEPC–97–187, 25th International Electric Propulsion Conference, 1997.
- ⁸ Yamamura, Y., et al., “Angular Dependence of Sputtering yields of Monatomic Solids,” Report IPPJ–AM–26, Institute of Plasma Physics, Nagoya University, Japan, 1983.
- ⁹ Lindhard, J., et al., *Mat. Fys. Medd. Dan. Vid. Selsk.*, **33** (14) 1963.
- ¹⁰ Matsunami, N., et al., “A Semi-empirical Formula for the Energy Dependence of the Sputtering Yield,” *Rad. Eff. Lett.*, **55** (15) 1980.
- ¹¹ Eckstein, W., et al., “Threshold Energy for Sputtering and Its Dependence on Angle of Incidence,” *Nucl. Instr. And Meth. In Phys. Res.*, **B83** 1993, 95–109.
- ¹² Bohdansky, J., “A Universal Relation for the Sputtering Yield of Monatomic Solids at Normal Ion Incidence,” *Nucl. Instr. And Meth. In Phys. Res.*, **B2** (587) 1984.

CHAPTER 6

XENON II VELOCIMETRY DOWNSTREAM OF THE DISCHARGE CATHODE IN THE ION THRUSTER

Xenon ion velocimetry was performed to identify the energy and the source of ions impacting the DCA surface and resulting in the observed erosion. Measurements were performed for both keepered and un-keepered configurations. Because a sophisticated model exists for reduction of LIF data for the 605—529 nm Xe II LIF transition,¹ that transition and model were employed in this analysis. The velocity and energy profiles are measured and do not entail assuming a Maxwellian distribution as did the HCA data. A brief discussion of the Xe II temperatures measured during the velocimetry is also presented.

Laser-Induced Fluorescence

Four laser beams were used in a multiplex configuration to simultaneously measure the three components of ion velocity: two beams were used to measure the axial velocity in order to maximize the accuracy of these measurements. Figure 6.1 shows the delivery of the four beams to the FMT. The angles between the off-axis beams and the vertical are given in Table 6.1. The angles were measured by taking

Table 6.1: LIF interrogation angles.

	α (deg)	β (deg)	γ (deg)
Un-keepereed data	10.51 ± 0.40	7.697 ± 0.42	4.480 ± 0.42
Keepereed data	10.57 ± 0.41	7.737 ± 0.47	4.232 ± 0.23

several measurements of the spacing between the beams at the delivery lens in the LVTF.

The second axial ion velocity was calculated from the second axial beam via Eqn. 3.2 by substituting of v_{o2} for v_o and γ for α . Similarly, the radial velocity can be calculated using the vertical velocity and the velocity indicated by the beam containing both radial and vertical components, the lateral beam. Substitution of v_L for v_o , T_L for T_o and β for α in Eqns. 3.2 and 3.3 yield the radial velocity and temperature, respectively.

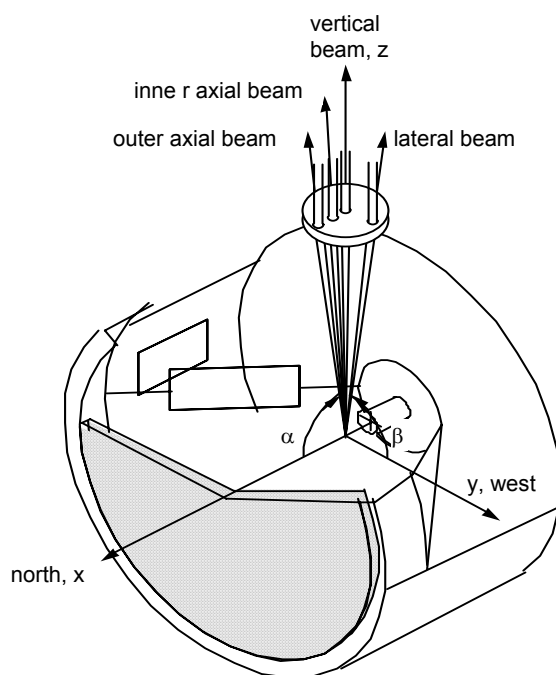


Figure 6.1 Schematic of laser beam delivery. Note the location of the beams on the lens.

A typical set of Xe II data is given in Fig. 6.2. These data were taken on centerline, 0.5 cm downstream of the un-kept DCA at 12 A, 27 V. Note the close proximity of the four curves which illustrate the sensitivity to the size and resolution of the beam angles. The de-convolution algorithm was used to calculate the velocities and the temperatures were estimated by fitting the resulting velocity profiles with Gaussian distributions (Eqn. 3.5).¹ Uncertainties in the velocity measurements are roughly 20 percent.

Un-kept Operation

Figure 6.3 compares mean axial centerline velocities for various un-kept DCA/FMT operating conditions. While the magnitudes of the velocities depended on the specific operating condition, the data do indicate several trends. There was a region of low-velocity/back-flowing ions just downstream of the orifice. The

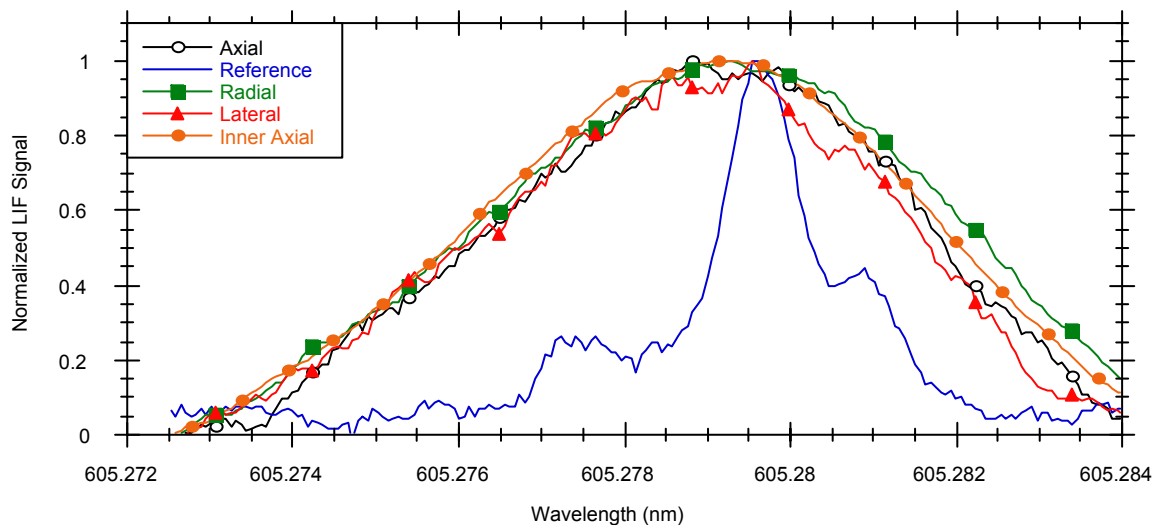


Figure 6.2 Typical Xe II LIF data. Data shown were taken on centerline, 0.5 cm downstream of the un-kept DCA operating at 12 A, 27 V.

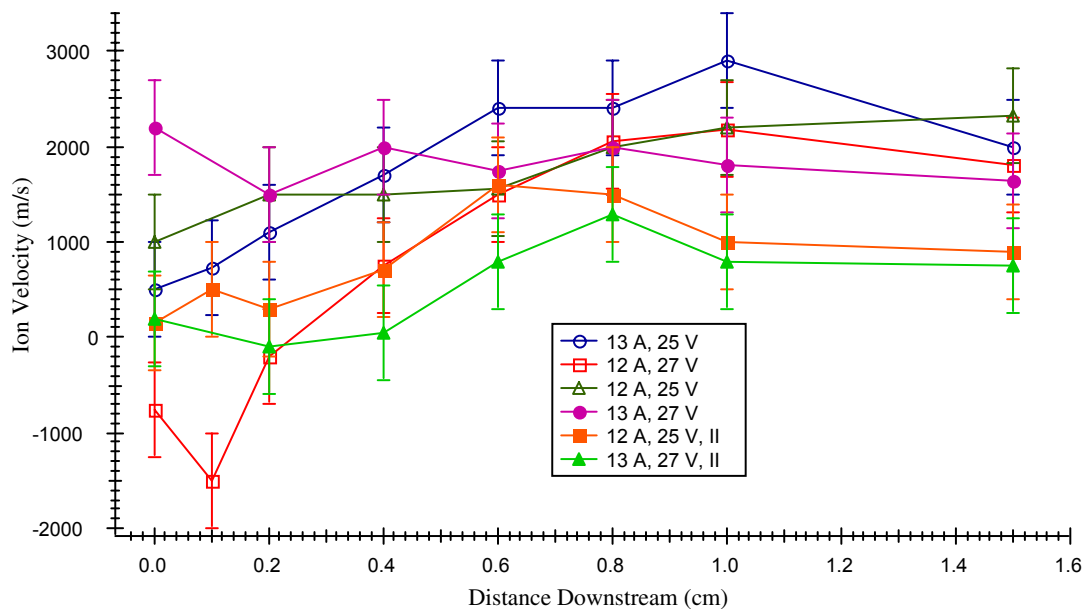


Figure 6.3 Centerline axial Xe II velocities downstream of the un-kept DCA. Note, $1 \text{ eV} = 1200 \text{ m/s}$. Recall that the “II” after the operating condition indicates a change in main flow rate.

velocities then increased to a peak roughly 1 cm downstream and then remain at that level. Higher J_d led to higher velocities downstream. Figure 6.4 shows the variation in axial velocity with radial position for the 12 A, 27 V case. Note that the same trends are present. However, the middle position, 0.2 cm off centerline, had the smallest degree of back-flowing ions. This would suggest that less erosion should be present over the middle of the orifice plate which was what was observed.

Figure 6.5 gives radial velocities along the centerline of the un-kept DCA’s plume for the 12 A, 27 V and 13 A, 25 V operating conditions. Note the large peak in the 13 A data near 0.2 cm. Higher velocities would indicate regions of larger potential gradients. Potentials would tend to be higher where the ion population is the greatest as discussed above. The millimeter resolution of the LIF may not be able to

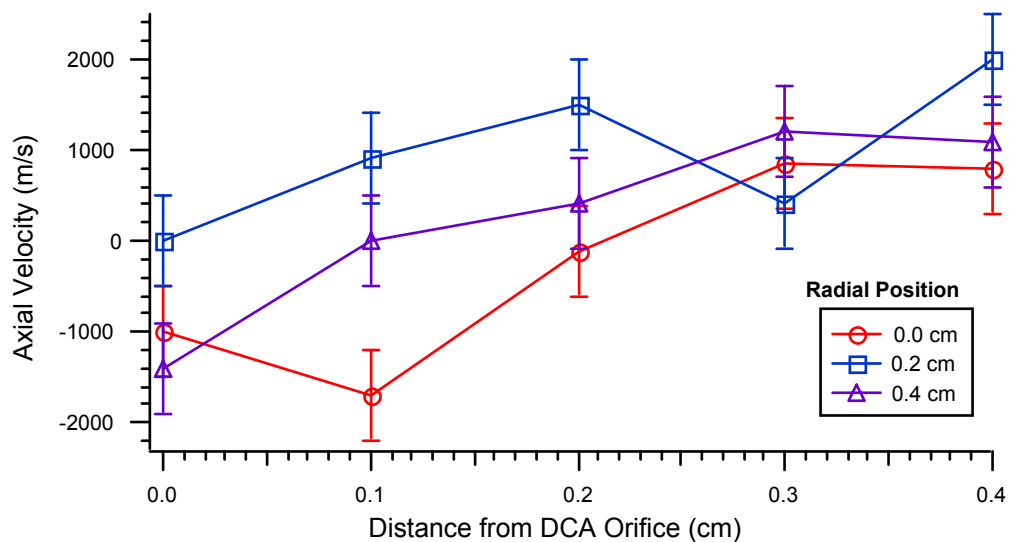


Figure 6.4 Axial velocities off-centerline for the 12 A, 27 V condition.

resolve the radial gradients in the plasma potential (via velocimetry). A slight offset from the centerline (resulting from either initial misalignment, slight off-axis travel, or variation in the laser spot's location) might result in measurement of the ion's velocity outside of the region of primary ionization after it had been accelerated through the

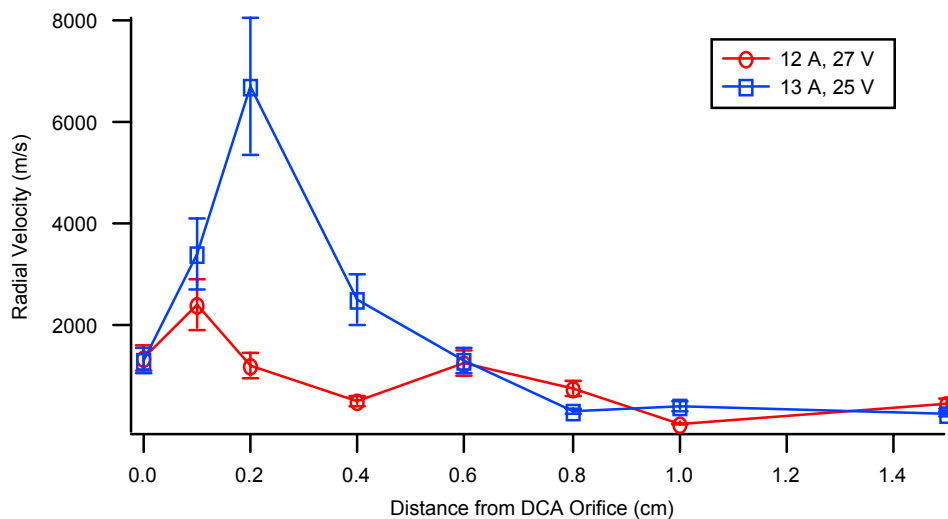


Figure 6.5 A comparison of radial velocities along the centerline for the 12 A, 27 V and 13 A, 25 V un-kept operating conditions.

potential gradient. The higher radial velocities may, therefore, indicate regions of high ionization just towards the centerline from the point of interrogation. From Fig. 6.5, it appears that the 13 A case has a more localized region of ionization roughly 0.2 cm downstream of the DCA, whereas the ionization appears to be more distributed in the 12 A case. Both, however, have peaks within 0.2 cm.

Figure 6.6 presents a more global picture of the ion velocities downstream of the DCA for the condition corresponding to that of the 2000 hr wear-test, i.e. 12 A, 27 V, un-keepered. Data were taken over half of the plane. Radial symmetry was assumed for clarity of presentation, and measurements of the radial velocity in the opposite half of the plane also revealed radial velocities away from the centerline. Note the back-flowing ions on centerline and near the 0.3 cm radial position and the high off-axis velocities along the face of the DCA. The largest axial velocities were on the order of 2500 m/s, but radial velocities along the face of the cathode approached 4000 m/s. The region of transition from low to high velocity appears as a quiescent region between 0.2 and 0.4 cm downstream.

Figure 6.7 shows the velocity vectors for the un-keepered 13 A, 25 V operating condition. Note the similarity of the vector field (data at radial positions greater than 0.3 cm were not taken in the 13 A, 25 V case) and the presence of back-flowing ions which indicate that the different un-keepered DCA operating conditions resulted in largely similar plasma environments. There were large radial velocities with back-flowing components along the face of the cathode. There was a region of negligible

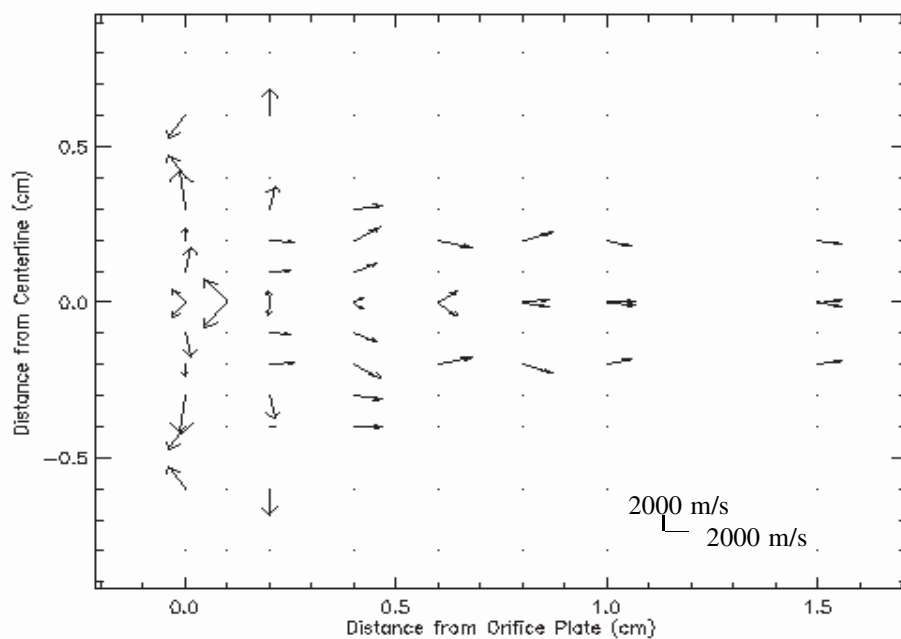


Figure 6.6 Xe II velocity map for 12 A, 27 V un-kept operation. Note the regions of back-flowing ions along the cathode face ($x=0$) and the region of small velocities along the centerline between 0.3 and 0.6 cm downstream.

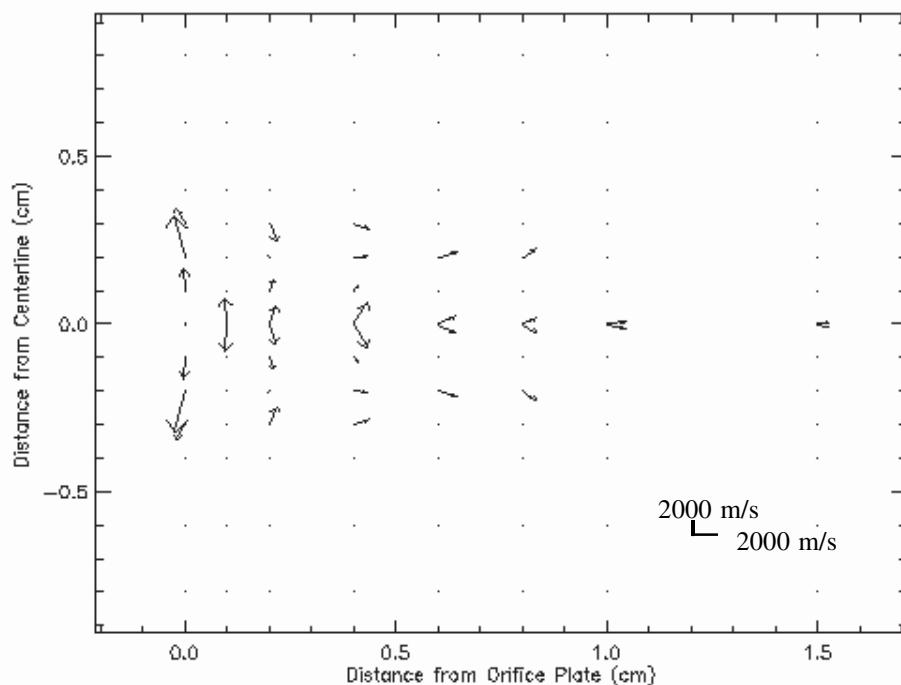


Figure 6.7 Xe II velocity map for 13 A, 25 V un-kept operation. Note the regions of back-flowing ions along the cathode face ($x=0$) and the region of small velocities along the centerline between 0.3 and 0.6 cm downstream.

axial velocities and large radial velocities from 0.2 to 0.4 cm. Beyond 0.5 cm the velocities have small radial components. Axial velocities transition from back-flowing to forward-flowing along the centerline between 0.0 and 0.2 cm. The maximum axial and radial velocities were on the order of 2500 m/s and 4300 m/s, respectively. As in the 12 A, 27 V case, the largest radial velocities occurred along the face of the DCA. The similarities indicate that the erosion rates should be similar between the two cases. However, the larger back-flowing velocities (1300 m/s compared to 1000 m/s) near the orifice plate between radial positions of 0.3 and 0.4 cm indicate the 12 A, 27 V (wear-test) condition should yield slightly greater Mo LIF signals at this point. As illustrated in Fig. 5.10, this is what was observed.

Differences between the two vector fields included larger back-flowing velocities along the DCA face and smaller radial velocities (cf. Fig. 6.5) along the centerline of the plume for the wear-test condition. The larger back flowing velocities may have resulted from the more plume-mode-like state (lower current, lower cathode flow rate, and higher discharge voltage) of the wear-test condition. Centerline radial velocities varied between 300 and 4300 m/s for the 13 A, 25 V case and were typically two to three times larger than for the 12 A, 27 V case. These larger radial velocities may result from a higher ion density associated with 13 A operation.

Energy distributions calculated from the measured velocity distributions along the face of the cathode for the wear-test condition are given in Fig. 6.8. In order to illustrate the magnitude of the energies of the ions moving towards the DCA, these energies are indicated as negative. Note that magnitudes of back-flowing ion energies peak near the radial location of maximum erosion, 0.4 to 0.6 cm. Note also that, at

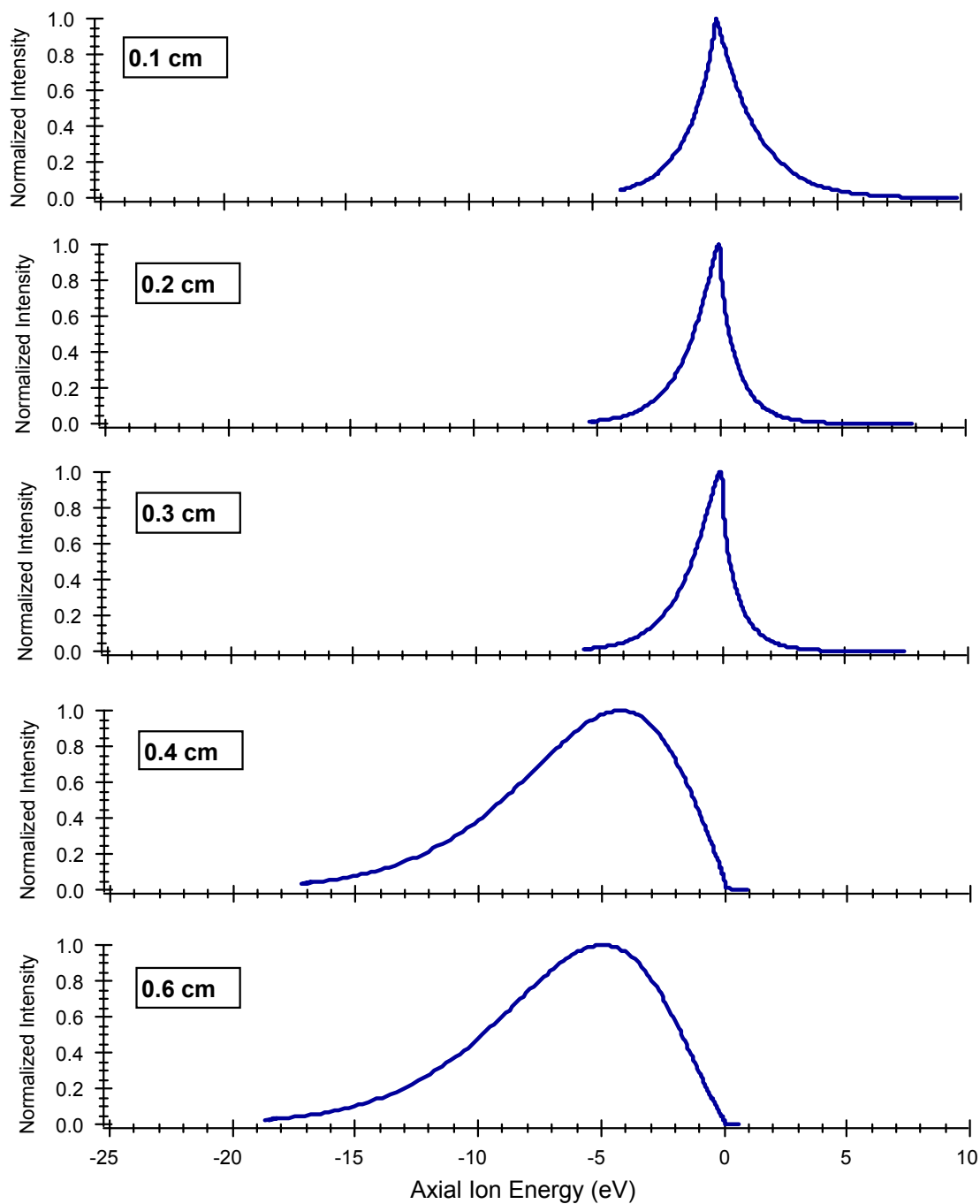


Figure 6.8 Normalized axial Xe II energy distributions as a function of radial distribution along the face of the un-keepered DCA for 12 A, 27 V operation.

these locations, a significant fraction of the ions had energies greater than 5 eV. Again, these profiles result from the deconvolution of the LIF data and do not entail assuming a

Maxwellian distribution. From Fig. 6.6, the ions at 0.4 and 0.6 cm appear to be striking the surface at angles between 45 and 55 degrees. At 55 degrees, the W erosion threshold is near its minimum of roughly 20 eV (Fig. 5.2b), but this is still greater than even the tail of the ion energies given in Fig. 6.8 at 0.4 and 0.6 cm. The integrated fraction of the energy distribution in the high-energy tail (> 18 eV) of the 0.6 cm case is less than one percent of the total. This small fraction could not be responsible for the observed erosion unless the flux of atoms was very large as will be discussed in the next chapter. Therefore, even though the energy and velocity distributions would suggest an erosion pattern similar to that shown in Fig. 5.6, the energies of the Xe II ions measured by LIF are much too small to generate the erosion. However, additional acceleration of the Xe II by the drop across the DCA's plasma sheath or Xe III ions following the same trajectories as the Xe II ions might result in the observed erosion. In addition, the total velocity of the ion composed of both the axial and the radial velocity components may provide significantly more incident energy than the purely axial energy profile presented here. These possibilities will be discussed in detail in Chapter 7.

Ion velocities have also been measured with the FMT running without beam extraction. No back-flowing ions were observed with the same currents and flow rates as maintained during normal operation. Increasing the discharge voltage by significantly decreasing the main flow rate did result in back flowing ions. However, even at roughly the same current and voltage, operation at flow rates significantly different from the nominal NSTAR conditions may not reproduce plasma conditions during nominal operations. This highlights the importance of making DCA erosion measurements with beam extraction.

Keeped Operation

Figure 6.9 compares mean axial centerline velocities for various kepted DCA/FMT operating conditions. The velocities started small and or negative, but increased quickly to a high velocity (>3000 m/s) within 0.2 cm. The velocities then decreased significantly. Most increased again to values comparable to those 1.5 cm downstream of the un-keeped DCA (except for the 12 A, 32 V data which remain at a low velocity, 100 m/s). Figure 6.10 gives the radial variation in axial velocity for the 13 A, 25 V case. Note that the progression with radial position of low to back-flowing, non-back-flowing, and large back-flowing ion velocities is similar to that of

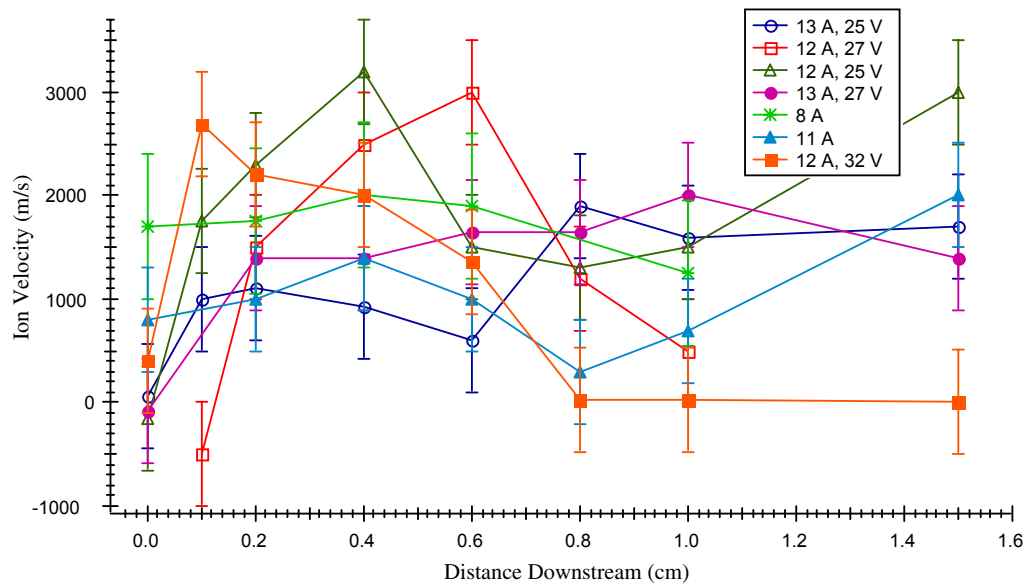


Figure 6.9 Centerline axial Xe II velocities downstream of the kepted DCA.

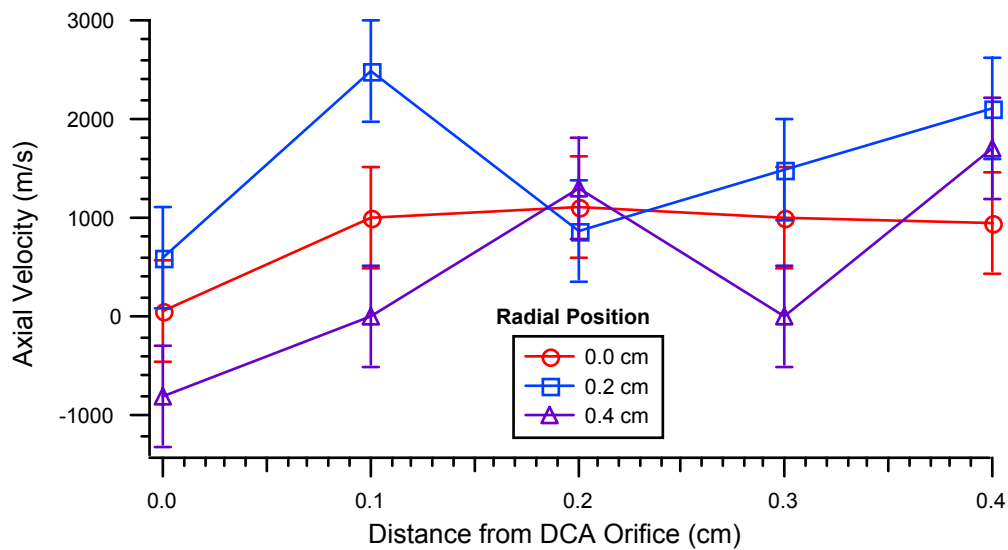


Figure 6.10 Axial velocities off-centerline for the 13 A, 25 V kepteered operating condition.

the un-kepteered wear test condition given in Fig. 6.4. However, in the kepteered case, the back-flowing component along the centerline is negligible and the velocity at 0.4 cm is roughly one half of that in the un-kepteered, 12 A case. Note the energy associated with the back-flowing component in the kepteered case would therefore be one-fourth that of the un-kepteered case.

Figure 6.11 compares the radial velocity components of the kepteered 12 A, 27 V and 13 A, 25 V operating conditions as a function of axial position. Note that the velocities differ significantly from those in Fig. 6.5. Figure 6.11 indicates two regions of high radial velocities: one just downstream of the exit plane and one 0.4 to 1.0 cm downstream. The latter suggests an extended region of ionization. The very high radial velocities at the exit plane may indicate that there is a localized region of ionization very near or in the keeper orifice which is consistent with kepteered operation being closer to spot-mode operation. As for the un-kepteered data, the 13 A

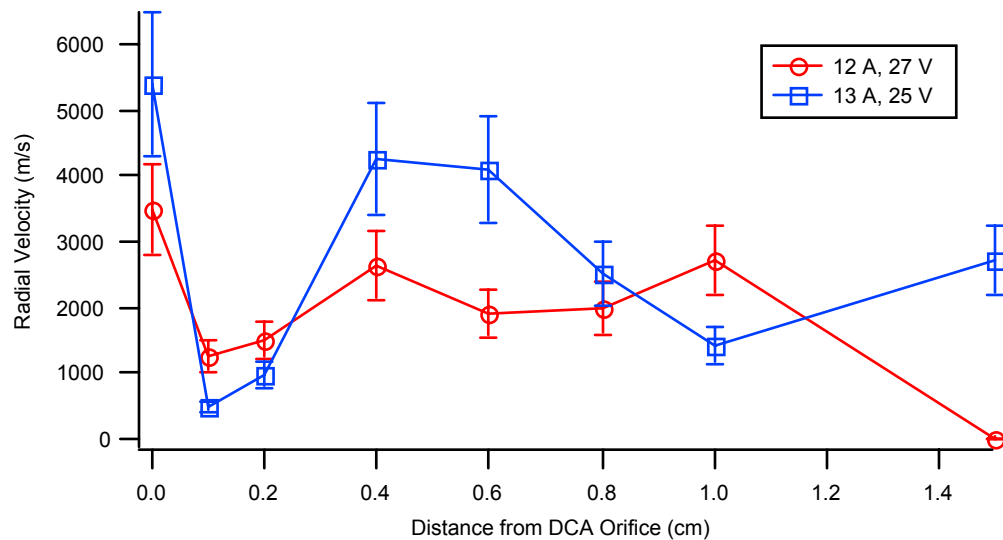


Figure 6.11 A comparison of radial velocities along the centerline for the 12 A, 27 V and 13 A, 25 V kepteered operating conditions.

case has higher radial velocities in a more localized region which would imply a more localized region of ionization. However, both kepteered sets of data indicate a more extended and, by virtue of the generally much higher radial velocities, a more intense region of ionization than the un-kepteered data.

Figure 6.12 maps the ion velocities downstream of the DCA for the 13 A, 25 V condition (which again corresponds to that of the 8200 hr life-test). Note the back and forward-flowing ions across the keeper face and the high off-axis velocities (up to 5400 m/s) at the DCA exit plane. As illustrated in the last few figures, there was a region of low axial and radial velocities up to 0.2 cm downstream of the keeper exit plane. Large radial velocities and small axial velocities occurred along the centerline from 0.4 cm to 0.8 cm suggesting that the region of primary ionization might be confined to a “beam-like” region downstream of the DCA. Again, there may be a slight

offset in the radial position so that the ions with high radial velocities have been accelerated through the gradients near the region of ionization. Note that the high radial velocities decreased significantly farther off centerline until there was little radial velocity (200 m/s) at 0.2 cm off centerline. Non-charge exchange collisions would have this effect, but based on estimates of the ion density on the order of 10^{12} cm^{-3} the mean free path would be too large.² However, significant charge exchange collisions would also have this effect and, from Eqn. 4.5, the cross section is sufficient to indicate that a significant fraction of the ions are undergoing these collisions. Note that the same phenomenon was observed in the un-keepered 13 A, 25 V case (Fig. 6.7). Perhaps the greater flow rate of the 13 A, 25 V case results in a larger number of neutrals which undergo charge exchange collisions.

Figure 6.13 gives the velocity vectors for operating conditions corresponding to the 2000 hr wear-test but in a keepered configuration. Note the presence of back and forward-flowing ions along the keeper face and the similar distribution of axial velocities along the centerline as in the 13 A, 25 V case. The maximum axial velocities were 3000 m/s for the 12 A, 27 V case and 2500 m/s for the 13 A, 25 V case. As in the un-keepered case, the radial velocities along the centerline were smaller for the wear test condition (up to 3500 m/s) than for the 13 A, 25 V condition. Also as in the 12 A, 27 V un-keepered case (Fig. 6.6), the large radial velocities did not decrease significantly off centerline. In addition to a decrease in J_D and an increase in V_D , V_K increased from 4.3 V to 5 V for the keepered wear test condition. This difference may explain why the region of low axial velocities was within 0.5 cm of the orifice plane as opposed to 1.0 cm for the 13 A, 25 V case.

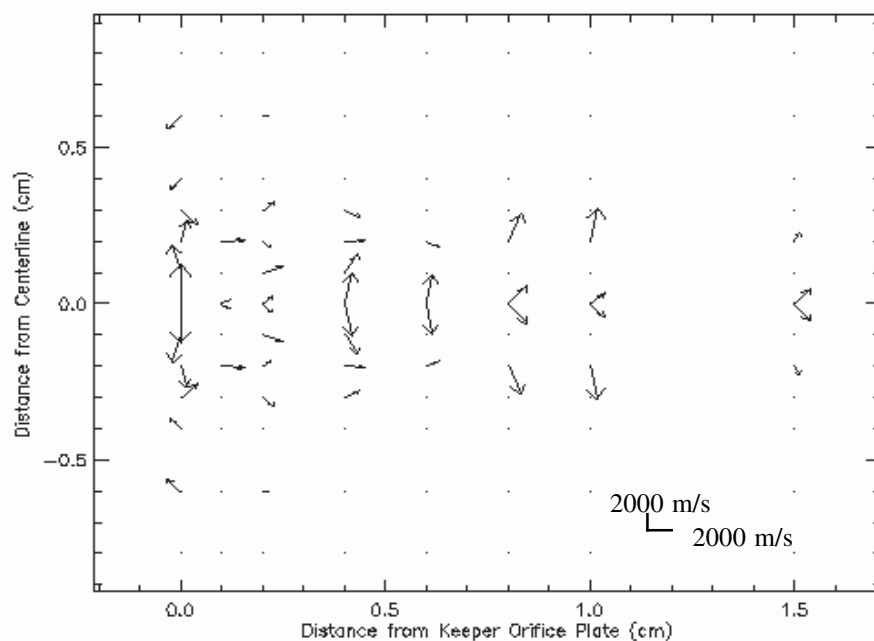


Figure 6.12 Xe II velocity map for 13 A, 25 V keptered operation. Note the regions of back-flowing ions along the cathode face ($x=0$) and the region of small velocities along the centerline between 0.3 and 0.6 cm downstream.

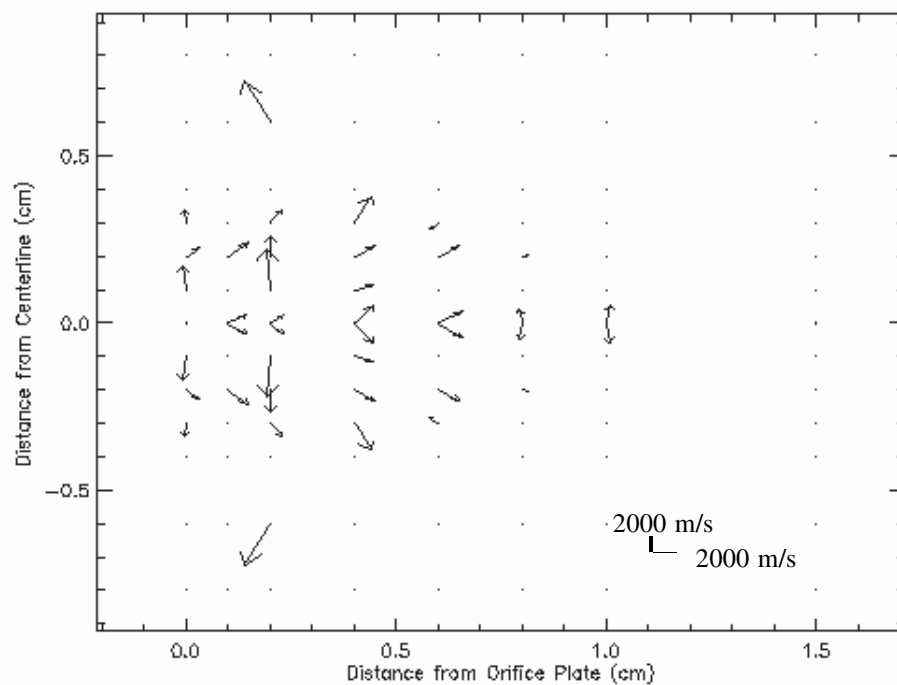


Figure 6.13 Xe II velocity map for 12 A, 27 V keptered operation. Note the regions of back-flowing ions along the cathode face ($x=0$) and the region of small velocities along the centerline between 0.3 and 0.6 cm downstream.

Energy distributions along the face of the keeper are given in Figure 6.14 for the 13 A, 25 V case. Note that magnitudes of back-flowing ion energies peaked farther from the centerline than for the un-keepered data in Figs. 5.6 and 6.8, and that at the 0.6 cm location the ions have roughly the same energy distribution for both cases. The velocity vectors and the radial progression of energy distributions would suggest the erosion pattern in Fig. 5.11. However, the ion energies did not extend above 20 eV which, from Fig. 5.2a, would be the minimum required energy for ions striking at angles of roughly 50 degrees.

Comparison of Velocity Profiles

The keeper electrode appears to have subtly modified the ion velocity pattern downstream of the DCA. In particular, the ions appeared to be created in a more collimated region farther downstream in the keepered cases.

The presence of a potential-hill was strongly suggested by the decrease in axial velocities in the keepered case (Fig. 6.9). Note that in both keepered and un-keepered configurations the DCA ran near plume-mode. In such a mode, the region of ionization required to draw electrons out of the cathode extended significantly downstream of the cathode/keeper orifice. The extended region of increasing ion velocities downstream of the un-keepered DCA (Fig. 6.6) also suggested a potential-hill. Axial velocities for the 2000 hr and 8200 hr wear-tests are compared in Fig. 6.15; the potential-hill/region of primary ionization appears to be closer to the exit plane in the un-keepered case. Similarly, the extended region of acceleration downstream of

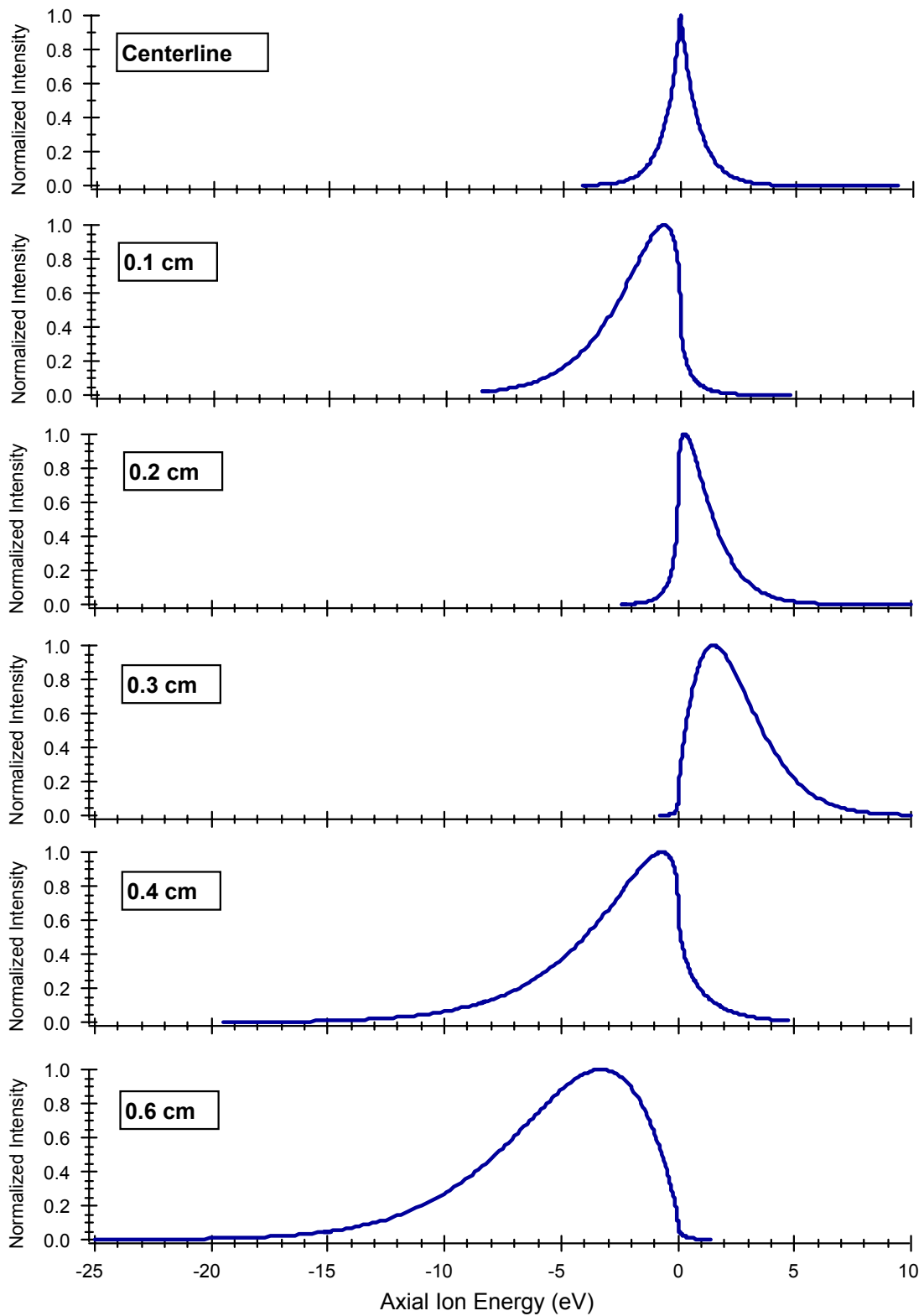


Figure 6.14 Energy distributions across the keeper face. Note the significant energies 0.4 and 0.6 cm downstream (roughly in the center of the keeper).

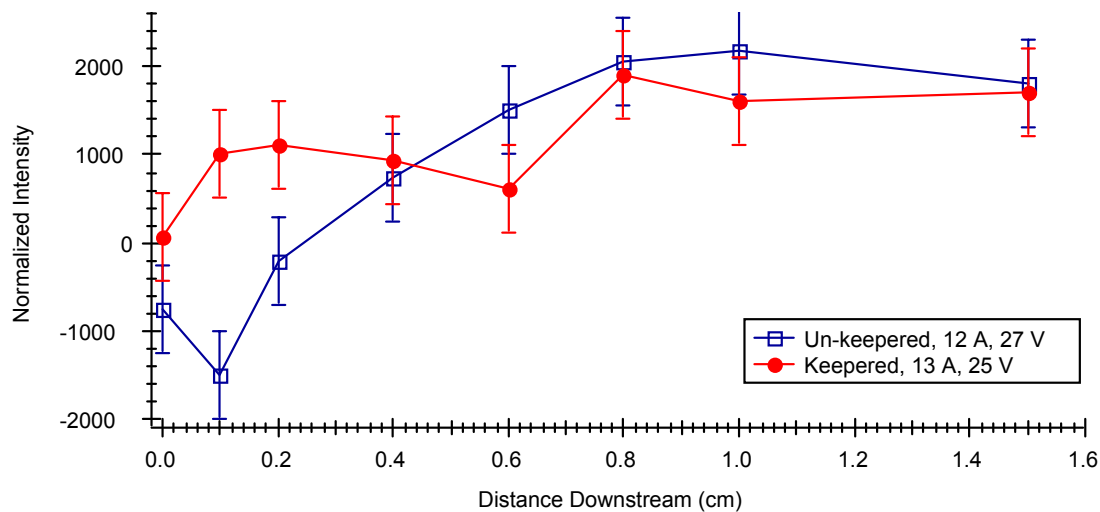


Figure 6.15 A direct comparison of the centerline axial ion velocities for the 2000 hr wear test (un-kept, 12 A, 27 V) and the 8200 hr wear test (kept, 13 A, 25 V).

the un-kept DCA indicates that the hill was near the exit, since there was no significant deceleration further downstream.

The proximity of the potential hill to the DCA exit plane appears to correspond to the increase in the back-flowing component of the ions which were rapidly moving off-axis along the face of the DCA in all cases. Conversely, the rapid increase in ion velocity followed by a region of deceleration indicates that a potential-hill existed on the order of 1 cm from the kept DCA. The increase in potential in the kept configuration probably resulted from a region of greater ionization which would induce a higher potential to maintain quasineutrality. Since this hill was closer to the exit plane in the un-kept case, the back-flowing components of the radially escaping ions would be expected to be greater in the un-kept case than in the kept case, as was observed.

Figures 6.12 and 6.13 show that most ions impacting the DCA surface in the 13 A, 25 V keepered configuration between 0.3 and 0.6 cm off centerline were moving towards the cathode centerline. Note that there were ions impacting the surface with axial and radial back-flowing velocity components 0.6 cm off centerline in both this keepered and in the 12 A, 27 V un-keepered configurations. Perhaps the proximity of the potential-hill in the un-keepered case tended to mask the presence of these ions closer to the centerline. The radially back-flowing ions suggest that a different mechanism of ion acceleration was in part responsible for the erosion. Ions may be accelerating towards the DCA from the ambient plasma.

Recall that HCA operation in the CTF yielded clear differences in centerline ion velocity trends in spot and plume-mode operation. In spot-mode, there was a quick rise in velocity followed by a roughly constant, high velocity away from the HCA. In plume-mode, there was an extended region of back-flowing ions but no downstream decrease in velocity as seen in DCA/FMT operation. The keepered and un-keepered discharge cathode operation appears to fall in between the two cases, though the trends more closely resemble those of plume-mode. This is supported by oscillations observed in the discharge cathode current which do not reflect either the calm of spot-mode or the well defined resonances of plume mode.^{3,4}

Xe II Temperature Measurements

Figure 6.16 shows Xe II axial temperatures as a function of axial position downstream of the un-keepered DCA. With the exception of the 13 A, 25 V case which has a prominent spike near 0.5 cm, the data are fairly constant within the uncertainty of

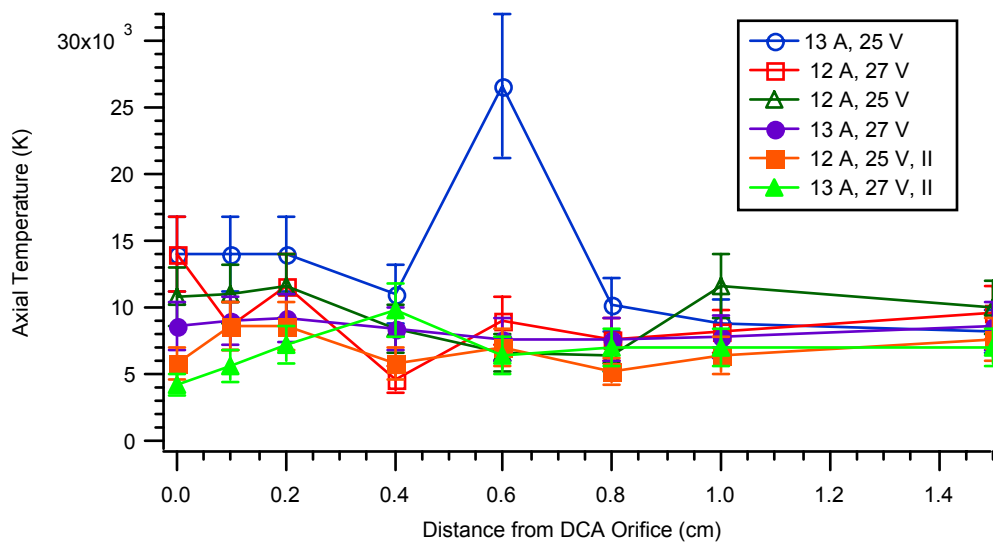


Figure 6.16 Axial temperatures along the centerline of the un-kept DCA for various operating conditions.

the measurement. While some conditions clearly have lower temperatures than others, there is no apparent correlation with J_D , V_D , or \dot{m}_C which would suggest that the variations are primarily due to uncertainties in the data. The mean value is roughly 8500 K or about 0.75 eV.

Despite its anomalous appearance, the spike in the 13 A, 25 V case may have some physical significance. Note that an almost identical trend is observed in Fig. 6.17 for kept operation. In kept operation, the 12 A, 25 V case also exhibits this behavior but to a lesser degree. While the 0.5 cm location is in agreement with the location of high radial velocities in the kept configuration, there is no correlation with the un-kept velocity data. The mean kept temperature along the centerline was less clear than for un-kept operation but all cases were on the order of 11,600 K or 1 eV.

Summary

Xe II velocimetry and velocity mapping were performed in the vicinity of the discharge cathode exit plane for several operating conditions for both the un-kept and kept DCA configurations. Differences in the magnitude of back-flowing velocities suggests that kept operation will reduce DCA erosion. Also, an extended region of high radial velocities in the kept configuration indicate that there is a potentially significant difference in the regions of primary ionization between kept and un-kept operation. High radial velocities and decreasing axial velocities indicate the kept configuration may generate a small potential-hill roughly 0.5 cm downstream of the keeper exit plane. The region of primary ionization and of a possible small potential hill in the un-kept configuration appears to be within 0.2 cm of the cathode orifice plate. These subtle differences may result in the decrease in DCA

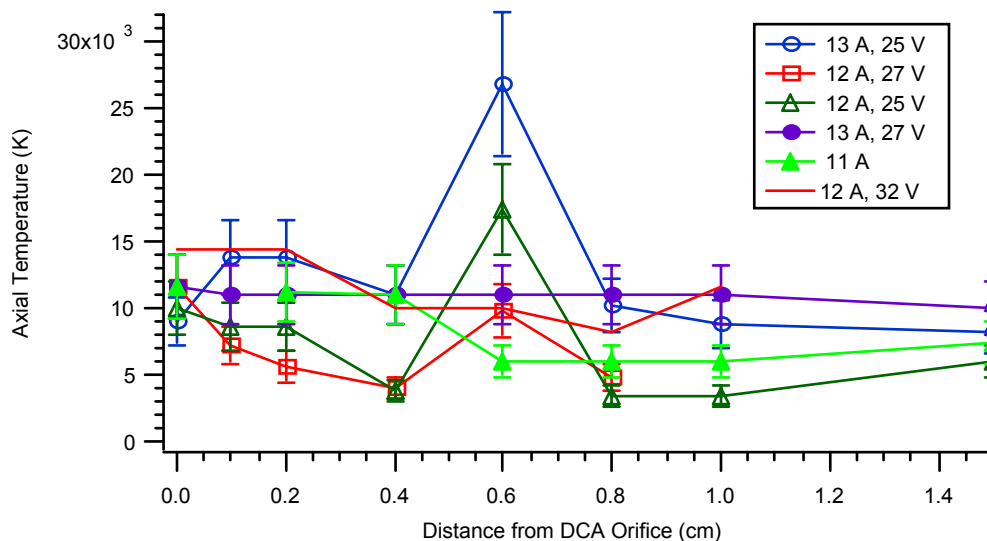


Figure 6.17 Axial temperatures along the centerline of the kept DCA for various operating conditions.

surface erosion as measured in Chapter 5 and observed in the various wear tests. The next chapter will treat the correlation of the erosion and the velocity measurements in greater detail.

Notes to Chapter 6

-
- ¹ Williams, G.J., et al., “Laser Induced Fluorescence Measurement of the Ion Energy Distribution in the Plume of a Hall Thruster,” AIAA-99-2424, 35th Joint Propulsion Conference, (June, 1999).
- ² Williams, G.J., et al., “Laser-Induced Fluorescence Characterization of Ions Emitted from Hollow Cathodes,” AIAA-99-2862, 35th Joint Propulsion Conference (June, 1999).
- ³ Williams, G.J., et al., “Characterization of the FMT-2 Discharge Cathode Plume,” IEPC-99-104, 26th International Electric Propulsion Conference (October, 1999).
- ⁴ Domonkos, M.T., et al., “Low-Current Hollow Cathode Evaluation,” AIAA-99-2575, 35th Joint Propulsion Conference (June, 1999).

CHAPTER 7

CORRELATION OF ION VELOCITIES TO DISCHARGE CATHODE EROSION

Erosion data were consistent with the observed erosion patterns and the radial and back-flowing ions were also phenomenologically consistent with the patterns. However, the differences in keepered and un-keepered ion velocity fields were subtle. The following discussion correlates the DCA erosion to thruster operating conditions in terms of these subtle differences.

Relating Xenon II Energy Measurements to Erosion

Significant radial velocities and back-flowing ions were observed both with and without the keeper. The region of primary ionization appears to influence the negative component to the ions which are being driven radially away from the region of their creation, especially in the un-keepered case. The back-flowing ions received additional energy, enough to exceed the erosion threshold, as they were accelerated through the plasma sheath of the DCA. Note that plasma potentials averaging a few volts above anode potential have been measured a few centimeters downstream of the DCA in ring-cusp ion thrusters.¹ Also, probe measurements in an NSTAR EMT have shown that the discharge voltage is primarily between the cathode and the plasma with very little variation between the anode and plasma potentials.² Since V_p was lower near the exit

plane than it was a few cm downstream in the HCA probe measurements, the cathode fall voltage is conservatively estimated to be 20 V for V_D between 25 and 27 V in the un-keepered configuration.

The presence of back-flowing ions with radial velocities towards the centerline indicated the presence of an additional mechanism by which ions might erode the DCA surface. Bulk discharge chamber ions in the vicinity of the DCA would be drawn to the DCA. As the density of ions increases near the edges of the cathode or keeper, more ions were drawn back towards the lower potential of the DCA surface. This mechanism appears to be secondary as evidenced by the significantly smaller erosion rates measured on the keeper electrode.

Thus, the primary erosion resulted from the high flux of ions from the high-density plume just downstream of the DCA. In addition, secondary erosion resulted from the low flux of ions from the relatively low-density ambient plasma. The Xe III number density will also be greater in the DCA plume and may significantly contribute to the primary erosion, but it should be a much smaller fraction of the secondary flux.

Figures 7.1 and 7.2 illustrate possible Xe II acceleration processes in un-keepered and keepered operation, respectively. These figures give a rough indication of how the velocimetry indicates the plasma downstream of the DCA differs between the two operating configurations. They do not attempt to provide a final and complete description of the structure of the plasma. Note that there are two regions of primary ionization in Fig. 7.2. The region of ionization in the keepered case appears to be

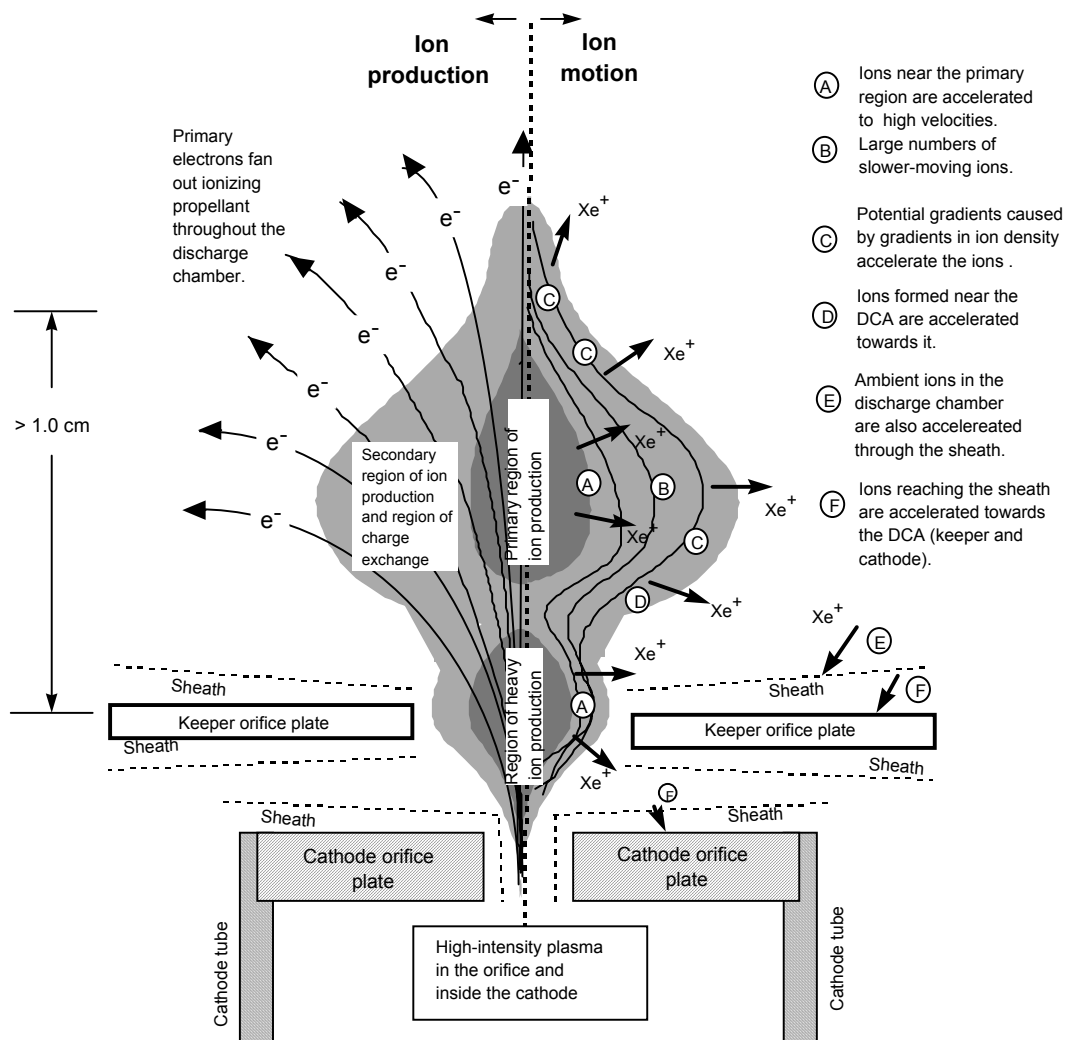


Figure 7.2 Schematic of the proposed Xe II acceleration mechanisms for keptered operation. The figure is not drawn to scale.

narrower and farther downstream than in the un-keptered case. This may be due to the fact that the primary electrons emitted from the keptered DCA are more focused as is illustrated in figures and has been found experimentally.³ The primary electrons emitted from the DCA and shown in the figures gain energies up to the discharge voltage (25 to 27 eV). The regions of varying ion acceleration are labeled in the figures. The contours indicate variations in ion density (and hence plasma potential) with the highest density towards the centerline. The boundaries of the secondary region of ionization are

illustrative and would require detailed probe measurements to determine quantitatively. The vectors associated with ion velocities indicate ions which have been accelerated after leaving the regions of high ion density and have acquired their velocity by passing through a drop in potential.

Un-keepered Operation

The angle of incidence of most of the ions striking the surface in the velocity maps (Figs 6.6 and 6.7) is on the order of 35 degrees. This is approaching the optimal angle for sputtering of roughly 50 degrees. Coupled with the potential drop across the sheath on the cathode, the Xe II ions could have energies between 20 and 38 eV which are sufficient to erode the surface. Figure 7.3 shows the axial Xe II energy distribution including a potential drop of 20 V across the cathode sheath for the un-keepered cathode, 12 A, 27 V, at 0.4 cm. Note the peak of the distribution is now at -25 eV instead of -5 eV. Also, since the entire distribution is being accelerated through a constant potential, the energy distribution retains its shape. This yields an effectively cooler axial “temperature” or narrower velocity distribution,^{4,5} which for the 5 to 25 eV case, results in a temperature decrease of a factor of 5 from 14000 K (12 A, 27 V at the DCA surface) to 2800 K.

Table 7.1 compares the bulk energies of ions before and after the sheath. These energies were calculated using the resultant of the maxima of the axial and radial velocity distribution functions at a given point which is approximately the bulk drift velocity. Thus, the energy reflects the total energy of the ion unlike the axial

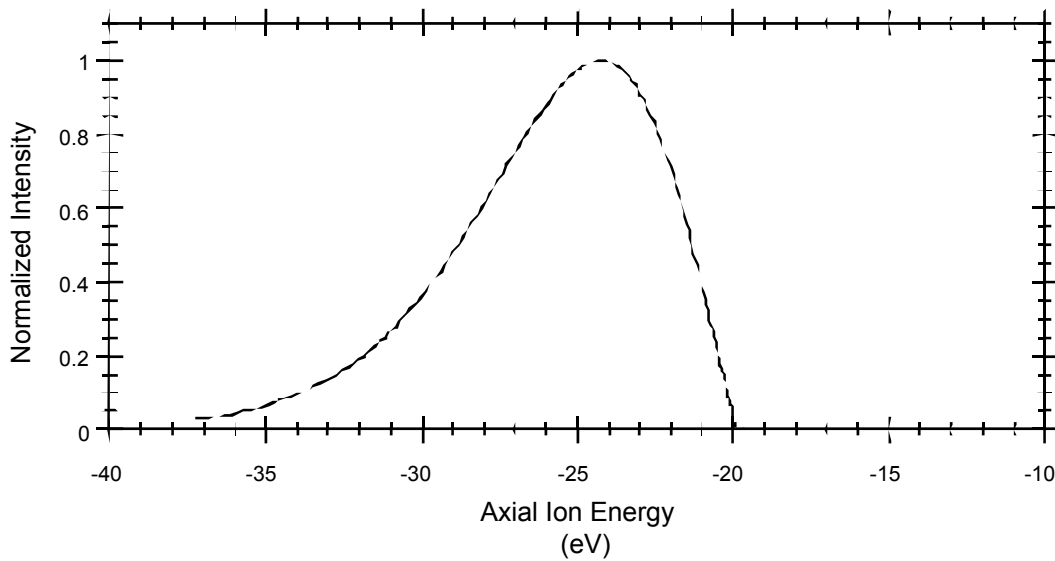


Figure 7.3 Impinging ion energy for un-kept operation.

energy distributions given in Figs. 6.8 and 6.14 (though those axial distributions give an insight into what part of the distribution might be responsible for erosion). Note the change in angle as the ion passes through the sheath. Near the radial locations where the maximum erosion was observed in the un-kept case, the angles are the greatest. Note that bulk energies with the sheath are above the erosion threshold of roughly 30 eV for many cases.

Figure 7.4 shows the region of these Xe II ion energies incorporating the 20 V drop across the sheath in relation to required number densities and W sputter yields and includes only 30 to 55 degree sputter yields. The box indicates the area encompassed by the projected back-flowing ion energies and ion number densities near the DCA. The fluxes were determined from the pre-sheath velocities, and the sheath energy was added to calculate the yield. Note that the energies were sufficient to generate the observed erosion. Assuming $n_i = 10^{13} \text{ cm}^{-3}$ on centerline, as was

Table 7.1: A comparison of ion energies before and after passing through the sheath.
Normal incidence corresponds to 0 deg, parallel to 90 deg, and directly away from surface to 180 deg.

Radial position (cm)	Before sheath			Trough sheath (20 V to cathode)		
	Velocity (m/s)	Energy (eV)	Angle (degree)	Velocity (m/s)	Energy (eV)	Angle (degree)
Un-keepered 12 A, 27 V						
0.0	1620	1.8	77	6570	29	12
0.1	600	0.49	130	-	-	-
0.2	3000	6.1	89	6240	26	29
0.3	4000	11.	85	7020	33	35
0..4	2800	5.3	62	7140	35	20
0.6	2600	2.7	66	6900	32	20
Un-keepered 13 A, 25 V						
0.0	1870	2.4	135	-	-	-
0.1	3400	7.9	88	6530	29	31
0.2	6900	32	77	9710	64	44
0.3	2800	5.3	63	7130	35	21
Keepered 12 A, 27 V						
0.1	3530	8.5	82	6350	27	33
0.2	2050	2.8	135	-	-	-
0.3	2600	4.6	86	5680	22	27
0.4	2800	5.3	-	-	-	-
Keepered 13 A, 25 V						
0.0	5400	20	90	-	-	-
0.1	3900	10.5	75	7000	33	33
0.2	2900	5.6	100	-	-	-
0.3	2650	4.8	120	-	-	-
0..4	1900	2.5	55	6300	27	16
0.6	2300	3.7	47	6670	30	15

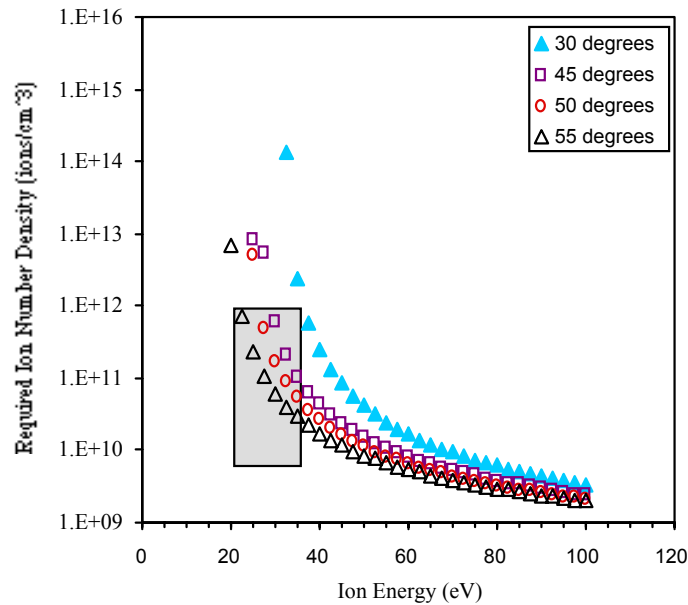


Figure 7.4 Required Xe II number densities to produce the W erosion in the 2000 hr wear test illustrating the impact of the fall across the plasma sheath.

measured by probes in the plume of an HCA, at 0.3 cm, $n_i \approx 10^{12} \text{ cm}^{-3}$ which is where the required number density curves pass through the available energies in Fig. 7.4.

Keeped Operation

Figure 7.5 shows the required number densities as a function of ion energy to produce the Mo erosion of the keeper observed in the 8200 hr wear-test. Note that the required densities are an order of magnitude lower than for W erosion of the cathode orifice plate in un-keeped operation. Assuming that the plasma potential downstream of the keeped DCA is equal to that of the un-keeped DCA, the potential drop to the keeper differs from that to the cathode by the keeper voltage, V_k . Typically $V_k \approx 4 \text{ V}$. Figure 7.6 shows ion energies for ions impinging on the keeper at 0.4 cm for the 13A, 25 V case assuming a 16 V fall to the keeper. Again the

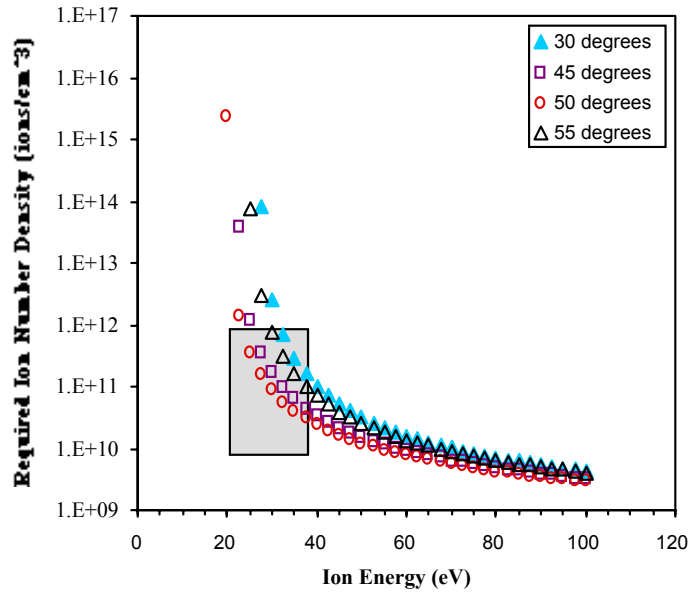


Figure 7.5 Xe II number densities required for the observed keeper erosion.

distribution retains its shape during acceleration through the sheath. Note that all of the erosion observed in the 2000 and 8200 hr endurance tests can be explained in terms of trends in the measured ion velocities as shown in Table 7.2.

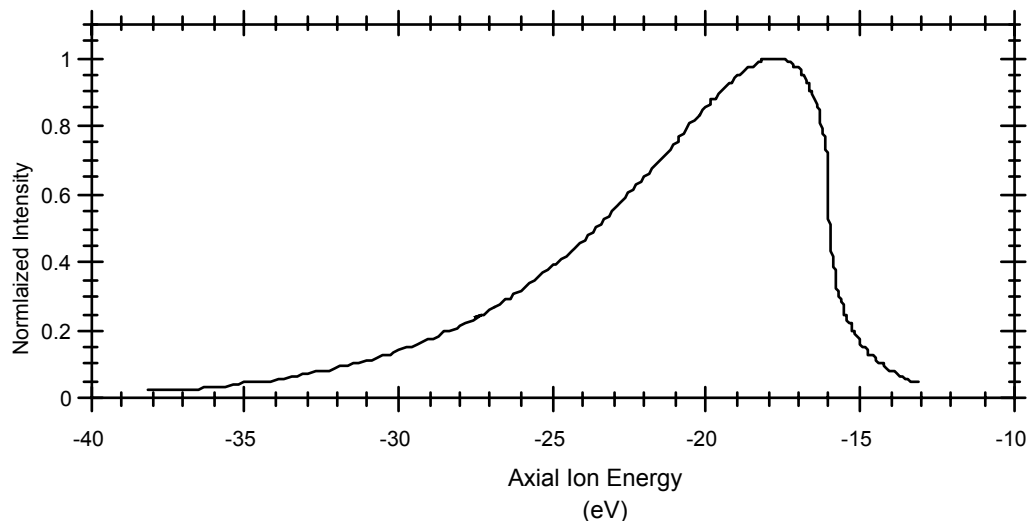


Figure 7.6 Impinging ion energies for keepered operation.

Role of Xe III

Xenon III ions should be accelerated along the same paths as Xe II ions and may result in the majority of the erosion. Due to its higher potential energy, the sputter yield of a doubly charged ion is greater than that of a singly charged ion with twice the kinetic energy. However, as a first approximation, the increase in sputter yield is assumed to be only a function of Xe III's higher kinetic energy. Figures 7.7a and 7.7b show the required number densities of Xe III to produce the observed un-keepered and keepered erosion. Densities above 10^{12} cm^{-3} remove much of the Xe III energy dependence indicating doubly-charged ions between 40 and 60 eV could result in the observed erosion.

An estimate of the ratio of Xe III to Xe II number densities near the discharge cathode can be inferred from the ratio downstream of the thruster since recombination

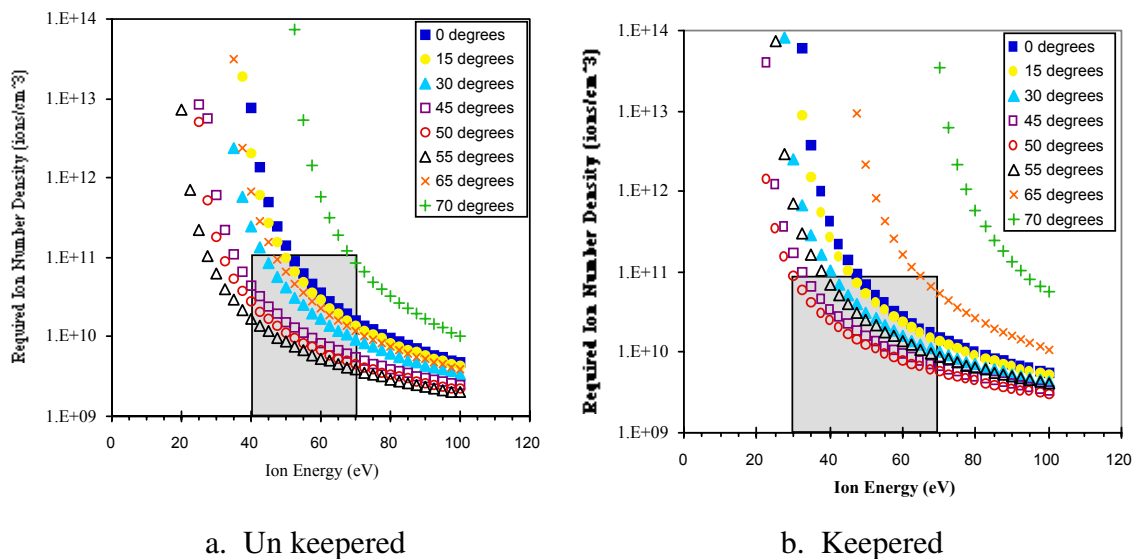


Figure 7.7 Xe III number densities required to produce the observed erosion.

Table 7.2 Explanations for observed DCA erosion

Observed Erosion	Test	Explanation
Heater coil eroded flush with the orifice plate	2000 hr	High-velocity ions radially emanating from the DCA plume
Electron beam weld eroded flush with the orifice plate	2000 hr	A combination of radial and back-flowing ions passing through the plasma sheath
Orifice plate eroded near its outer edge	2000 hr	Back-flowing ions originating in the plume
Cathode tube eroded with a curvature towards its outer edge	2000 hr	A combination of back-flowing ions originating in the plume and in the ambient plasma
Keeper orifice eroded to a chamfer	8200 hr	Back-flowing ions from the ion plume (potentially coupled to impinging ions generated in the cathode-to-keeper gap)
Keeper orifice plate eroded across its surface	8200 hr	Back-flowing ions originating in the ambient plasma
Keeper orifice plate edge bevelled	8200 hr	Back-flowing ions from the ambient plasma

collisions should be negligible. Ratios as high as 0.1 have been measured downstream of the thruster for various operating conditions.⁶

The Xe III fraction can also be approximated by performance calculations.⁷ The ratio of doubly charged ion to singly charged ion current density (j_{++}/j_{+}) in the beam can be expressed as a function of the discharge efficiency (where both Xe II and Xe III are produced):

$$\frac{j_{++}}{j_{+}} = 1.2439 - 7.1078v_D + 15.3317v_D^2 - 14.7856v_D^3 + 5.4228v_D^4 \quad (7.1)$$

where the discharge efficiency is

$$v_D = \frac{J_B}{0.07175(\dot{m}_M + \dot{m}_C)}$$

A comparison of the density ratios in the beam and the discharge is meaningful because the ion velocities result from electric fields which implies continuity so that the ratio of densities in the beam can be expressed as a function of the current densities and then equated to the ratio of densities in the discharge chamber:⁸

$$\left(\frac{n_{++}}{n_+}\right)_{\text{Beam}} = \left(\frac{(j_{++})_{\text{Beam}}}{2e\sqrt{\frac{4eV_B}{m}}}\right) \left(\frac{e\sqrt{\frac{2eV_B}{m}}}{(j_+)_{\text{Beam}}}\right) = \frac{1}{2\sqrt{2}} \left(\frac{j_{++}}{j_+}\right)_{\text{Beam}} = \frac{1}{2\sqrt{2}} \left(\frac{j_{++}}{j_+}\right)_{\text{Disch}} = \left(\frac{n_{++}}{n_+}\right)_{\text{Disch}} \quad (7.2)$$

Table 7.3 gives Xe III to Xe II density fractions calculated using Eqn. 7.2 as a function of operating condition. Note that the fractions are all on the order of 0.02 and that between 8.3 A and 13.1 A (1.0 and 2.3 kW NSTAR operating conditions) there is little variation despite the increasing J_D to \dot{m}_C ratio from 1.0 to 1.5 kW operation. The fraction does increase slightly for the 2000 hr wear test conditions (the last condition in the table). Thus, the Xe III density may be on the order of 10^{10} cm^{-3} to 10^{11} cm^{-3} for

Table 7.3: Calculated Xe III to Xe II current fractions for the NSTAR throttling points.

\dot{m}_M (sccm)	\dot{m}_C (sccm)	J_D (A)	V_D (V)	J_B (A)	v_D	j^{++}/j^+	n_{++}/n_+
5.9	2.50	4.3	25.4	0.5	0.83	0.026	0.009
5.9	2.50	5.1	25.4	0.5	0.83	0.026	0.009
8.3	2.50	6.1	25.4	0.7	0.90	0.046	0.016
11.3	2.50	7.1	25.4	0.9	0.91	0.048	0.017
14.4	2.50	8.3	25.4	1.1	0.91	0.048	0.017
18.5	2.7	10.2	25.4	1.4	0.92	0.053	0.019
21	3.1	11.6	25.4	1.6	0.93	0.055	0.019
23.4	3.7	13.1	25.4	1.76	0.91	0.047	0.017
22.9	3.0	12.1	26.8	1.76	0.95	0.067	0.024

un-keepered operation. This fraction may not be sufficient for Xe III to produce the observed erosion by itself.

Recent retarding potential analyzer (RPA) measurements of Xe II and Xe III downstream of an HCA also lend some insight into the nature of Xe III emitted from or created near the HCA.⁹ The Xe III flux decreased more rapidly with angle off centerline than did the Xe II flux. This suggests that Xe III ions may not have a velocity field similar to that of Xe II after all. The Xe III flux varied as J_k^4 which would imply that higher keeper voltages, V_k , would indicate a larger fraction of Xe III ions. This is counter-intuitive for the DCA since higher V_k would imply lower V_d which exhibits less erosion and a more stable discharge. However, the observation that the Xe III to Xe II ratio decreased with an increasing cathode flow rate implies that higher discharge voltages will yield a higher Xe III to Xe II ratio.

Measurement of relative Xe III densities as a function of operating condition and of Xe III velocities proved beyond the scope of this investigation. A modified dye circulator providing substantially higher dye flow rates and newly developed near-UV intra-cavity laser optics are required.

Summary

There is good correlation between the measured erosion and ion velocities. Acceleration of the Xe II ions through the DCA plasma sheath provided them with energies sufficient to generate the erosion. Both Xe II and Xe III have sufficient energies to produce the cathode erosion. However, the relative contributions of Xe II and Xe III to the erosion process depend on their number densities.

Notes to Chapter 7

-
- ¹ Hayakawa, Y., et al., “Measurements of Electron Energy Distributions in a 14 cm diameter Ring-Cusp Ion Thruster,” AIAA-89-2715, 25th Joint Propulsion Conference (July, 1989).
- ² Foster, J.E., et al., “Plume and Discharge Plasma Measurements of an NSTAR-type Ion Thruster,” AIAA-2000-3812, 36th Joint Propulsion Conference (July, 2000).
- ³ Jack, T.M., et al., “The Effect of the Keeper Electrode on Hollow Cathode Characteristics,” AIAA-2000-3533, 36th Joint Propulsion Conference (July, 2000).
- ⁴ Kaufman, S.L., “High-Resolution Laser Spectroscopy in Fast Beams,” *Optics Communications*, **17** (3) June, 1976, 309–312.
- ⁵ Meehan, N.B., et al., “Optical Study of Anomalous Electron Transport in a Laboratory Hall Thruster,” AIAA-99-2284, 35th Joint Propulsion Conference, June, 1999.
- ⁶ Rawlin, V.K., et al., “NSTAR Flight Thruster Qualification Testing,” AIAA-98-3936, 34th Joint Propulsion Conference (July, 1998).
- ⁷ Patterson, M., et al., “Ionpro Version 3,” 1993.
- ⁸ Williamson, W.S., “Ion Chamber Sputtering Investigation,” Hughes Research Laboratories Final Report IS-679, 1974.
- ⁹ Crofton, M.W., “The Feasibility of Hollow Cathode Ion Thrusters: A Preliminary Characterization,” AIAA-2000-5354, 36th Joint Propulsion Conference (July, 2000).

CHAPTER 8

CONCLUSIONS AND FUTURE WORK

As ion thrusters are scaled to higher and lower powers they will enable more ambitious space exploration and more efficient near-earth maneuvering for commercial and military purposes. However, the erosion observed in several 30 cm ion thruster endurance tests has raised the concern that the current design of the discharge cathode assembly or the selection of primary thruster operating conditions will generate even greater erosion which might preclude the use of the ion thruster as currently designed or operated. This investigation presents the first real-time, in situ experimental analysis of DCA erosion and of the plasma near the DCA responsible for the erosion. Real-time, in situ, relative discharge cathode assembly erosion rates have been measured as a function of 30 cm ion thruster operating conditions. The data from this investigation support a phenomenological model of the DCA erosion process and indicate there are both design and operational factors which can reduce the erosion.

This investigation incorporated two parallel endeavors which, when eventually coupled, provided the data necessary to predict how DCA erosion will vary with thruster operation: 1) the development of a laser-induced fluorescence diagnostic capability which can measure three components of velocity simultaneously or the relative density of an eroded material and 2) the design, assembly, and maintenance of a NSTAR-like 30 cm ion thruster which was operated in a university laboratory. The LIF

capability developed around a Coherent ring-dye laser was demonstrated on HCA,¹ Hall thruster,² and ion thruster³ electric propulsion devices. Xe I, Xe II, W, and Mo species were detected using very-near UV to visible wavelengths. The ion thruster's performance was comparable to that of both the EMT's used in the endurance tests and to that of the thruster now on Deep Space 1. Conclusions drawn from the data collected using the LIF capability on the thruster is summarized below and should be transferable to other NSTAR-type thrusters.

Discharge Cathode Erosion Processes

DCA erosion was observed under all operating conditions and in all configurations. The erosion was most likely caused by back-flowing Xe II and, possibly, Xe III ions. Both W and Mo erosion scaled roughly linearly with discharge current. The dependence on discharge voltage was proportional, but small. As observed in the wear tests, the erosion rate of the keeper was roughly one fourth that of the cathode tube in un-keepered operation. The radial variation in LIF signals of the eroded species was in excellent agreement with both Mo and W erosion patterns in both keepered and un-keepered configurations

The rate of erosion is determined by the plasma properties downstream of the DCA. Erosion rates measured without the magnetic field or the geometry of the thruster's discharge chamber or without beam extraction will not produce accurate predictions of these rates under nominal thruster operating conditions even for the same cathode current and discharge voltage. However, trends discovered in such tests such as the influence of a potential hill on back-flowing ions will provide valuable insight into the selection of thruster operating conditions if the plasma properties associated

with the thruster operating conditions are known. For example, strong plume-mode HCA operation yielded back-flowing ions with high velocities. Operation of the DCA at strong plume-mode conditions will also yield back-flowing ions with high velocities, and the velocity distributions indicated that nearly all of the ions within the first few millimeters would be back-flowing in these cases.

The keeper electrode changed the nature of the plasma downstream of the discharge cathode by moving or extending the region of ionization downstream of the cathode. This reduced or eliminated the upstream deflection of radially moving ions, thus significantly reducing the DCA erosion. Unless the discharge operating condition is significantly altered or the discharge cathode is redesigned, it appears that the keeper electrode is necessary to prevent potentially life-limiting erosion of the DCA at high powers.

Predictions of DCA Erosion

The large radial velocities observed in all DCA configurations and at all operating conditions indicates that cathode potential surfaces in close proximity and radially outward from the plane of the DCA will experience significant erosion. Such erosion has in fact been observed in several tests. The keeper may also experience significant erosion if its axial position or orifice diameter is such that the ionization region is brought towards the cathode exit plane. Optimization of the keeper geometry was beyond the scope of this investigation.

The DCA erosion will increase as the discharge current is increased for NSTAR-like flow-rates and beam currents. However, as mentioned above, the ability to predict the erosion under different throttling conditions, e.g. those of the CNSR mission,

depends on the ability to predict the plasma environment produced by these new conditions. The following general trends were observed in this investigation:

- Higher beam currents for the same discharge current and flow rate increase the discharge voltage increasing erosion
- Higher beam currents for the same discharge current and total flow rate increase the Xe III to Xe II ratio increasing erosion
- Higher DCA keeper voltages (which in the nominal thruster configuration imply higher keeper electron currents) tend to move the DCA closer to spot-mode and thus tending to decrease DCA erosion.

Demonstration of Laser-Induced Fluorescence

A multiple capability laser-induced fluorescence diagnostic system was developed and demonstrated as part of this investigation. The Coherent 899-29 laser provided repeatable, reliable scanning over tens of GHz from roughly 398 nm to 690 nm depending on the dye and laser optics. The laser operated smoothly over the entire range of wavelengths. Stanford lock-in amplifiers proved much more capable than the less sophisticated Thor lock-in amplifiers with phase matching though both were used with success.

The multiplex velocimetry technique was demonstrated in cathode plume investigations, both internal and external to an ion thruster. The use of mirrors and beam splitters instead of specially designed single piece parallel beam optics to generate the parallel beams required for the multiplex interrogation introduced some uncertainty in the angles of interrogation. In the future, the more expensive parallel beam optics might

be used when the beam separation is relatively small, e.g. for the lateral beam and for the second axial beam. The error introduced by the two-optic method was more critical in the interrogation of HCA and DCA plumes than in thruster plume interrogation because the error is absolute (about 500 m/s) not relative and is largely negligible in the high-velocity thruster plumes.

Several interrogation/fluorescence wavelength pairs were identified and utilized in this investigation in addition to the well-established Xe II 605.1—529 nm transition. These included a strong 603—550 nm Mo transition, a strong 582—618 nm Xe I transition, a moderately-strong 429—427 nm W transition, and a weak 410—405 nm Xe II transition. The grouping of transitions around 600 nm allows interrogation of Xe I, Xe II and Mo species with minimal adjustments to laser and detector frequencies. Interrogations of all three species in the same afternoon of testing became routine. None of these transitions interrogated the ground state of the species, and, thus, all required modeling to relate the measured intensity to the population of the ground state.

Suggested Future Work

Since the LIF data were time averaged over tens of seconds, erosion induced by fluctuations in the plasma would also have been indistinguishable from that caused by steady-state ion impingement. Equally, the ion velocities would be time-averaged and may or may not include contributions from these effects. While it is known that fluctuations in the cathode voltage are present, the resolution of ion velocities and erosion measurements on time scales of μs was beyond the scope of this investigation.

The combination of small angles between interrogating beams and of fluctuations in the reference cell datum resulted in significant uncertainty in the ion

velocity measurements. While the reference cell was stabilized, the angles could not be increased without significantly modifying the FMT. Technically possible, such modifications (e.g. providing optical access into the discharge chamber from just upstream of the ion grids) were beyond the scope of this investigation. However, doubling or tripling the angles of interrogation would increase the velocity resolution significantly and would provide a more rigorous quantification of the influence of the potential-hill.

Xe I velocimetry near the DCA would provide more insight into the role charge exchange plays in the distribution of high-energy and back-flowing ions. The primary limitation would be modeling the Xe I spectra to the high degree that Xe II spectra has been modeled. A first order velocimetry could be performed using the models already developed, and that might be sufficient to verify the presence of significant numbers of high-velocity neutrals.

A calibrated ion source could provide a real-time calibration of the erosion species LIF. This would provide a real-time absolute erosion-rate capability. Detailed spectral line modeling would provide a much more accurate measurement of the temperature of these species which would yield greater accuracy in the conversion of LIF signal to erosion rate measurement. Also, a multiplex LIF tool with greater axial angles of interrogation would significantly increase the accuracy of the axial ion velocity measurements. This would entail modification of the optical access to the FMT. All of these are left to future investigations.

Quantification of Xe III ion velocities and densities as a function of operating condition would be of great value. The current UV configuration of the dye laser does not permit operation below 398 nm. The primary Xe III transitions are near 392 nm. Incorporation of a high-pressure dye circulator and nozzle, newly developed UV optics, and newly developed dye solvent for extended operation in the UV should permit extended operation at relatively high-power near 392 nm.

Lastly, direct measurement of plasma properties such as ion number density, electron temperature, and plasma potential in the vicinity of the DCA would be invaluable. These data would complete the description of the plasma and permit conclusive evaluation of the sensitivity of discharge parameters on operating condition and keeper configuration. The high-speed axial reciprocating probe (HARP) used for internal measurements in Hall thrusters may be used to measure these quantities in the ion thruster in the future.⁴

Notes to Chapter 8

- ¹ Williams, G.J., et al., “Laser-Induced Fluorescence Characterization of Ions Emitted from Hollow Cathodes,” AIAA-99-2862, 35th Joint Propulsion Conference (June, 1999).
- ² Williams, G.J., et al., “Laser Induced Fluorescence Measurement of the Ion Energy Distribution in the Plume of a Hall Thruster,” AIAA-99-2424, 35th Joint Propulsion Conference, (June, 1999).
- ³ Williams, G.J., et al., “Characterization of the FMT-2 Discharge Cathode Plume,” IEPC-99-104, 26th International Electric Propulsion Conference (October, 1999).
- ⁴ Haas, J.M., et al., “Hall Thruster Discharge Chamber Plasma Characterization Using a High-Speed Axial Reciprocation Electrostatic Probe,” AIAA-99-2426 (June, 1999).

BIBLIOGRAPHY

- Askerov, S.G., and L.A. Sena, "Cathode Sputtering of Metals by Slow Mercury Ions," *Soviet Physics—Solid State*, **11** (6) 1969, 1288–1293.
- Bay, H.L., "Laser-Induced Fluorescence as a technique for Investigations of Sputtering Phenomena," *Nuclear Instruments and Methods in Physics Research B*, **18**, 1987, 430–445.
- Beattie, J.R., and J.N. Matossian, "High-Power Ion Thruster Technology," NASA Technical Report CR–195477, 1992.
- Bilen, S.G., et al., "The Far-Field Plasma Environment of a Hollow Cathode Assembly," AIAA–99–2861, 35th Joint Propulsion Conference (June, 1999).
- Bohdansky, J., "A Universal Relation for the Sputtering Yield of Monatomic Solids at Normal Ion Incidence," *Nucl. Instr. And Meth. In Phys. Res.*, **B2** (587) 1984.
- Brophy, J.R., and C.E. Garner, "Tests of High Current Hollow Cathodes for ion Engines," AIAA–88–2913, 24th Joint propulsion Conference, (July, 1988).
- Brophy, J.R., et al., "The Ion Propulsion System on NASA's Space Technology 4/Challengion Comet Rendezvous Mission," AIAA–99–2856, 35th Joint Propulsion Conference, (July, 1999).
- Calaway, W. F., et al., "Laser-Induced Fluorescence as a Tool for the Study of Ion Beam Sputtering," *Handbook of Ion Beam Processing Technology*, Noyes Publications, park Ridge, NJ, 1989, pp. 112–127.
- Cedolin, R.J., et al., "Laser-Induced Fluorescence Diagnostics for Xenon Hall Thrusters," AIAA–96–2986, 32nd Joint Propulsion Conference, (July, 1996).
- Collier, M., et al., "Ionpro Version 3," 1993.
- Corliss, C.H., and W.R. Bozman, *Experimental Transition Probabilities for Spectral Lines of Seventy Elements*, National Bureau of Standards Monograph 53, 1962, pp. 195–219 and 499–519.

- Crofton, M.W., "Laser Spectroscopic Study of the T5 Ion Thruster," AIAA-96-5151, 32nd Joint Propulsion Conference (July, 1996).
- Crofton, M.W., "The Feasibility of Hollow Cathode Ion Thrusters: A Preliminary Characterization," AIAA-2000-5354, 36th Joint Propulsion Conference (July, 2000).
- Deininger, W.D., "Advanced Propulsion System Options for Geostationary Satellites," AIAA-94-3001, 30th Joint Propulsion Conference (June, 1994).
- Domonkos, M.T., et al., "Low Current Hollow Cathode Evaluation," AIAA-99-2575, 35th Joint Propulsion Conference (June, 1999).
- Domonkos, M.T., "Evaluation of Low-Current Orificed Hollow Cathodes," Ph.D. Thesis, The University of Michigan, October, 1999, pp. 153-157.
- Duchemin, O.B., et al., "A Review of Low-Energy Sputtering Theory and Experiments," IEPC-97-068, 25th International Electric Propulsion Conference, (October, 1999).
- Eckbreth, A.C., *Laser Diagnostics for Combustion Temperature and Species*, Abacus Press, Cambridge, 1988, pp. 72-73.
- Eckstein, W., et al, "Threshold Energy for Sputtering and Its Dependence on Angle of Incidence," *Nucl. Instr. And Meth. In Phys. Res.*, **B83** 1993, 95-109.
- Friedly, V.J., and P.J. Wilbur, "High-Current Hollow Cathode Phenomena," *Journal of Propulsion and Power*, **8** (3) 1992, 635-643.
- Gaeta, C.J., et al., "Plasma Erosion Rate Diagnostics Using Laser-Induced Fluorescence," *Review of Scientific Instruments*, **63** (5) 1992, 3090-3095.
- Gaeta, C.J., et al., "Erosion Rate Diagnostics in Ion Thrusters Using Laser Induced Fluorescence," *Journal of Propulsion and Power*, **9** (3) 1993, 369-376.
- Griem, H.R., *Plasma Spectroscopy*, McGraw Hill, New York, 1964, pp. 129-160.
- Gulczinski, F.S., and R.A. Spores, "Analysis of Hall Effect Thrusters and Ion Engines for Orbit Transfer Missions," AIAA-96-2973, 32nd Joint Propulsion Conference (July, 1996).
- Haas, J.M., et al., "Hall Thruster Discharge Chamber Plasma Characterization Using a High-Speed Axial Reciprocation Electrostatic Probe," AIAA-99-2426 (June, 1999).
- Hubin, J.D., *NRL Plasma Formulary*, Office of Naval Research, 1998.

- Huddleston, R.H., and S.L. Leonard, *Plasma Diagnostic Techniques*, Academic Press, New York, 1965, pp. 208–214.
- Husinsky, W., “The Application of Doppler Shift Laser Fluorescence Spectroscopy for the Detection and Energy and Energy Analysis of Particles Evolving from Surfaces,” *Journal of Vacuum Science and Technology*, **B3** (5) 1985, 1546–1559.
- Hutchinson, I.H., *Principles of Plasma Diagnostics*, Cambridge University Press, 1987, pp. 62–66.
- Incropera, F.P., and D.P. DeWitt, Fundamentals of Heat and Mass Transfer, 3rd ed., John Wiley and Sons, 1990, pp. 710–711.
- Jack, T.M., et al., “The Effect of the Keeper Electrode on Hollow Cathode Characteristics,” AIAA–2000–3533, 36th Joint Propulsion Conference (July, 2000).
- Jahn, R.G., *Physics of Electric Propulsion*, McGraw Hill, 1968, pp. 2–20.
- Katz, I., and M.J. Patterson, “Optimizing Plasma Contactors for Electrodynamic Tether Missions,” Presented at Tether Technology Interchange, September 9, 1997, Huntsville, AL.
- Kamayama, I., and P.J. Wilbur, “Characteristics of Ions Emitted from High-Current Hollow Cathodes,” IEPC–93–023, 23rd International Electric Propulsion Conference (August, 1993).
- Kameyama, I., and P.J. Wilbur, “Effects of External Flow Near High-Current Hollow Cathodes on Ion-Energy Distributions,” IEPC–97–173, 25th International Electric Propulsion Conference, (August, 1997).
- Kameyama, I., and P.J. Wilbur, “Potential-Hill Model of High-Energy Ion Production Near High-Current Hollow Cathodes,” ISTS–98–Aa2–17, 21st International Symposium on Space Technology and Science, (May, 1998).
- Keefer, D., *et al.*, “Multiplexed Laser-Induced Fluorescence and Non-Equilibrium Processes in Arcjets,” AIAA–94–2656, 25th Plasmadynamics and Lasers Conference (July, 1992).
- Keefer, D., et al., “Multiplexed LIF and Langmuir Probe Diagnostic Measurements in the TAL D-55 Thruster,” AIAA–99–2425, 35th Joint Propulsion Conference (June, 1999).
- King, L.B., “Ion energy Diagnostics in the Plume of an SPT-100 from Thrust Axis to Back Flow,” AIAA–98–3641, 34th Joint Propulsion Conference, (July, 1998).

- Kusakabe, T., et al., "Charge Transfer of Multiply Charged Slow Argon, Krypton, and Xenon Ions on Atomic and Molecular Targets. Single-Charge Transfer Cross Sections," *Journal of Physics, B*, **19** 1986, 2165–2174.
- Lindhard, J., et al., *Mat. Fys. Medd. Dan. Vid. Selsk.*, **33** (14) 1963.
- Mantenieks, M.A., "Sputtering Threshold Energies of Heavy Ions," IEPC-97-187, 25th International Electric Propulsion Conference, 1997.
- Manzella, D.H., "Stationary Plasma Thruster Ion Velocity distribution," AIAA-94-3141, 30th Joint Propulsion Conference (June, 1994).
- Marr, G.V., *Plasma Spectroscopy*, Elsevier Publishing Company, New York, 1968, pp. 272–273.
- Matsunami, N., et al., "A Semi-empirical Formula for the Energy Dependence of the Sputtering Yield," *Rad. Eff. Lett.*, **55** (15) 1980.
- Miles, R., "Lasers and Optics," Course notes, Princeton University, 1995.
- Myers, R., "Overview of Electric Propulsion Activities in Industry," AIAA-2000-3147, 36th Joint Propulsion Conference, (July, 2000).
- Patterson, M.J., et al., "Performance of the NASA 30 cm Ion Thruster," IEPC-93-108, 23rd International Electric Propulsion Conference, (September, 1993).
- Patterson, M.J., et al., "2.3 kW Ion Thruster Wear Test," AIAA-95-2516, 31st Joint Propulsion Conference (July, 1995).
- Poeschel, R.L., "2.5 kW Advanced Technology Ion thrusters," NASA CR-135076, 1976.
- Poeschel, R.L., and J.R. Beattie, "Primary Electric Propulsion Technology Study," NASA CR-159688, 1979.
- Polk, J.E., et al., "A 1000-Hour Wear Test of the NASA NSTAR Ion Thruster," AIAA-96-2717, 32nd Joint Propulsion Conference (July, 1996)
- Polk, J.E. et al., "Validation of the NSTAR Ion Propulsion System on the Deep Space One Mission: Overview and Initial Results," AIAA-99-2274, 35th Joint Propulsion Conference, (July, 1999).
- Polk, J.E., "An Overview of the Results from an 8200 Hour Wear Test of the NSTAR Ion Thruster," AIAA-99-2446, 35th Joint Propulsion Conference (June, 1999).
- Rapp, D., and W.E. Francis, "Charge Exchange Between Gaseous Ions and Atoms," *The Journal of Chemical Physics*, **37** (11) December, 1962, 2631–645.

- Rawlin, V.K., et al., "NSTAR Flight Thruster Qualification Testing," AIAA-98-3936, 34th Joint Propulsion Conference (July, 1998).
- Ruyten, W.M., and D. Keefer, "Two-Beam Multiplexed Laser-Induced Fluorescence Measurements of an Argon Arcjet Plume," *AIAA Journal*, **31** November, 1993, 2083-2089.
- Rock, B.A., "Development of an Optical Emission Model for the Determination of Sputtering Rates in Ion Thruster Propulsion Systems," Ph.D. Dissertation, Arizona State University, 1984, pp. 43-59.
- Salhi, A., *Theoretical and Experimental Studies of Orificed Hollow Cathodes*, Ph.D. Dissertation, Colorado State University, 1993.
- Sarver-Verhey, T.R., "Extended Test of a Xenon Hollow Cathode for a Space Plasma Contactor," NASA Contractor Report 195402, November, 1994.
- Schott, L., "Electrical Probes," *Plasma diagnostics*, W. Lochte-Holtgreven ed., American Institute of Physics, New York, pp. 668-725.
- Siegfried, D.E., and P.J. Wilbur, "An Investigation of Mercury Hollow Cathode Phenomena," AIAA-78-705, 13th International Electric Propulsion Conference, (April, 1978).
- Sigmund, P., "Theory of Sputtering Yields of Amorphous and Polycrystalline Targets," *Physical Review*, **184** (2) 1969, 383-416.
- Striganov, A.R., and N.S. Sventitskii, *Tables of Spectral Lines of Neutral and Ionized Atoms*, Plenum, New York, 1968, pp. 571-607.
- Stuart, R.V., and G.K. Wehner, "Sputtering at Very Low Energy Light ion Sputtering," *Journal of Applied Physics*, **33** (7) 1962, 2345-2352.
- Stuhlinger, E., "Possibilities of Electrical Space Ship Propulsion," *Ber. 5th Intern. Astronaut. Kongr.*, Innsbruck, (August, 1954) 100.
- Stuhlinger, E., *Ion Propulsion for Space Flight*, McGraw Hill, 1964, pp. 2-15.
- Sutton, G.P., *Rocket Propulsion Elements*, 6th edition, John Wiley and Sons, 1992.
- Verdeyn, J.T., Laser Electronics, 3rd ed., Prentice-Hall, 1995, p. 216.
- Wilbur, P.J., "Ion Propulsion," Advanced SEI Technologies Conference (September, 1991).

Williams, G.J., et al., Near-Field Investigation of Ions Emitted from a Hollow Cathode Assembly Operating at Low-Power,” AIAA-98-3658, 34th Joint Propulsion Conference (July, 1998).

Williams, G.J., et al., “Laser-Induced Fluorescence Characterization of Ions Emitted from Hollow Cathodes,” AIAA-99-2862, 35th Joint Propulsion Conference (June, 1999).

Williams, G.J., et al., “Laser Induced Fluorescence Measurement of the Ion Energy Distribution in the Plume of a Hall Thruster,” AIAA-99-2424, 35th Joint Propulsion Conference, (June, 1999).

Williams, G.J., et al., “Characterization of the FMT-2 Discharge Cathode Plume,” IEPC-99-104, 26th International Electric Propulsion Conference, (October, 1999).

REPORT DOCUMENTATION PAGE			Form Approved OMB No. 0704-0188	
Public reporting burden for this collection of information is estimated to average 1 hour per response, including the time for reviewing instructions, searching existing data sources, gathering and maintaining the data needed, and completing and reviewing the collection of information. Send comments regarding this burden estimate or any other aspect of this collection of information, including suggestions for reducing this burden, to Washington Headquarters Services, Directorate for Information Operations and Reports, 1215 Jefferson Davis Highway, Suite 1204, Arlington, VA 22202-4302, and to the Office of Management and Budget, Paperwork Reduction Project (0704-0188), Washington, DC 20503.				
1. AGENCY USE ONLY (Leave blank)		2. REPORT DATE April 2004		3. REPORT TYPE AND DATES COVERED Final Contractor Report
4. TITLE AND SUBTITLE The Use of Laser-Induced Fluorescence to Characterize Discharge Cathode Erosion in a 30 cm Ring-Cusp Ion Thruster			5. FUNDING NUMBERS WBS-22-982-10-02 NAG3-1572 and NAG3-2216	
6. AUTHOR(S) George J. Williams, Jr.				
7. PERFORMING ORGANIZATION NAME(S) AND ADDRESS(ES) Ohio Aerospace Institute 22800 Cedar Point Road Brook Park, Ohio 44142			8. PERFORMING ORGANIZATION REPORT NUMBER E-13100	
9. SPONSORING/MONITORING AGENCY NAME(S) AND ADDRESS(ES) National Aeronautics and Space Administration Washington, DC 20546-0001			10. SPONSORING/MONITORING AGENCY REPORT NUMBER NASA CR-2004-211296	
11. SUPPLEMENTARY NOTES This report was submitted as a dissertation in partial fulfillment of the requirements for the degree of Doctor of Philosophy in Aerospace Engineering to the University of Michigan, 2000. Project Manager, James S. Sovey, Power and On-Board Propulsion Technology Division, NASA Glenn Research Center, organization code 5430, 216-4977-7454.				
12a. DISTRIBUTION/AVAILABILITY STATEMENT Unclassified - Unlimited Subject Category: 20 Available electronically at http://gltrs.grc.nasa.gov/GLTRS This publication is available from the NASA Center for AeroSpace Information, 301-621-0390.			12b. DISTRIBUTION CODE	
13. ABSTRACT (Maximum 200 words) Relative erosion rates and impingement ion production mechanisms have been identified for the discharge cathode of a 30 cm ion engine using laser-induced fluorescence (LIF). Mo and W erosion products as well as neutral and singly ionized xenon were interrogated. The erosion increased with both discharge current and voltage and spatially resolved measurements agreed with observed erosion patterns. Ion velocity mapping identified back-flowing ions near the regions of erosion with energies potentially sufficient to generate the level of observed erosion. Ion production regions downstream of the cathode were indicated and were suggested as possible sources of the erosion causing ions.				
14. SUBJECT TERMS Electric propulsion; Ion thrusters; Laser-induced fluorescence			15. NUMBER OF PAGES 167	
			16. PRICE CODE	
17. SECURITY CLASSIFICATION OF REPORT Unclassified	18. SECURITY CLASSIFICATION OF THIS PAGE Unclassified	19. SECURITY CLASSIFICATION OF ABSTRACT Unclassified	20. LIMITATION OF ABSTRACT	

